VISIBLE LIGHT-DRIVEN PHOTOCATALYTIC FUEL CELL FOR WASTEWATER TREATMENT AND ELECTRICITY CONVERSION

WARREN TONG MENG WEI

A project report submitted in partial fulfillment of the requirements for the award of Bachelor of Engineering (Hons) Environmental Engineering.

Faculty of Engineering and Green Technology
Universiti Tunku Abdul Rahman

May 2022

DECLARATION

I hereby declare that this project report is based on my original work except for citations and quotations which have been duly acknowledged. I also declare that it has not been previously and concurrently submitted for any degree or award at UTAR or other institutions.

Signature : *Tong*

Name   : Warren Tong Meng Wei

ID No.   : 17AGB01850

Date   : 22/4/2022

APPROVAL FOR SUBMISSION

I certify that this project report entitled **"VISIBLE LIGHT-DRIVEN PHOTOCATALYTIC FUEL CELL FOR WASTEWATER TREATMENT AND ELECTRICITY CONVERSION"** was prepared by **WARREN TONG MENG WEI** has met the required standard for submission in partial fulfillment of the requirements for the award of Bachelor of Engineering (Hons) Environmental Engineering at Universiti Tunku Abdul Rahman.

Approved by,

Signature   :

Supervisor   : ChM. Ts. Dr. Lam Sze Mun

Date   : 22/4/2022

Signature   :

Supervisor   : ChM. Ts. Dr. Sin Jin Chung

Date   : 22/4/2022

ACKNOWLEDGEMENTS

First and foremost, I would like to take this opportunity to express my sincere gratitude to my diligent research supervisor, ChM. Ts. Dr. Lam Sze Mun for her invaluable guidance and advice throughout the entire research process. I would also like to express my sincere appreciation for your positive words of encouragement that motivate and inspire me to never give up during my failure times. My deepest appreciation also goes to my co-supervisor, ChM. Ts. Dr. Sin Jin Chung for his continuous support.

I would also like to say thank you to my seniors, expecially Yong Zi Jun, Choong Man Kit and Zhao Liang for teaching me the correct procedures in using the equipment and instruments. Without their willingness to assist, professional advice and suggestions, I would not be able to complete my research and thesis. Special thanks again to them for assisting me throughout the whole journey of my research with their kind support. I am also grateful for all the help given by the UTAR lab officers in ensuring all the equipment and instruments are readily available and fully functional to guarantee no delay in the research.

Lastly, I would like to express my heartfelt gratitude to my parents and fellow siblings for their invaluable support, which instilled faith into me and motivated me to complete this project.

SOLAR-DRIVEN PHOTOCATALYTIC FUEL CELL FOR WASTEWATER TREATMENT AND ELECTRIC CONVERSION

ABSTRACT

Dyestuff wastewater has high concentrations of noxious pollutants that are harmful to the environment and well-being of living organisms. However, it has huge potential to be recycled and reused for non-potable water applications such as irrigation and cleaning after proper treatment due to its ever-increasing amount being released from the industries. Photocatalytic fuel cell (PFC) is a sustainable and green technology, which is capable of treating dyestuff wastewater through photocatalytic degradation process while simultaneously producing electricity. In this study, a PFC system using $NiFe_2O_4/ZnO/Zn$ photoanode and CuO/Cu cathode was developed. The $NiFe_2O_4/ZnO/Zn$ photoanode was synthesized through the electrodeposition-hydrothermal combined method, whereas the wet chemical method was used to fabricate CuO/Cu cathode. Characterization of the prepared photoelectrodes was done through analyses such as FESEM, EDX, FTIR, XRD, UV-Vis DRS, TPR, LSV, EIS and MS. The surface morphologies, elemental compositions, functional groups and crystalline phases of the photoelectrodes were identified. Apart from that, the band gap potential, photocurrent density, interfacial charge transfer, conduction band (CB) potential and valence band (VB) potential were determined for the photoanode. Through FESEM analysis, the ZnO was revealed as having a tree-like structure with size ranging from 310 nm to 5930 nm, whereas the $NiFe_2O_4$ particles exhibited granular shapes with size varying from 64 nm to 239 nm. The CuO on the Cu cathode demonstrated rod-like structures with size fluctuating from 91 nm to 392 nm. Several process parameters were studied and they proved to have profound influence on the performance of the PFC system. Under the optimum condition of 0.5 %

NiFe$_2$O$_4$/ZnO/Zn photoanode, 0.5 M supporting electrolyte concentration and alkaline pH 10, 65 % colour removal efficiency was achieved for RhB dye solution. In the context of electricity generation, it achieved V_{oc}, J_{sc}, and P_{max} values of 637 mV, 0.1831 mA/cm^2 and 0.0253 mW/cm^2, respectively. Radical scavenging test was also conducted to determine the active radical species involved in the photodegradation process and Z-scheme photocatalytic mechanism was proposed. Subsequently, the COD mineralization study was successfully carried out and followed by recycling test. Furthermore, the effectiveness of the PFC in treating real industrial printing ink wastewater was evaluated under direct sunlight. Lastly, cost analysis was performed to analyse the real-life application of the PFC system.

TABLE OF CONTENTS

LIST OF TABLES

LIST OF FIGURES

LIST OF SYMBOLS / ABBREVIATIONS

°C	Degree Celsius
λ	Wavelength
θ	Angle Between Incident X-Ray and Reflecting Plane
2θ	Angle Between Incident X-Ray and Reflected Beam
Ω	Ohm
A	Ampere
A	Light Absorbance at Certain Wavelength
Abs	Absorbance
eV	Electron Volt
ε	Molar Absorption Coefficient
I	Circuit Current, A
J_{sc}	Short Circuit Current Density, mA/cm^2
kWh	Kilowatt-Hour
l	Length of Light Transport Path
M	Molarity
nm	Nanometer
P_{max}	Maximum Power Density, mW/cm^2
RM	Malaysian Ringgit
rpm	Revolutions Per Minute
V	Voltage
V_{oc}	Open Circuit Voltage, mV
W	Watt
C_0	Initial Dye Concentration Value
C_f	Final Dye Concentration Value

DO_0	Initial Dissolved Oxygen Value
DO_5	Final Dissolved Oxygen Value After 5 Days Incubation
E_g	Energy Band Gap
E_{CB}	Conduction Band (CB) Potential
E_{VB}	Valence Band (CB) Potential
h_v	Light Energy
R^2	Coefficient of Linear Correlation

Cl^-	Chlorite Ion
ClO^-	Hypochlorite Ion
H^+	Hydrogen Ion
$HO_2\bullet$	Hydroperoxyl Radical (or Hydrogen Superoxide)
Na^+	Sodium Ion
NH_4^+	Ammonium Ion
NO_3^-	Nitrate
NO_2^-	Nitrite
OH^-	Hydroxide Ion
$\bullet OH$	Hydroxyl Radical
$\bullet O_2^-$	Superoxide Anion
SO_4^2	Sulfate Ion
$\bullet SO_4^-$	Sulfate Radical
e^-	Electrons
$e^-\text{-}h^+$	Electron-Hole Pair
h^+	Positive Holes

1,4-BQ	1,4-Benzoquinone
Ag	Silver
AgCl	Silver Chloride
$AgNO_3$	Silver Nitrate
$BaTiO_3$	Barium Titanate
BiOI	Bismuth Oxyiodide
Bi_2WO_6	Bismuth Tungstate
$BiVO_4$	Bismuth Vanadate

C_2H_5OH	Ethanol
C_3H_8O	Isopropyl Alcohol
CO_2	Carbon Dioxide
Cu	Copper
CuO	Copper Oxide
$Fe(NO_3)_3 \cdot 9H_2O$	Iron (III) Nitrate Nonahydrate
$g\text{-}C_3N_4$	Graphite Carbon Nitride
H_2O	Water Molecule
H_2O_2	Hydrogen Peroxide
H_2SO_4	Sulfuric Acid
HCl	Hydrochloric Acid
KOH	Potassium Hydroxide
$MgSO_4$	Magnesium Sulfate
MoS_2	Molybdenum Disulfide
NaCl	Sodium Chloride
NaOH	Sodium Hydroxide
Na_2S	Sodium Sulfide
Na_2SO_4	Sodium Sulfate
$Na_2S_2O_8$	Sodium Persulfate
$NiFe_2O_4$	Nickel Ferrite
$Ni(NiO_3)_2 \cdot 6H_2O$	Nickel (II) Nitrate Hexahydrate
Pt	Platinum
Sn_3O_4	Tin Oxide
$SrTiO_3$	Strontium Titanate
TiO_2	Titanium Dioxide
WO_3	Tungsten Trioxide
Zn	Zinc
$Zn(CH_3COO)_2 \cdot 2H_2O$	Zinc Acetate Dihydrate
$Zn(NO_3)_2 \cdot 4H_2O$	Zinc Nitrate Tetrahydrate
ZnO	Zinc Oxide
FEGT	Faculty of Engineering and Green Technology
FESEM	Field Emission Scanning Electron Microscopy

FTIR	Fourier Transform Infrared
FTO	Fluorine-Doped Tin Oxide
LSV	Linear Sweep Voltammetry
MBBR	Moving Bed Biofilm Reactor
MS	Mott-Schottky
NF	Nanofiltration
NHE	Normal Hydrogen Electrode
NTU	Nephelometric Turbidity Units
PFC	Photocatalytic Fuel Cell
pH_{zpc}	Point of Zero Charge
RBC	Rotating Biological Contactor
RhB	Rhodamine B
RO	Reverse Osmosis
TDS	Total Dissolved Solids
TN	Total Nitrogen
TOC	Total Organic Carbon
TPR	Transient Photocurrent Response
TSS	Total Suspended Solids
UTAR	Universiti Tunku Abdul Rahman
UV	Ultraviolet
UV-Vis DRS	UV-Vis Diffuse Reflectance Spectroscopy
VB	Valence Band
VOC	Volatile Organic Compounds
XRD	X-Ray Diffraction

LIST OF APPENDICES

CHAPTER 1

INTRODUCTION

1.1   Advanced Oxidation Process for Treatment of Dyestuff

Over recent decades, countries across the globe are facing the issue of pollution in water bodies, which has significantly dwindled both the quantity and quality of freshwater resources. Rapid population growth, improved living standards and agricultural land expansion in addition to uncontrolled urbanization and industrialization are the main driving elements behind this situation (Saimy and Yusof, 2013; Boretti and Rosa, 2019). According to United Nations World Water Assessment Programme (2018), by 2050, it is projected that about 57% of the global population will experience the problem of clean water scarcity, causing them to have limited access of clean water supply. Despite Malaysia receiving abundant rainfall all year round, several states such as Selangor, Johor and Pulau Pinang still constantly face water shortage issue, mainly due to development, population explosion and surface water pollution (Saimy and Raji, 2015). Thus, the practice of recycling wastewater as an alternative water source is increasingly gaining popularity worldwide to meet current and future global water demand (Tortajada, 2020).

Wastewater containing pigments and dyes is suitable to be reclaimed as alternative water source since enormous quantities of such wastewater is being generated each year (Gao, Yang and Wang, 2018; Yin et al., 2019). This type of

wastewater is commonly found in industries which involve dye manufacturing and dye applying process such as printing, textile, paint and so forth (Sun and Yang, 2020). Kerkez et al. (2020) estimated that the global production of dyes (i.e. natural and synthetic dyes) is between 7×10^5 to 1×10^6 tons per annum and from this amount, a large portion of dyes is being wasted and discharged into the environment during both production and application processes. Since dye-manufacturing and dye-using industries use large amounts of clean water, which leads to huge quantities of dye-containing wastewater, it is hence important to threat and reuse these wastewater effluents as a possible water source within the industrial processes or other purposes such as irrigation and cleaning for sustainable water consumption (Yaseen and Scholz, 2018).

The dye-containing wastewater discarded by industries may cause serious environmental pollution and harm living organisms especially aquatic life if not properly treated before discharge. A variety of physical, biological, and chemical treatments have been developed and implemented over the years in order to preserve the environment (Piaskowski, Świderska-Dąbrowska and Zarzycki, 2018). However, since traditional treatment methods differ substantially in efficiency among wastewater of various origins, advanced oxidation processes (AOPs) are preferred to improve wastewater treatment. AOPs are promising technique since it is able to remove non-biodegradable (i.e. recalcitrant) organic compounds and reduce the amount of sludge produced (Hutagalung, Muchlis and Khotimah, 2020). AOPs work by utilizing strong oxidizing agents such as hydroxyl radical ($\bullet$OH) to treat the wastewater (Hassaan and Nemr, 2017). These highly reactive oxidizing agents can be formed by subjecting reagent such as hydrogen peroxide (H_2O_2) or semiconductor such as zinc oxide (ZnO) to ultraviolet (UV) radiation.

From there, both the homogenous and heterogeneous AOPs are further divided into photochemical (such as UV photolysis and photo-Fenton process) and non-photochemical (such as Fenton process, ozonation and cavitation), respectively (Verma, Kundu and Pandey, 2021). Photocatalytic fuel cell (PFC), which is nature-friendly and operates using AOPs principles has large potential in further enhancing treatment of dye-containing wastewater. PFC requires the usage of a fabricated metal-oxide semiconductor as its photoanode, which acts as a catalyst when exposed to UV

radiation from sun or artificial light, a cathode to generate electricity through the electrons received from photoanode and a liquid electrolyte (Lee et al., 2016b). The primary benefit of using PFC is that it can easily degrade organic compounds such as phenolic compounds and yield electricity concurrently, besides releasing zero toxicity emission during the process (Wu et al., 2015). Since Malaysia receives abundant amount of sunlight throughout the year, PFC has a high capability to be commercialized in treating dye-containing wastewater from industries.

1.2   Problem Statements

Active recycling and reusing of wastewater from dye-manufacturing and dye-using factories can remarkably reduce the consumption of water for domestic and industrial purposes, helping to fully optimize the usage of the exploited water resources. As a means to achieve this purpose, it is of utmost importance to employ the right treatment technique to ensure the wastewater discharged is free of any unwanted substances that will jeopardize human health and the environment.

Presently, although natural dyes are non-toxic, synthetic dyes are preferable because they offer a wide variety of colour, low production cost and long-lasting coloured effects on the applied substrate (Omotosho and Ameuru, 2019). As a result, wastewater released from dye-manufacturing and dye-using factories is usually known to have high content of salt, high amount of total dissolved solids (TDS) and total suspended solids (TSS), high turbidity, unstable pH values, high concentration levels of biological oxygen demand (BOD) and chemical oxygen demand (COD) as well as high temperature (Yaseen and Schloz, 2016). Furthermore, it is high in recalcitrant organic and inorganic compounds, besides containing many toxic substances such as phenols, heavy metals, benzenes, amines and so forth. The molecular structure of dyes contains chromophore, therefore enabling it to exhibit ability to colourise a substrate by acting as a xenobiotic compound (Shamey and Zhao, 2014). Since dyes are highly soluble, they can easily dissolve in water bodies and increase the turbidity of water, blocking sunlight penetration and subsequently lower the rate of photosynthesis (Imran et al., 2015; Hassan and Carr, 2018). This will lower the amount of dissolved

oxygen present in the aquatic ecosystem and threaten the survival of the aquatic species.

Heterogeneous photocatalysis technology is increasingly gaining attention as it offers efficient and cost-effective treatment method for degrading the organic and pollutants present inside industrial wastewater. Thence, PFC, which is a novel heterogenous photocatalysis technology has started to be employed to treat wastewater due to its capability to produce electricity while breaking down the chemical pollutants present inside the wastewater. The fundamental parts of a PFC system are photoanode, cathode and a liquid electrolyte. When exposed to light, the photoanode will undergo photoexcitation, causing photogeneration of electrons (e^-) and holes (h^+). The subsequent flow of e^- from the photoanode to the cathode along an external circuit thus initiates electricity generation. In addition, the photogenerated e^- and h^+ will generate radicals, which are responsible to degrade the organic pollutants exist inside the wastewater (Lam et al., 2013).

For the past decade, zinc oxide (ZnO) is extensively used as the semiconductor photocatalyst of PFC because of its harmless nature and it offers a wide energy band gap (E_g= 3.37 eV) (Ravichandran et al., 2014). However, some complications might arise during usage of semiconductor ZnO in PFC, hindering its ability to function as an efficient photocatalyst. Some cons of using semiconductor ZnO include it is prone to photocorrosion caused by UV irradiation and has frequent recombination occurrence between the photogenerated electrons in the conduction band and holes in the valence band (Han et al., 2014; Wu et al., 2015). Several studies have been carried out in an attempt to overcome the above-mentioned defects and the results obtained indicates that semiconductor ZnO that is doped with transition metals or oxides of transition metals has a vastly increased photocatalytic efficiency (Adeleke et al., 2018). $NiFe_2O_4$, which is a transition metal oxide has been adopted as the doping material of ZnO as it provides many advantages such that it can increase both the photocorrosion resistance and photostability of ZnO. Moreover, $NiFe_2O_4$ exhibits high degree of catalytic efficiency, can be recovered and recycled, inexpensive and non-poisonous (Iraqui, Kashyap and Rashid, 2020). Hence, coupling of ZnO together with $NiFe_2O_4$ to form the composite photoanode has a likely chance to work well in sunlight,

producing more electrons and improving the photodegradation effectiveness and performance of a PFC system.

Not much studies have been conducted on the treatment of dye-containing wastewater using a PFC system, in which the photoanode is made up of ZnO coupled with $NiFe_2O_4$, since this is a relatively new concept. In this study, the effectiveness of $NiFe_2O_4/ZnO/Zn$ composite photoanode and CuO/Cu cathode in treating dye-containing wastewater and simultaneous electricity generation will be evaluated.

1.3   Objectives

The main objectives of this study are:

1) To develop a PFC system which uses $NiFe_2O_4/ZnO/Zn$ as the photoanode and CuO/Cu as the cathode.
2) To evaluate the photocatalytic degradation efficiency of the developed PFC system using different parameters such as concentrations of electrolyte and pH of solution under visible light.
3) To study the photocatalytic mechanism using the developed PFC system.

1.4   Scope of Study

This study will develop a PFC system by synthesizing $NiFe_2O_4/ZnO/Zn$ as the photoanode and CuO/Cu as the cathode. Characterization of the photoelectrodes will be conducted through various analyses such as field emission scanning electron microscopy with energy dispersive X-ray spectroscopy (FESEM-EDX), Fourier transform infrared spectroscopy (FTIR) and so forth. The dye used in this experiment will also be characterized before undergoing treatment to determine parameters, such as BOD, COD, pH and so on. The photocatalytic mechanism of the PFC system will then be studied and its efficiency in degrading the dye will be evaluated by varying the process parameters. For example, concentrations of electrolyte and pH of solution. The

treatment performance of the developed PFC system on real wastewater collected from printing ink factory will also be studied.

CHAPTER 2

LITERATURE REVIEW

2.1 Printing Ink Wastewater

Humanity has become dependent on printing inks due to their extensive usage, ranging across a variety of products such as paper, textiles and labelling of daily items such as food, drinks, drugs et cetera (Ding et al., 2011). Printing inks used in industrial settings are roughly categorized into two main groups, namely solvent-based inks (consists of mainly organic solvent) and water-based inks (consists of mainly water) (Ramirez and Tumolva, 2018). Since the early 2000s, the world has observed a shifting trend from solvent-based inks rather to water-based inks. This is because the latter contains a lower percentage of volatile organic compounds (VOC), making it safer to the environment and living organisms (Ma and Xia, 2009). However, this may have indirectly resulted in a higher generation amount of printing ink wastewater because manufacturing and utilization of water-based inks require the use of higher amount of clean water.

In reality, it is still unfeasible for industries to fully transition from solvent-based inks to water-based inks. The key reason is water-based inks display ineffective adhesion effect when applied on non-perforated surfaces such as plastic and metal. Any printing ink is a complex mixture regardless of its type. Printing inks generally consists of colouring agents, solvents, resins, oils and other enhancers (Aydemir et al.,

2017). Due to the presence of these substances, printing ink wastewater has a significant amount of persistent organic and inorganic matter, as well as being dark-coloured (Ma and Xia, 2010). Therefore, it is crucial to treat printing ink wastewater every time before discharging into water bodies to prevent any accidental damage to the environment.

The water quality of printing ink wastewater can be determined via several parameters such as pH, biological oxygen demand (BOD), chemical oxygen demand (COD), total organic carbon (TOC), total suspended solids (TSS), total dissolved solids (TDS), nitrate (NO_3^-), nitrite (NO_2^-) and ammonium (NH_4^+). According to a study conducted by Pal (2017), wastewater effluent generated from printing process in a textile industry has an average pH of 8.06, BOD of 170 mg/L, COD of 1907 mg/L, TSS of 499.4 mg/L, NO_3^- of 6.06 mg/L, NO_2^- of 0.91 mg/L and NH_4^+ of 14.34 mg/L. As per another study done by Pei and Yu (2016), they reported that the average COD value for wastewater generated from printing industries is 20000 mg/L. Therefore, it is noteworthy that the quantity and quality of printing ink wastewater produced differ considerably among industries because of the different chemicals and printing technology being used.

The main synthetic dye group found in printing ink wastewater is azo dyes since more than half of the industrial dyes used are azo dyes (Hagan and Poulin, 2021). However, other man-made dye groups such as xanthene, azine and oxazine are still widely used by industries. The unique molecular arrangement of these dyes makes them highly stable and resistant to environmental, biological and chemical changes (Benkhaya, M'rabet, El Harfi, 2020). Printing ink wastewater coloured by synthetic dyes, which are highly soluble will easily change the appearance of water bodies. In addition, carcinogens, mutagens and teratogens arise from degradation of untreated synthetic dyes are toxic to living organisms.

For example, when Rhodamine B which is a type of highly carcinogenic xanthene dye widely used to produce ink is accidentally ingested, it can bring about sarcoma (Shen and Gondal, 2017). Basic Red 9 dye, which is an azo dye also used as colouring agent mainly for printing ink can be easily broken down into carcinogenic aromatic amines under anaerobic conditions and direct contact with it can cause skin

allergies and cancer if severe (Sivarajasekar and Baskar, 2014). Besides that, since the heavy metals present in unnatural dyes such as copper, nickel and cadmium are extremely persistent, they will easily remain in fish tissues and undergo biomagnification as they move through food chains, resulting in organisms situated at higher trophic levels (i.e. humans) will experience higher level of contamination than those at lower trophic levels (Lellis et al., 2019). These heavy metals can have adverse impacts on the endocrine, reproductive, neurological and respiratory systems of humans and animals (Sall et al., 2020).

2.2   Printing Ink Wastewater Treatment Methods

The use of recycled and reclaimed printing ink wastewater as an alternative water source will ensure the continuity of water security for current and future generations. Prior to this noble practice, printing ink wastewater must be treated to ensure it is safe for use. Various treatment methods including physical, biological, and chemical treatments have been applied to achieve this. Depending on variables such as wastewater origins, industrial processes, and chemicals used, each technology has its own strengths and limitations. This section will review past research projects in order to find the most efficient and economically feasible method for treating printing ink wastewater.

2.2.1   Physical Treatment Methods

Physical treatment of wastewater involves removing suspended solids and other impurities physically without introducing microorganisms or chemicals, preserving the biological and chemical characteristics of the wastewater pre- and post-treatment (Katheresan, Kansedo and Lau, 2018). Dye removal from printing ink wastewater is commonly achieved with adsorption and membrane filtration technologies.

Physical adsorption or physisorption treats wastewater by concentrating impurities such as dye particles, suspended solids and dissolved solids onto a porous absorbent which has a large contact area by applying attraction forces (Pei and Yu, 2016). For instance, hydrogen bonding, Van der Waals forces and so on. Banerjee et al. (2019) had conducted an experiment using alumina (Al_2O_3) nanoparticles as the adsorbent substance to treat dye-containing wastewater at pH level of 2.5 and 30 ℃. Based on the studies, 1 g/L of nanoparticles were able to achieve removal rate of 63.9 % for Orange G, 64.1 % for Indigo Carmine and 56.6 % for Reactive Red 180. It was also found that increased amount of adsorbent used, longer retention time and lower pH, the dye, BOD and COD removal rate increased significantly. Although this method was simple, applicable for a wide spectrum of dyes and the adsorbent used was recyclable, however it was both time-consuming and financially unviable due to the relatively high cost of the adsorbent used.

Another physical treatment method in treating wastewater is membrane filtration technologies which utilize a semi-permeable membrane. For instance, pressure-driven membrane processes, namely microfiltration, ultrafiltration, nanofiltration and reverse osmosis. Nanofiltration (NF) removes pollutants that have a size larger than 0.001 µm, thus only allowing monovalent ions and certain small-sized multivalent ions to pass through. The blocking of large-sized particles is through size exclusion and charge repulsion between solute and membrane. Kurt et al. (2012) had evaluated the effectiveness of NF in treating wastewater from the weaving industry using a NF-270 membrane. It was reported that close to 100 % of colour, 94.7 % of COD and 76.3 % of salinity were removed. Although application of NF showed satisfactory effectiveness in treating wastewater, certain constraints such as frequent fouling of membranes and high operational costs were determined.

Porous size of membrane used in reverse osmosis (RO) is smaller than that of NF. This prevents more suspended particles, ions, and other pollutants from passing through. During RO, pressure is applied to the contaminants-packed membrane side, pushing the water molecules through the porous membrane to the other side as purified water. The research done by Liu et al. (2011) had shown that RO achieved a higher removal of salinity than NF. The main disadvantages of RO compared to NF are higher operational and maintenance costs.

2.2.2 Biological Treatment Methods

In biological treatment, plants or microorganisms culture such as bacteria, algae and fungi are being used to carry out biodegradation, breaking down unwanted organic and inorganic particles into non-toxic substances, either through an aerobic or anaerobic process (Jamee and Siddique, 2019). The charged functional groups such as amino and carboxyl on the plants and microbes' cell wall help attract the contaminants to the microorganisms, enabling the plants and microbes to consume them (Ayele et al., 2021). Biological treatment technologies are widely applied globally because it is affordable and environmentally friendly. Some common examples of such treatment technologies are rotating biological contactor (RBC), moving bed biofilm reactor (MBBR) and constructed wetland (CW).

In MBBR, wastewater is flown through a bed of movable particles with large total surface area. When the wastewater comes into contact with the microorganisms thriving on the particles, the pollutants present inside the wastewater will be biodegraded (Safwat, 2018). Yang et al. (2020) had conducted a study on the performance of MBBR in treating dye-containing wastewater from a textile factory. They reported that at 25 °C, hydraulic retention time of 24 hours and usage of 3.5 g/L of biomass, 82 % of COD, 78 % of TSS and more than 90 % of total nitrogen and phosphorus were removed.

CW is an engineered treatment method used for removing pollutants present in wastewater by simulating the ecological processes of natural wetlands, i.e. the relationship between vegetation, soil media and microbes (Vymazal, 2011). Sahayarayan, Ramasamy and Kandasamy (2019) evaluated the performance of a vertical flow CW in treating dyestuff wastewater from a textile factory. They found that using a CW planted with *Alternanthera sessilis* subjected to a detention time of 24 hours, 60 % of TDS, 83 % of TSS, 81 % of BOD and 73 % of COD were successfully removed. Furthermore, they reported that replacing *Alternanthera sessilis* with *Zea mays* will have a lower removal efficiency of 58 % for TDS, 77 % for TSS as well as 63 % for both BOD and COD.

Biological treatment methods are inexpensive, easy to operate and produce

non-hazardous by-products. However, the efficiency of biological treatment methods is heavily dependent on the type of organism used. For instance, fungi such as *Chaetomium globosum*, *Trametes versicolor* and *Cylindrocephalum aurelium RY06* were reported to have high level of dye removal efficiency (Bankole, Adekunle and Govindwar, 2018; Dayi, Kyzy and Akdogan, 2019; Mostafa et al., 2019). However, they tend to experience a long lag phase (Katheresan, Kansedo and Lau, 2018; Solís et al., 2012). On the other hand, bacteria such as *Bacillus* and *Rhodococcus* have a faster growth rate, thus able to remove wastewater pollutants in a shorter time (Samsani et al., 2020). One common disadvantage of all types of biological treatment methods are the organisms used are sensitive to pH, temperature, shock-load and other environmental factors (Solís et al., 2012; Katheresan, Kansedo and Lau, 2018).

2.2.3 Chemical Treatment Methods

Chemical treatment methods involve the addition of chemicals to generate chemical reactions, thus achieving the purpose of removing pollutants from targeted wastewater (Hynes et al., 2020). Examples of commonly used chemical treatment methods are coagulation-flocculation, ion exchange and so forth.

Coagulation-flocculation involves first adding coagulants such as alum or other suitable salts or polymers followed by flocculants such as polymers. Coagulants help to neutralize the charge of pollutant particles, reducing their repulsive forces, whereas coagulants bind the fine pollutant particles together, forming large-sized agglomerate, which settles easily (Ahmad et al., 2015; Collivignarelli et al., 2019). The settled lump will then be removed through filtration. Arumathi et al. (2019) evaluated the performance of polyaniline as coagulant in treating dyestuff wastewater. From their study, they realized that using 1.6 g /L of polyaniline at pH 8, 94.38 % of colour, 91.45 % of COD and 86.1 % of turbidity were successfully removed.

The electrocoagulation method utilizes the electrochemistry principle for chemical treatment (Moussa et al., 2017). During electrocoagulation, the coagulant is locally produced through oxidation at the anode rather than using chemical coagulant

additives. The hydrogen bubbles generated at the cathode during reduction will then trap the floc and allow it to float on the surface of the water, easing its subsequent removal (Chellam and Sari, 2016). As per the research done by Papadopoulos et al. (2019), they reported that electrocoagulation method achieved removal rate of approximately 75 % for COD and 99 % for colour when treating printing ink wastewater.

Another chemical method for treating wastewater is ion exchange. In order to conduct an ion exchange process, a bed of charged solid particles is required, which facilitates ion exchanges between the solid particles and the unwanted ions in the wastewater. When the resin microbeads are saturated, it must be recharged to function properly again. A study conducted by Deaconu et al. (2016) shown that utilization of macroporous polymeric ion exchanger could remove about 64 % of TN, 90 % of turbidity and 95 % of colour from dyestuff wastewater.

Even though chemical treatment methods have a higher efficiency in degrading dyes than physical and biological treatment methods, they are noticeably more expensive (Katheresan, Kansedo and Lau, 2018). A large amount of chemicals and equipment are required when using chemical treatment methods, thus impeding their usage and commercialization process. For example, electrochemical coagulation requires high amount of electricity and chemicals to treat dye, besides producing secondary pollutant which needs additional treatment and disposal (Kumar et al., 2012). Nonetheless, state-of-the-art photocatalytic fuel cell (PFC) system which operates using advanced oxidation principles as will be discussed in the following section is able to overcome all the defects mentioned.

2.3   Advanced Oxidation Processes

At present, advanced oxidation processes (AOPs) are gaining immense recognition for their capability to further refine current wastewater treatment methods, specifically in breaking down toxic organic pollutants like dyes. In AOPs, highly reactive oxidants primarily hydroxyl radicals ($\bullet$OH) are produced through chemical reactions to treat the

wastewater (Kokkinos, Venieri and Mantzavinos, 2021). Typically, homolytic cleavage is used to form •OH from hydrogen peroxide (H_2O_2), whereby light is applied to break the O–O bond of H_2O_2 (Shabat-Hadas, Mamane and Gitis, 2017). In fact, besides •OH, other radicals which are strong oxidizers such as superoxide anions and hydroperoxyl radicals may also be generated in certain AOPs (Giannakis, Ritmi and Pulgarin, 2017). The AOPs can be categorized into two main types, namely homogenous and heterogeneous AOPs. From there, both the homogenous and heterogeneous AOPs are further divided into photochemical (such as UV photolysis and photo-Fenton process) and non-photochemical (such as Fenton process, ozonation and cavitation), respectively (Verma, Kundu and Pandey, 2021).

AOPs are recommended compared to other wastewater treatment methods because of the non-selectivity characteristic of the highly oxidative radicals (Galeano et al., 2019). As a result, most refractory organic and inorganic pollutants may easily be removed through AOPs, enabling higher quality of treated wastewater to be achieved and reused (Bilińska, Gmurek and Ledakowicz, 2017). Unlike coagulation-flocculation which is also a chemical treatment method, AOPs will not produce any sludge (Katheresan, Kansedo and Lau, 2018). This eliminates the need for sludge recovery and treatment, achieving cost reduction. Sun et al. (2019a) evaluated the performance of ozonation in degrading wastewater containing azo dyes under different ozone dosage, pH values and initial dye concentrations. From their study, they found out that Direct Red 80 dye underwent decolourisation rate of 99 % when ozone dosage of 1.25 g/(L/min) and pH level of 12 are applied for dye concentration of 100 mg/L.

2.3.1 Photocatalytic Fuel Cell

In the recent past, rapid advances in the field of AOPs have given rise to a novel wastewater treatment technology, that is photocatalytic fuel cell (PFC). PFC has an edge over traditional wastewater treatment approaches because as it treats wastewater through photocatalytic degradation of organic pollutants, electricity generation will happen as well. In addition, PFC will not produce secondary pollutants. This makes PFC an environmentally-friendly method that has a promising future. The general set-

up of a PFC system is illustrated in Figure 2.1 below. It is clear that a PFC system requires photoanode, cathode, external circuit connecting photoanode and cathode together in addition to a liquid electrolyte.
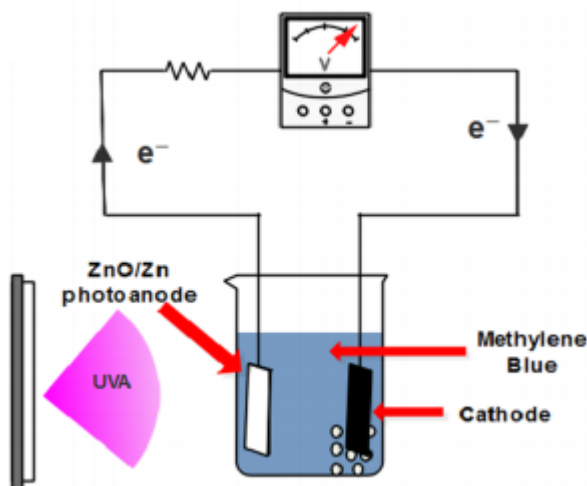
Figure 2.1: Set-Up of a PFC System to Treat Dyestuff Wastewater (i.e. Methylene Blue Solution) Under Light Exposure (Lee et al., 2016a).

Upon coming into contact with light irradiation, the photoanode bearing a semiconductor photocatalyst will experience photoexcitation by absorbing photons encountered. As a result of this, generation of electron-hole (e_{CB}^--h_{VB}^+) pair happens, as shown in Equation (2.1) (Sfaelou and Lianos, 2016). It is pivotal that the incoming light irradiation has energy equals to or greater than the energy band gap of the photocatalyst used in order to enable excitation of e^- from valence band (VB) to conduction band (CB) (Vasseghian et al., 2020). At the same time, the uncoupled h^+ remains in VB.

$$Photocatalyst + h_v \rightarrow e_{CB}^- + h_{VB}^+ \tag{2.1}$$
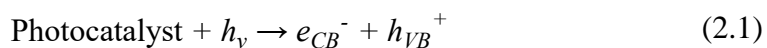
The e_{CB}^- produced will then move via an external circuit from photoanode to cathode, thus generating electricity. On the other hand, h^+ at the photoanode will react with hydroxide ions (OH⁻) or water molecules to produce hydroxyl radicals (•OH) as pointed out by Equations (2.2) and (2.3) below (Kee et al., 2018; Vasseghian et al., 2020).

$$h_{VB}{}^+ + OH^- \rightarrow \bullet OH \qquad (2.2)$$

$$h_{VB}{}^+ + H_2O \rightarrow \bullet OH + H^+ \qquad (2.3)$$

Once the $e_{CB}{}^-$ reaches the oxygenated cathode, they will react with the available oxygen molecules, producing radicals such as superoxide anions ($\bullet O_2^-$) and hydrogen superoxide (or hydroperoxyl radicals) ($HO_2\bullet$) (Vasseghian et al., 2020). In addition, hydrogen peroxide (H_2O_2) may also be produced (Kee et al., 2018). H_2O_2 is not a radical, however it can easily be converted into $\bullet OH$. The following Equations (2.4) – (2.7) illustrate clearly the processes (Zhao et al., 2017).

$$e_{CB}{}^- + O_2 \rightarrow \bullet O_2^- \qquad (2.4)$$

$$\bullet O_2^- + H^+ \rightarrow HO_2\bullet \qquad (2.5)$$

$$O_2 + 2H^+ + 2e_{CB}{}^- \rightarrow H_2O_2 \qquad (2.6)$$

$$H_2O_2 + e_{CB}{}^- \rightarrow \bullet OH + OH^- \qquad (2.7)$$

In simple terms, the $h_{VB}{}^+$ degrades organic pollutants through oxidation, whereas $e_{CB}{}^-$ achieves the same purpose via reduction (Kee et al., 2018). Furthermore, the radicals produced by $h_{VB}{}^+$ and $e_{CB}{}^-$ such as $\bullet OH$ and $\bullet O_2^-$ are known to have high oxidation strength and non-selective, thus allowing higher degree of mineralization rate of the organic pollutants to be attained. The reactions for the degradation processes by $\bullet OH$ and $\bullet O_2^-$ are represented by Equations (2.8) and (2.9) (Samsudin et al., 2015). Figure 2.2 shows the schematic diagram of photocatalytic mechanism of a PFC system.

$$\text{Organic pollutants} + \bullet O_2^- \rightarrow CO_2 + H_2O + \text{by-products} \qquad (2.8)$$

$$\text{Organic pollutants} + \bullet OH \rightarrow CO_2 + H_2O + \text{by-products} \qquad (2.9)$$
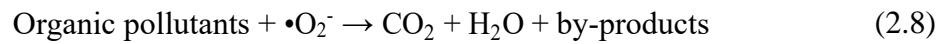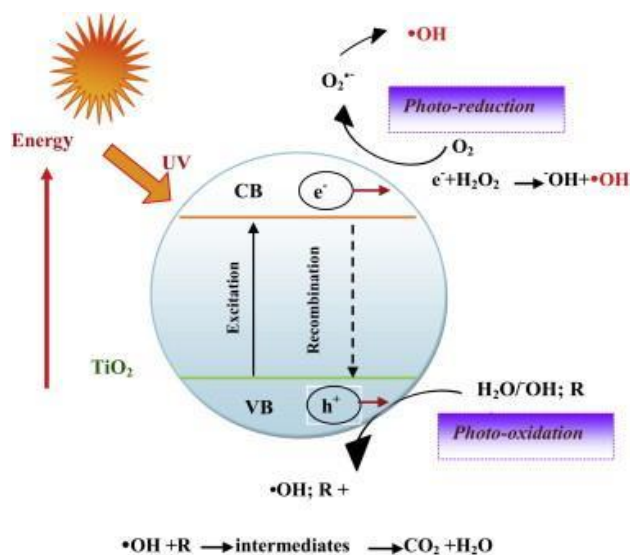
Figure 2.2: Photocatalytic Mechanism of a PFC System for Wastewater Treatment (Jaafar et al., 2013).

Other than photoanode and cathode, the selection of a suitable supporting electrolyte is necessary for a PFC to achieve a high dye degradation efficiency during wastewater treatment (Ong et al., 2020). This supporting electrolyte helps to lower the internal resistance of the PFC system (Wang et al., 2014). This promotes movement of ions and charge transfer, enabling more radicals to be produced to treat the wastewater (Liao et al., 2015). Besides that, higher energy output can be achieved due to the ease for e_{CB}^{-} to move from photoanode to cathode. Studies conducted over the years shown that using sodium sulfate (Na_2SO_4) as the electrolyte in PFC led to a higher wastewater treatment efficiency compared to other electrolytes (Sun et al., 2019b). Na_2SO_4 is universally acknowledged because it is chemically inert and highly stable.

The efficiency of the PFC system might vary depending on the light source and types of targeted dye. Lee at al. (2018) evaluated the effectiveness of a PFC system in degrading several azo dyes under sunlight and UV irradiation. The PFC system was constructed using a ZnO/Zn photoanode and a Pt/C cathode. They found that after exposing the PFC system to sunlight and UV irradiation (wavelength 350 - 400 nm) for 8 hours, colour removal rate of 93 % and 86 % were achieved for Reactive Green 19. However, after repeating the same experiment for Acid Orange 7, they observed that colour removal rate of 63 % and 76 % were achieved under sunlight and UV

irradiation. They justified that Reactive Green 19 achieved a higher degradation rate because it is more nucleophilic than Acid Orange 7, thus its azo bonds have more electrons, making it more likely to be oxidized. Another reason that they mentioned was that Reactive Green 19 has more anion groups than Acid Orange 7, making it easier to be oxidized due to attraction of anions to the positively-charged photoanode.

2.3.1.1 Modification of Photoelectrodes in Photocatalytic Fuel Cell

An ideal PFC system relies on an internal potential difference between its photoanode and cathode electrodes. Potential differences contribute to pollutant degradation and electricity generation. However, the PFC system consistently faces one constraint, namely frequent e_{CB}^--h_{VB}^+ pairs recombination. The degradation performance of the PFC system will be adversely affected as there will be fewer ions available to react to produce radicals that are highly oxidative, subsequently leading to reduced energy output.

With the intention of improving the photocatalytic performance of the PFC system, numerous studies have been done on the photoanode over the years. It was reported that modification by doping the semiconductor photoanode with another semiconductor (primarily transition metal or transition metal oxides) having different energy band gap to form heterojunction photoanode is able to inhibit the recombination of e_{CB}^- and h_{VB}^+ (Adeleke et al., 2020; Solomon et al., 2020). This is due to the presence of lowered energy band gap in heterojunction photoanode (Solomon et al., 2020), allowing more e^- to be photoexcited from VB to CB. Moreover, narrowed energy band gap promotes the generation of more e_{CB}^- and h_{VB}^+, enhancing the photocatalytic degradation and electricity yield of the PFC system. Figure 2.3 shows the energy band gap of certain semiconductors under specific conditions.
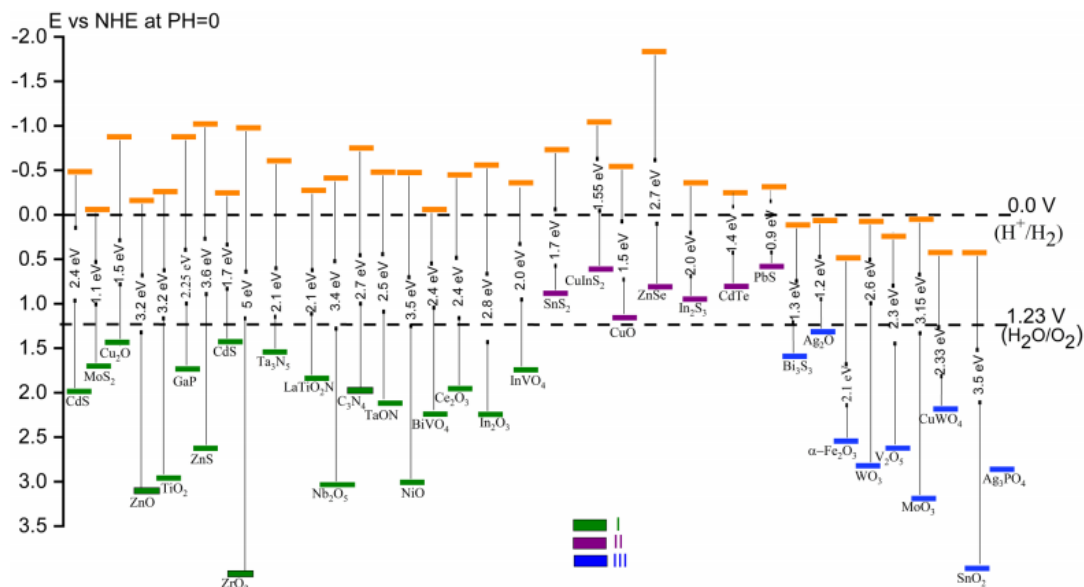
Figure 2.3: The Energy Band Gap of Certain Semiconductors at pH Level of 0 and in Reference to Normal Hydrogen Electrode (NHE) (Hisatomi, Kubota and Domen, 2014; Lu et al., 2016; Kumar et al., 2017).

Kappadan, Thomas and Kalarikkal (2020) modified the photoanode by coupling barium titanate ($BaTiO_3$) onto ZnO to form a heterojunction photoanode through hydrothermal method. They found that $BaTiO_3$ alone accomplished a degradation rate of 72 % for methylene blue dye and 23 % for phenols when subjected to UV irradiation from a 250 W lamp for an hour. In contrast, after repeating the same experiment using $BaTiO_3$/ZnO heterostructure, higher degradation efficiency was attained, i.e. about 94 % for methylene blue dye and 48 % for phenols. The reason given by them was that using $BaTiO_3$/ZnO reduced the internal charge transfer resistance of the PFC, easing the separation process of e_{CB}^--h_{VB}^+ pair. The recombination rate of e_{CB}^- and h_{VB}^+ was minimized, enabling more e_{CB}^- and h_{VB}^+ to carry out photocatalytic degradation.

In a separate study performed by Ungan and Tekin (2019), the effect of coating duration on the photocatalytic degradation efficiency of PFC system was analysed. Sol-gel method was conducted in the presence of ultrasonic irradiation in order to prepare two types of heterojunction photoanode, namely TiO_2/Ag and TiO_2/ZnO. Fabrication process for each of the photoanode was done three times under different coating durations, i.e. 30 minutes (coated with four layers), 45 minutes (coated with

four cycles) and 60 minutes (coated with 10 cycles). They reported that for both photoanodes, coating duration of 30 minutes gave the most optimum photocatalytic degradation efficiency in treating Acid Red 27 dye under the presence of 44 W UV lamp with a wavelength of 254 nm. They explained that long coating time have thickened the TiO_2 photocatalyst and caused blocking in its pores. The thick layers may have inhibited the movement of e_{CB}^- through the photoanode, hence causing higher recombination rate between e_{CB}^- and h_{VB}^+.

2.3.1.2 Methods of Synthesizing Photoelectrodes in PFC System

Photoelectrodes play a major role in PFC system since they aid in degrading organic pollutants and generate electricity. On account of this, it is vital to synthesize photoelectrodes that are of the highest quality. The rapid progress of nanostructures has led to them being integrated into the PFC system to further improve the performance of PFC system by increasing the total surface area available for reaction to occur and charge transfer conductivity of the photoanode (Shen et al., 2018). Several fabrication methods are available to synthesize nanostructure-based photoanodes. For example, hydrothermal method, template synthesis method, anodization method, sol-gel method and dip-coating method (Ren and Gan, 2012; Rane et al., 2018). Nanostructure-based photoanodes come in a variety of shapes and sizes such as nanoneedles, nanorods, nanotubes and nanosheets, depending on requirements and process parameters such as reaction time, temperature and pH value (Shen et al., 2018).

Bai et al. (2016) analyzed the performance of a PFC system constructed using dual nanostructure-based heterojunction photoelectrodes, namely $BiVO_4/TiO_2$ nanotubes photoanode and ZnO/CuO nanowires cathode. First, hydrothermal method subsequently liquid phase deposition for 20 minutes at 25 °C were done to form TiO_2 nanotubes. After that, spin coating was conducted to apply layers of $BiVO_4$ onto the surface of TiO_2 nanotubes, forming the $BiVO_4/TiO_2$ photoanode. While for cathode synthesis, wet chemical method was first conducted to produce $Cu(OH)_2$ nanosheets. Then, spin coating was done to form $Cu(OH)_2$ nanosheets coated with zinc acetate,

which eventually yields the ZnO/CuO photoanode after heated at 400 °C for an hour. They reported that after operating under sunlight for 80 hours, the PFC system successfully achieved dye degradation rates of 76 % for methyl orange, 83 % for methylene blue and 90 % for Congo red. They attributed this high performance to the usage of TiO_2 nanotubes and CuO nanowires which provided a larger surface area, promoting the formation of radicals. They added that $BiVO_4$ has a small energy band gap, i.e. 2.4 eV, thus easing the separation process of h_{VB}^+ and e_{CB}^-. Besides that, due to its high photocorrosion resistance, $BiVO_4$ helped improve the photoanode stability.

Xie and Ouyang (2017) investigated the performance of a PFC system constructed using a WO_3 nanoflakes/FTO photoanode and an air-breathing Pt/C cathode. The synthesis of the photoanode started with carrying out of hydrothermal process by immersing cleaned FTO substrates inside an evenly mixed mixture consisting of sodium tungsten dihydrate, deionised water, hydrochloric acid and ammonium oxalate at 120 °C for 12 hours. Then, the WO_3/FTO photoanode was required to undergo annealing at 450 °C for an hour. They reported that under irradiation of artificial light having a light density of 200 mW/cm^2 for a duration of 8 hours, the PFC system achieved a removal rate of 90.4 % for oxytetracycline hydrochloride. They mentioned that the capability to absorb visible light was profusely higher in WO_3/FTO photoanode than FTO alone, hence enabling generation of large amount of h_{VB}^+ and e_{CB}^-. Although oxytetracycline hydrochloride is an antibiotic and not a dye, this work done by the authors provided an insight into how a PFC system can be modified accordingly to give better performance on degradation of dyes and electricity generation.

He et al. (2018a) studied the performance of a PFC system constructed using nanostructure-based heterojunction photoelectrode. TiO_2 covered with quantum-dot CdS/ZnS nanoparticles were used by them. First, sol-gel method was conducted by stirring a mixture of TiO_2, deionized water, acetylacetone and polyethylene glycol using a magnetic stirrer for 12 hours. After that, spray-coating was done to deposit a thin layer of the prepared TiO_2 mixture on a carbon paper. After calcining the coated carbon paper at 550 °C for 2 hours, it was allowed to soak in two solutions, namely mixture of $Cd(NO_3)_2$ and $Zn(NO_3)_2$ for four minutes followed by Na_2S for five minutes after rinsing with deionized waster. Lastly, the TiO_2/CdS/ZnS photoanode was rinsed
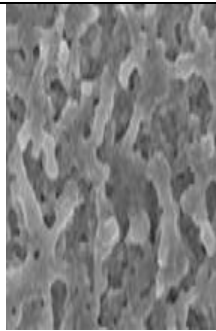
with deionized water again and dried at 100 ℃ for 10 minutes. They reported that the efficiency of the PFC system improved significantly compared to the previous similar work done by Seger and Kamat (2009) which did not use nanostructure-based heterojunction photoanode when treating organic pollutants. He et al. (2018a) stated that the addition of quantum-dot CdS/ZnS nanoparticles increased the visible light absorption capability of the PFC system, enabling higher efficiency in removing organic pollutants and yielding energy.
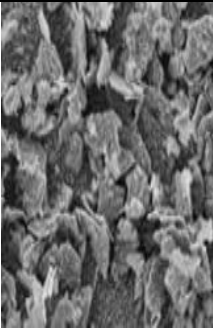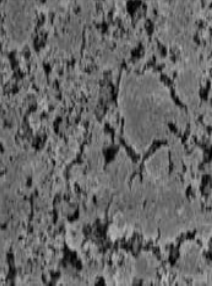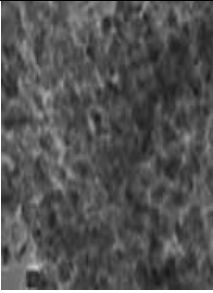
In another separate study, Li et al. (2020) tested the photocatalytic performance of differently-sized nanomaterials. The TiO_2 photocatalyst nanoparticles were prepared through alkaline hydrothermal treatment method. First, they stirred anatase TiO_2 together with distilled water and sodium hydroxide in the proportion of 0.6 g: 60 mL: 12 g for 30 minutes before subjected to temperature of 180 ℃ inside an autoclave for 24 hours. Finally, the modified TiO_2 was neutralized using distilled water and placed under annealing inside a furnace of 400 ℃ for 3 hours, 12 hours, 24 hours and 48 hours containing nitrogen atmosphere before being utilized in PFC system. They reported that TiO_2 that underwent annealing for 24 hours displayed the best degradation rate, i.e. 72.7 % for Rhodamine B dye after two hours of treatment under visible light. Pure TiO_2 only achieved degradation rate of 6.2 % within the same period of time. This phenomenon was due to the presence of surface defects and nanocrystalline structure of the modified TiO_2. They added that the increase in surface reaction area led to generation of significantly higher amount of $\bullet O_2^-$ radicals by the modified TiO_2, enhancing the degradation process of Rhodamine B. This proven that synthesizing nanostructure-based photocatalyst is able to improve the performance of PFC system.
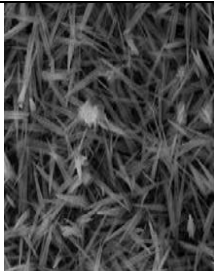
During their study, Li et al. (2020) also noticed an interesting scenario, which was TiO_2 that underwent annealing for 48 hours attained a degradation rate of 28.3 %. Supposedly, longer annealing duration should lead to higher degree of dye degradation rate by the PFC system. The explanation they offered for this contradictory behaviour was that longer hydrothermal times disrupted the structure of TiO_2. The authors suggested that alkali metal oxides might accumulate on the surface of TiO_2. As a result, the surface area available for reaction was reduced, even though they have the smallest crystalline structure, eventually affecting their phototcatalytic degradation efficiency.

Through reviewing all reported past works, it is evident that the performance of a PFC system is remarkably affected by the morphological features of the photoelectrodes used. Thus, suitable fabrication methods if done properly may be able to change the structure of photoelectrodes and assist the PFC system in achieving increased pollutants degradation efficiency and electricity generation rate by enhancing its total surface area available for reaction, volume of pores, amount of h_{VB}^{+} and e_{CB}^{-} generated and so forth. A summary of the conventional fabrication methods of the photoelectrodes is shown in Table 2.1 below.

Table 2.1: Summary of Conventional Fabrication Methods for the Photoelectrodes.

Photoanodes									
Type of Photoelectrodes	Nanostructures	Synthesis Methods	Precursors	Synthesis Conditions	Particles Size (nm)	Heterojunction Morphologies	Substrates degradation efficiency	Maximum power density (P_{max}, W/m^2)	References
BiVO$_4$/TiO$_2$ (photoanode) ZnO/CuO (cathode)	TiO$_2$ nanotubes	Hydrothermal method, liquid-phase deposition, spin coating method, annealing	(NH$_4$)$_2$(TiF)$_6$, H$_3$BO$_3$, Bi(NO$_3$)$_3$, NH$_4$VO$_3$, HNO$_3$, 0.1 M Na$_2$SO$_4$ solution	Liquid phase deposition: 25 ℃, 20 min; annealing: 450 ℃, 2 h, in air	~ 400		Removal rates of 76 %, 83 % and 90 % for methyl orange, methylene blue and Congo red.	1.16	Bai et al (2016)

WO$_3$/FTO (photoanode) Pt/C (cathode)	WO$_3$ nanoflakes	Hydrothermal method, annealing	HCL, ammonium oxalate, acetone, isopropanol, 0.1 M Na$_2$SO$_4$ solution	Reaction: 120 °C, 12 h; drying: 60 °C, in air; annealing: 450 °C, 1 h	~ 200		Removal rate of 90.4 % for oxytetracycline hydrochloride.	0.36	Xie and Ouyang (2017)
TiO$_2$/CdS/ZnS (photoanode) Pt/C (cathode)	Quantum-dot CdS/ZnS nanoparticles	Sol-gel method, spray coating, successive ionic adsorption and reaction (SILAR)	Polyethylene glycol, Cd(NO$_3$)$_2$, Zn(NO$_3$)$_2$, Na$_2$S, 0.2 M KOH solution	SILAR process: 4 to 5 min; drying: in N$_2$ stream; heating: 100 °C, 10 min	~ 50		Achieved 75 % higher organic pollutants removal rate than the work previously reported.	1.01	He et al. (2018a) Seger and Kamat (2009)
TiO$_2$ (no mentioning of photoanode and cathode)	TiO$_2$ nanoparticles	Alkali-hydrothermal method	Anatase TiO$_2$, NaOH	Reaction: 180 °C, varying heating duration; freeze-dried; calcination: 400 °C, 2 h	~ 20 - 100		Degradation rate of 72.7 % for Rhodamine B dye.	N/A	Li et al. (2020)

Cathodes									
Type of Photoelectrodes	Nanostructures	Synthesis Methods	Precursors	Synthesis Conditions	Particles Size (nm)	Heterojunction Morphologies	Substrates degradation efficiency	Maximum power density (P_{max}, W/m^2)	References
$BiVO_4/TiO_2$ (photoanode) ZnO/CuO (cathode)	CuO nanowires	Electro-deposition, wet chemical method, spin casting, annealing, hydrothermal method	$CuSO_4$, lactic acid, NaOH, $(NH_4)_2S_2O_8$, zinc acetate solution 0.1 M Na_2SO_4 solution	Electro-deposition: pH 11; annealing: 400 ℃, 1 h	~ 400		Removal rates of 76 %, 83 % and 90 % for methyl orange, methylene blue and Congo red.	1.16	Bai et al (2016)

2.4 Process Parameter Study

In order to ensure high photocatalytic degradation efficiency, various parameters must be taken into account when constructing the PFC system. These include the initial concentration of the pollutants, types of electrolyte used and its concentration along with the pH of the initial solution (Antoniadou and Lianos, 2014). Owing to the fact that these parameters have such a significant impact on the performance of PLC systems, they will be investigated and discussed thoroughly in the present study.

2.4.1 Types of Electrolyte and its Concentration

The electricity generation and photocatalytic degradation efficiencies of the PFC system appeared to be affected by the electrolyte selected and its concentration used. Electrolytes play an essential role in PFC operation because they help to improve the conductivity of the electrons (e_{CB}^-) and holes (h_{VB}^+) by decreasing the inner resistance confronted by them (Shen et al., 2006). Furthermore, electrolytes aid in the diffusion of the H^+ ions produced at the photoanode to the cathode. The higher conductivity therefore facilitates the production of more highly oxidative species, thereby increasing the removal efficiency of organic pollutants from wastewater (Zhu et al., 2009). In addition, the ease of transfer from photoanode to cathode for e_{CB}^- promotes higher electrical energy output (Fu et al., 2018).

Lee et al. (2016) investigated the performance of a PFC system using different types of electrolytes, which are NaCl, Na_2SO_4 and $MgSO_4$. They reported that the PFC built using a ZnO/Zn photoanode and a Pt/C cathode attained the best Reactive Green 19 removal efficiency after 8 hours of treatment when NaCl was used. This observation was attributed to two reasons, such as NaCl reacted more readily than Na_2SO_4 and $MgSO_4$ with the OH^- formed on the photoanode to generate radicals, apart from the use of NaCl electrolyte promoted the production of ClO^- which may oxidize the azo dye molecules. Their report also mentioned that electrolytes helped PFC systems generated higher maximum power densities in comparison to PFC without them. This

was because of the greater flowability of e_{CB}^- from photoanode to cathode caused by the reduction of internal resistance of the PFC by electrolytes.

Ong et al. (2021) analyzed the effects of varying electrolyte concentrations on the performance of PFC. Four different Na_2SO_4 concentrations were addressed by them, namely 0.05 M, 0.10 M, 0.15 M and 0.20 M. The PFC demonstrated an increasing dye degradation efficiency and electricity generation with increasing Na_2SO_4 concentration. However, any increment of the Na_2SO_4 concentration beyond 0.10 M only increased the maximum power density, whereas the dye degradation rate was reported to be nearly constant. The reason given by them was that 0.10 M was the optimum condition for the operation of PFC. Furthermore, they added that Na_2SO_4 has a more significant effect on increasing electricity output instead of breaking down dyes.

2.4.2 Initial Solution pH

The pH of the initial solution is another major factor that governs the photocatalytic performance of PFC since the properties of charge on the surface of the photoelectrodes depend to a great extent on it (Lam et al., 2012). The surface of the photoelectrodes may become positively or negatively-charged, depending on the initial solution pH. Different pH values of the initial solution thus resulted in different interaction patterns between the photoelectrodes and the dye pollutants. This affected the production of radicals that aid in the degradation process of dye. Table 2.2 displays the summary of recently published works on the role of initial solution pH in affecting the photocatalytic performance of PFC.

Lee et al. (2016) investigated the performance of PFC under different initial solution pH values, which are pH 3, 5.3 and 10. Their results showed that the PFC based on a ZnO/Zn photoanode and a Pt/C cathode worked better when subjected to acidic conditions compared to alkaline conditions. They reported that pH 5.3 was the optimum condition for the PFC to operate. At pH 5.3, near-complete removal of the Reactive Green 19, which was an azo dye was achieved after a treatment period of 8

hours. Additionally, maximum power density of 0.0076 mW/cm^2 was attained. This was due to the presence of strong electrostatic attraction force, prompting more Reactive Green 19 to adsorb onto the surface of positively-charged photoanode, resulting in the PFC exhibiting a high performance. They went further to clarify that low pH encouraged recombination between electrons (e_{CB}^-) and holes (h_{VB}^+), caused by insufficient amount of OH$^-$ to promote active generation of •OH radicals. Nevertheless, at pH 10, electrostatic repulsion was the dominant force rather than electrostatic attraction. The production of radicals was obstructed, indirectly leading to high recombination rate between e_{CB}^- and h_{VB}^+.

Khalik et al. (2017) evaluated the role of pH in aiding the performance of PFC. The PFC having a ZnO/C photoanode and a Pt/C cathode was placed under pH 2, 6, 9 and 12. They found that the maximum photocatalytic efficiency of the PFC favoured to happen under pH 9, in which 49.19 % of the Reactive Black 5 was successfully removed along with the generation of maximum power density of 24.48 mW/cm^2. They explained that at pH 9, the surface of the ZnO was negatively-charged to a high degree, which easily attracted the positively-charged sulfonate groups of the Reactive Black 5, producing a high amount of •OH radicals to degrade dye pollutant and generate electricity simultaneously.

In another experiment conducted by Fu et al. (2018), the performance of PFC in degrading 4-chlorophenol, which was an organic pollutant commonly found in dyes was studied under pH 4.4, 6.4, 8.4 and 10.4. The PFC system was constructed using a Ag/TiO$_2$ photoanode, a Pt cathode and 0.05 M Na$_2$SO$_4$ electrolyte. They reported that the optimum pH was located between the range of 6.4 and 8.4, which gave rise to the highest removal rate of 4-chlorophenol (29.9 % to 32.6%) and maximum power yield, P_{max} (34.0 to 36.0 mW/m^2). They mentioned that at H 6.4, the Ag/TiO$_2$ surface was positively-charged, hence has a tendency to generate a high amount of •OH radicals, eventually increasing the performance of PFC. They elaborated that at pH 10.4, there was a lower rate of protonation, causing accumulation of negatively-charged ions at the surface of photoanode, thus inhibiting the formation of •OH radicals. While at pH 4.4, they observed that the amount of •OH radicals was inadequate, leading to the ineffectiveness of the PFC in degrading the pollutants.

Table 2.2: The Effects of Initial Solution pH on the Photocatalytic Performance of PFC.

Pollutant type	Light source	Photocatalyst	pH range	Optimum pH	Substrates degradation efficiency (%)	Maximum power density (P_{max}, mW/cm^2)	References
Reactive Green 19	UV-A	ZnO/Zn (photoanode) Pt/C (cathode)	3 - 10	5.3	~ 100	0.0076	Lee et al. (2016)
Reactive Black 5	Solar	ZnO/C (photoanode) Pt/C (cathode)	2 - 12	9.0	49.19	24.4803	Khalik et al. (2017)
4-chlorophenol	Visible light	Ag/TiO$_2$ (photoanode) Pt (cathode)	4.4 – 10.4	6.4 – 8.4	29.9 – 32.6	34.0 – 36.0	Fu et al. (2018)

2.5 Summary of Literature Review

Under the section of literature review, the fundamental characteristics of dyestuff wastewater and conventional treatment methods that may be applied to treat them have been discussed intricately. It was apparent that each type of dyestuff wastewater treatment method, whether it was physical, biological or chemical has its own pros and cons. The use of photocatalytic mechanism, which was a type of chemical treatment method has been studied thoroughly due to its potential in overcoming all the limitations commonly faced by other traditional treatment methods. The continuous investigation in this field led to the emergence of photocatalytic fuel cell (PFC). In order to set up a PFC, it was crucial to have photoelectrodes. Several fabrication methods to synthesize nanostructure-based photoelectrodes have been mentioned. In addition, the importance of modifying photoelectrodes by coupling the semiconductor with photoelectrodes was given. Thorough explanation of the process parameters of PFC such as types and initial concentration of electrolytes as well as initial solution pH was also revealed. In addition, the importance of the process parameters in ensuring the PFC system constructed exhibits high pollutants degradation efficiency and electricity generation has been justified.

Currently, no similar study has yet been conducted to investigate the treatment of dyestuff wastewater using a PFC system constructed using $NiFe_2O_4/ZnO/Zn$ as the photoanode and CuO/Cu as the cathode. Therefore, the photocatalytic performance of a novel PFC system based on $NiFe_2O_4/ZnO/Zn$ photoanode and CuO/Cu cathode will be investigated in this study.

CHAPTER 3

RESEARCH METHODOLOGY

The discussion in this chapter is centered on the setup of the experiment and the methodology employed. The flowchart as outlined in Figure 3.1 summarizes the process flow of this study.

3.1   Materials and Chemicals Review

Table 3.1 lists down all the materials and chemicals that were used during the research. These materials and chemicals were of analytical grade, meaning they did not require additional purification prior to their use in experiments.
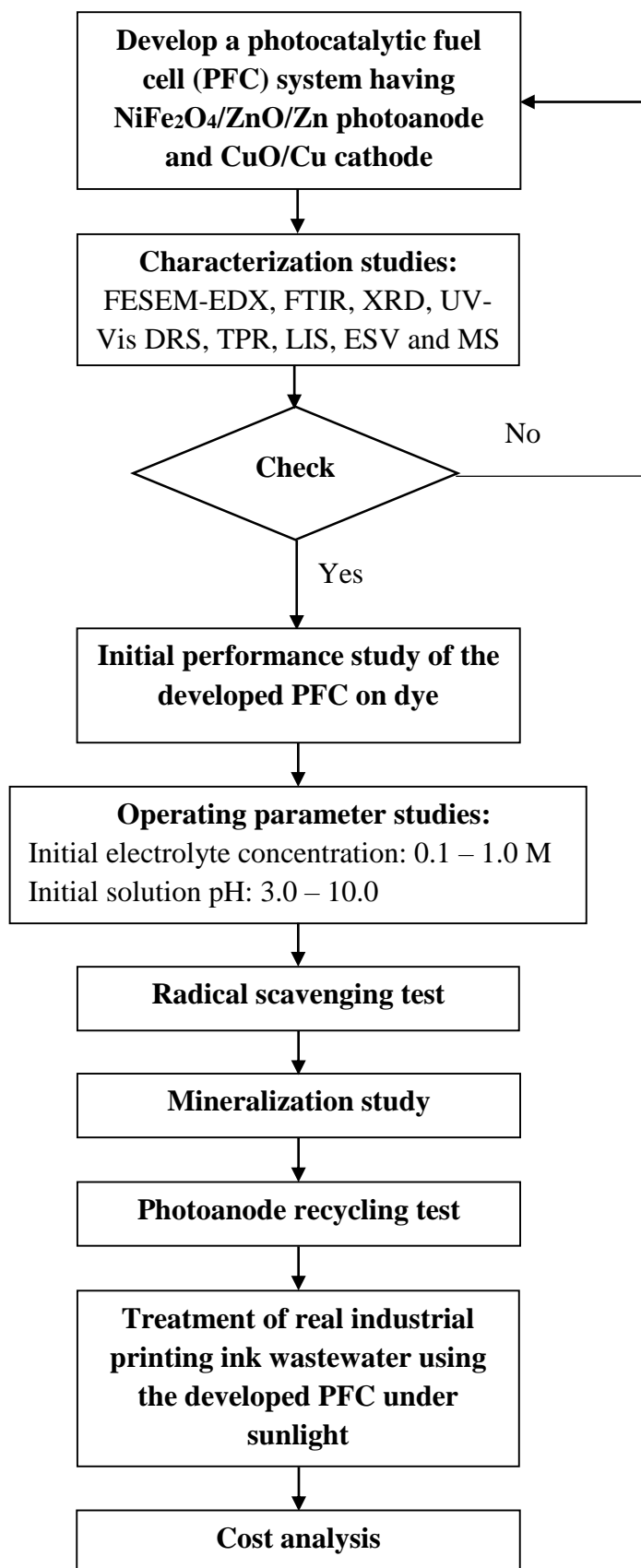
Figure 3.1: The Flow of Experimental Work Conducted in this Research.

Table 3.1: List of Materials and Chemicals Used.

Chemical / Reagent	Purity (%)	Supplier	Function
Zn Foil (0.25 mm thickness)	99.9	Strem Chemicals	Used as base plate in fabrication of photoanode.
Cu Foil (0.25 mm thickness)	99.9	Sigma-Aldrich	Used as base plate in fabrication of cathode.
Ethanol (C_2H_5OH)	95.0	ChemAR	Used for pre-cleaning of materials during photoelectrodes preparation.
Rhodamine B	-	Merck KGaA	Used as a standard dye to evaluate the effectiveness of the developed PFC system.
Zinc Nitrate Tetrahydrate [$Zn(NO_3)_2 \cdot 4H_2O$]	98	Chem Soln	Used for photoanode preparation.
Zinc Acetate Dihydrate [$Zn(CH_3COO)_2 \cdot 2H_2O$]	99.0	Chem Soln	Used for photoanode preparation.
Nickel (II) Nitrate Hexahydrate [$Ni(NiO_3)_2 \cdot 6H_2O$]	97.0	Systerm Chemicals	Used for photoanode preparation.
Iron (III) Nitrate Nonahydrate [$Fe(NO_3)_3 \cdot 9H_2O$]	98.0	GENE Chemical	Used for photoanode preparation.
Sodium Persulfate ($Na_2S_2O_8$)	99.0	BDH Laboratory Supplies	Used for cathode preparation.
Sodium Sulfate (Na_2SO_4)	99.8	Bendosen	Used as a supporting electrolyte.
Sulphuric Acid (H_2SO_4)	99.0	R&M Chemicals	Used as a pH adjuster.
Sodium Hydroxide (NaOH)	99.0	R&M Chemicals	Used as a pH adjuster.
Silver Nitrate ($AgNO_3$)	99.9	GENE Chemicals	Used for radical scavenging test.
Ethylenediaminetetraacetic Acid Disodium Salt (EDTA-2Na)	99.0	Systerm Chemicals	Used for radical scavenging test.
1,4-Benzoquinone (1,4-BQ)	98.0	Acros Organics	Used for radical scavenging test.
Isopropyl Alcohol (C_3H_8O)	95.0	GENE Chemicals	Used for radical scavenging test.
High Range (HR) COD Digestion Reagent	-	HACH	Used for COD analysis.
Real Industrial Dyestuff Wastewater	-	Hasrat Meranti Sdn. Bhd.	Used to evaluate the effectiveness of the developed PFC system in real wastewater treatment.

3.2   Apparatus and Equipment

3.2.1   Experimental Apparatus for Constructing Photocatalytic Fuel Cell (PFC)

A PFC system has been developed to treat dyestuff wastewater and generate electricity simultaneously under sunlight. The schematic diagram and actual setup of the constructed PFC are illustrated in Figures 3.2 and 3.3.

Throughout the carrying out of the research work, the PFC system was placed inside an acrylic black box, thereby forming a confinement area which effectively trapped the visible light emitted from the lamp within the box and blocked the interference from external light sources. The photoanode and cathode were connected via an external circuit of 1 kΩ titanium wire. A multimeter was joined to the external circuit mentioned earlier to measure the electrical properties of the PFC system during the photocatalytic process. The circuit was also connected to a variable resistor which functioned as a voltage regulator. Furthermore, the photoanode and cathode were separated by a fixed distance of 2 cm (Kee et al., 2018). A LED lamp (*100 W LED Flood Light IP65 Spotlight*) was used as the visible light source for the PFC and was installed on the left side of photoanode. The photoanode and light source were placed 2 cm apart to irritate and excite the photoanode (Kee et al., 2018). The performance study of the PFC was simulated inside a 100 mL beaker containing the targeted test solution. An evenly mixed test solution was maintained during the research period by placing the beaker containing the test solution and a stir bar above a magnetic stirrer, which stirred at 200 rpm. On the other hand, an air pump was used to push air into the cathode compartment. The aeration process was controlled at a constant rate of 1 L/min during the running of the experiment with the help of an air flow meter. In order to ensure the presence of proper air circulation and prevent the PFC system from overheating, two cooling fans were mounted at the side of the acrylic black box.
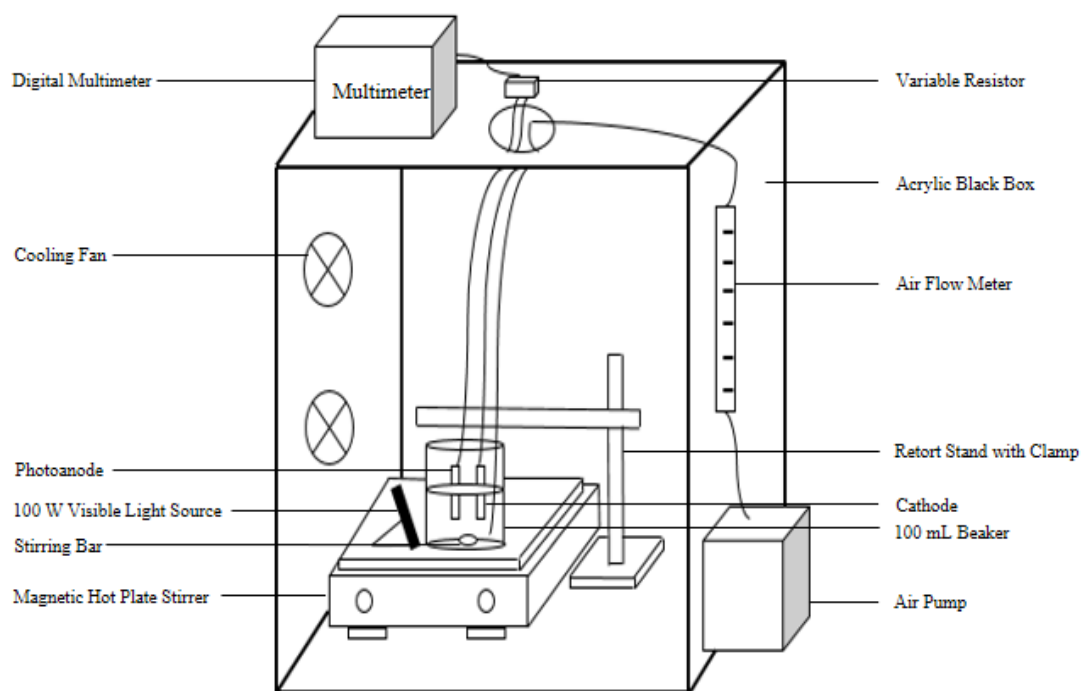
Figure 3.2: Schematic Diagram of the PFC System Setup.
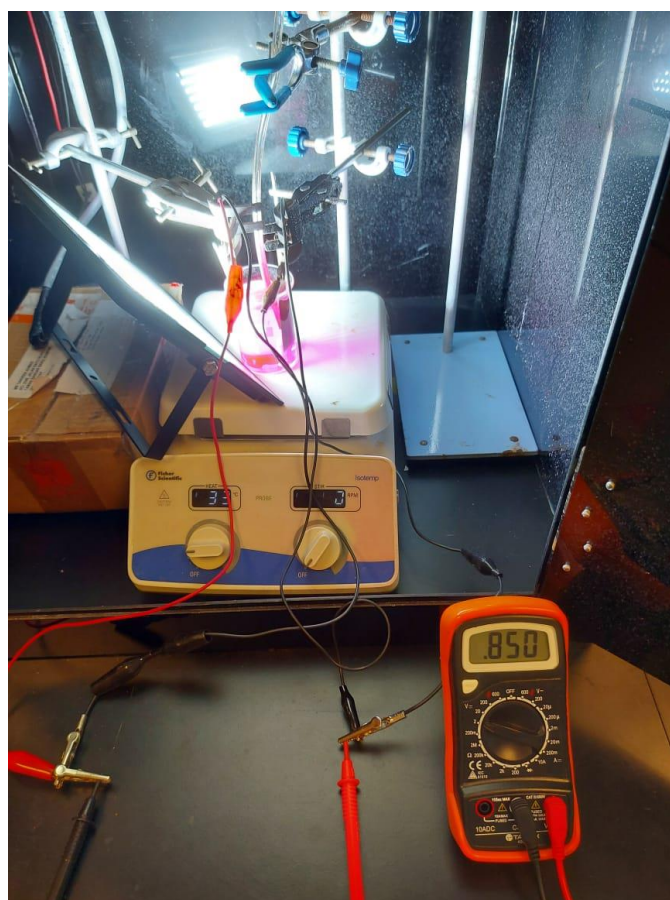
Figure 3.3: Experimental Setup of the PFC System.

3.3   Analytic Procedure

3.3.1   UV-Vis Spectrophotometer Analysis

The concentration of dye molecules present in a target sample was measured using *HACH DR6000* UV-Vis spectrophotometer. First, the absorbance of a blank sample held inside a cuvette was measured and ensured to be at zero. Then, the wavelength (λ) at the maximum absorbance value of the specific dye solution was established. After that, the wavelength of the UV-Vis spectrophotometer was adjusted to that determined earlier and the absorbance value of the test samples were measured. The light absorbance measurement by *HACH DR6000* UV-Vis spectrophotometer work in accordance with Beer-Lambert's law, in which the absorbance value of a target dye solution is directly proportional to the concentration of dye molecules present in it, as shown by Equation (3.1) below (Kittpanyangam and Eguchi, 2019).

$$A = \varepsilon c l \qquad\qquad (3.1)$$

where

A = the light absorbance at certain wavelength,

ε = the molar absorption coefficient, L/mg/cm,

c = the concentration of dye solution, mg/L,

l = the length of the dye solution through which the light pass, cm.

The synthetic dye planned to be used in this research work is Rhodamine B (RhB) with λ of 553.6 nm. The calibration curve for the RhB dye was displayed in Appendix A1.

3.3.2   Chemical Oxygen Demand (COD) Analysis

Chemical oxygen demand (COD) measures how much oxygen is required by a chemical to chemically oxidize organic matter of wastewater samples (Khan and Ali,

2018). During this research work, COD analysis was carried out on the test solution at regular intervals to determine the degradation process effectiveness of the PFC system. In order to achieve this purpose, a COD digester (*HACH DRB 200*) was used. The COD analysis was performed in accordance with COD Hach Method 8000 (HACH, 2021). First, a blank sample was produced by putting 2 mL of distilled water into a reagent vial. The function of the blank sample was to set the reading of the equipment at zero each time before measuring the COD of the other vials. Next, same volume i.e. 2 mL of the test solution was pipetted into vials at regular intervals during the running of degradation process by the PFC. After that, the vials were shaken gently to ensure even mixing before subjected to 150 °C for 2 hours inside the COD reactor. Once the digestion process was done, the vials were allowed to cool to room temperature (23 °C - 26 °C). UV-Vis spectroscopy test was then conducted using *HACH DR6000* UV-Vis spectrophotometer. As per Zhao et al. (2011), there exists a relationship between COD and UV absorbance. The accuracy of the test was improved by obtaining multiple and average COD readings for each vial. Then, the pollutants degradation efficiency of the PFC system was determined using Equation (3.2) (Xu, Liang and Zhou, 2013).

$$\text{Degradation efficiency (\%)} = \frac{COD_0 - COD_f}{COD_0} \times 100 \qquad (3.2)$$

where

COD_0 = the initial COD value, mg/L,

COD_f = the final COD value, mg/L.

3.3.3 Biological Oxygen Demand (BOD) Analysis

Biological oxygen demand (BOD) indicates how much oxygen aerobic microbes consume during their biodegradation of organic matter in wastewater over a stated time length (Li and Liu, 2019). BOD analysis was performed using the conventional closed bottle test as stipulated in ISO 5815-1:2003 and ISO 5815-2:2003 (Jouanneau et al., 2014). First, 300 mL BOD bottles were overfilled with test samples diluted with appropriate dilution factor. Then, *EUTECH DO 2700* dissolved oxygen meter was

used to determine the initial value of dissolved oxygen, DO_0 of the test sample in the BOD bottle. Next, the BOD bottle was sealed airtight using paraffin film to prevent air from entering or leaving the test sample contained in it, preventing any disruption to the oxygen content (Dewata and Zainul, 2015). The sealed BOD bottle was then incubated inside *VELP SCIENTIFICA FOC 225E* incubator at 20 °C for five days. 5-days incubation period was preferred as it was the accepted standard worldwide for BOD analysis (Dewata and Zainul, 2015; Dahamsheh and Wedyah, 2017). After 5-days incubation period, the dissolved oxygen of the test sample, DO_5 inside the BOD bottle was once again measured. BOD_5 was then obtained using Equation (3.3) as follows (Patel and Vashi, 2015).

$$BOD_5 = \frac{DO_0 - DO_5}{\text{Dilution factor}} \tag{3.3}$$

where

DO_0 = the initial DO value, mg/L,

DO_5 = the final DO value measured after 5-days incubation period, mg/L.

3.3.4 Turbidity Analysis

Turbidity analysis is used to measure the clarity level of a test sample through identification of suspended particles present in it based on the light-scattering principle by the particles (De Roos et al., 2017). *Lovibond* turbidimeter was used when measuring the turbidity of the test sample. In the first place, calibration was done on the turbidimeter with standard solutions. Next, the turbidity vial was filled with well-mixed test solution up to the marked line on the side of the vial. The vial was ensured to be dry as well as free of air bubbles and fingerprints to ensure accuracy in the readings obtained. All the turbidity readings were measured in Nephelometric Turbidity Units (NTU). Multiple readings were taken to obtain an average.

3.4   Preparation of Photoelectrodes

3.4.1   Preparation of Photoanode

A two-step method was used for the preparation of novel $NiFe_2O_4/ZnO/Zn$ photoanode, namely electrodeposition followed by hydrothermal synthesis process (Rahmayeni et al., 2016; Stumpp et al., 2018; Yong et al., 2021). Initially, ethanol solution was used to clean a Zn plate measuring 7.5 cm × 2.0 cm through ultrasonic method. Then, the cleaned Zn plate was rinsed with distilled water. Next, ZnO seed solution was prepared by mixing 20 mM of zinc acetate together with 10 mM of sodium hydroxide inside a 50 mL ethanol solution. Subsequently, the mixture was heated at 100 °C for 1 hour under continuous stirring. After that, the ZnO seed solution was casted onto the Zn plate using a dropper and calcined at 300 °C for 1 h.

Electrodeposition was then carried out by allocating the casted Zn plate as the working electrode and a plain Zn plate as the counter electrode using *GW Instek GPS-3303* bench power supply. The electrolyte solution used in this case was prepared by dissolving 0.15 g of zinc nitrate inside a 100 mL distilled water. The electrolyte solution was then heated and once its temperature reached 80 °C, electric current of 0.01 A and voltage of 1.1 V were applied for a duration of 2 h. Important precaution step during the electrodeposition process was that every 20 minutes, the microbubbles sticking on the Zn plates must be removed. The synthesized ZnO/Zn photoanode was then dried in oven and calcined at 400 °C for 1 h.

For the synthesis of $NiFe_2O_4$ nanoparticles, first 10 mM nickel nitrate and 20 mM iron nitrate were mixed inside 100 mL distilled water using magnetic stirrer for 30 minutes. Then, 2 M NaOH solution was used to adjust the mixture's pH to 12. Subsequently, the mixture was heated at a constant temperature of 180 °C for 7 h. Once finished heating, the products were allowed to cool down, followed by rinsing with distilled water and drying at 70 °C for 2 h. After that, NiFe2O4 nanoparticles whose mass was 2.5 % of that of the ZnO layer were mixed in 80 mL deionized water for 10 minutes using an ultrasonic homogenizer. The ZnO/Zn photoanode was then immersed inside the suspension with the surface coated with ZnO layer facing upwards, followed by heating at a constant temperature of 120 °C for 7 h. The synthesized

NiFe$_2$O$_4$/ZnO/Zn photoanode was allowed to cool down followed by rinsing with distilled water and drying at 70 °C for 2 h. Figure 3.4 illustrates the procedure involved in the photonaode preparation.

Ultrasonic cleaning of Zn plate with ethanol

↓ Rinsing with distilled water and leave aside for drying

Cleaned Zn plate

↓

Preparing ZnO seed solution

↓

Loading ZnO seed solution onto Zn plate using drop casting

↓

Setting up of electrochemical cell:
Working electrode: Zn plate casted with ZnO seed layer solution
Counter electrode: Plain Zn plate
Electrolyte solution: Zinc nitrate solution

↓

Electrodeposition for 2 h at 0.01 A and 1.1 V under 80 °C

↓

Oven-drying followed by calcining at 400 °C for 1 h

↓

Nanostructure-based ZnO/Zn photoanode

↓

Preparing mixture of 10 mM Ni(NiO$_3$)$_2$•6H$_2$O, 20 mM Fe(NO$_3$)$_3$•9H$_2$O and 100 mL distilled water

↓ Adjusting the pH to 12 using 2 M NaOH

Heating at a constant temperature of 180 °C for 7 h, followed by rinsing with distilled water and drying at 70 °C for 2 h

↓

NiFe$_2$O$_4$ nanoparticles

↓

Preparing mixture of NiFe2O4 nanoparticles whose mass was 2.5 % of that of the ZnO layer with 80 mL deionized water

↓

Heating the loaded Zn plate inside the mixture at a constant temperature of 120 °C for 7 h, followed by rinsing with distilled water and drying at 70 °C for 2 h

↓

Nanostructure-based $NiFe_2O_4/ZnO/Zn$ photoanode

Figure 3.4: Procedure Followed During Preparation of NiFe₂O₄/ZnO/Zn Photoanode.

3.4.2   Preparation of Cathode

Wet chemical method was used to prepare CuO/Cu cathode (Wang et al., 2010; Gawande et al., 2016; Kee et al., 2018). First, a Cu plate that measures 7.5 cm $\times$ 2.0 cm was prepared. Ultrasonic cleaning using ethanol was then carried out to clean the surface of the Cu plate, followed by rinsing with distilled water. Once the Cu plate was ensured to be completely dry, it was left soaked inside a mixture consisting of 2.5 M NaOH and 0.125 M $Na_2S_2O_8$. When 30 minutes has passed, the Cu plate was again rinsed with distilled water to ensure there was no presence of excess residue. The Cu plate was then placed under two consecutive heating processes, which are oven-drying at 90 °C for 24 h, subsequently furnace-calcining at 450 °C for 1 h. The process flow in Figure 3.5 summarizes the wet chemical method used to prepare the cathode.

```
┌─────────────────────────────────────────────┐
│   Ultrasonic cleaning of Cu plate with ethanol │
└─────────────────────────────────────────────┘
                    │        Rinsing with distilled water and
                    │        leave aside for drying
                    ▼
┌─────────────────────────────────────────────┐
│              Cleaned Cu plate                 │
└─────────────────────────────────────────────┘
                    │        Submerging inside a mixture of 2.5
                    │        M NaOH and 0.125 M Na₂S₂O₈
                    ▼
┌─────────────────────────────────────────────┐
│       Drying in an oven at 90 °C for 24 h     │
└─────────────────────────────────────────────┘
                    │
                    ▼
┌─────────────────────────────────────────────┐
│     Calcining in a furnace at 450 °C for 1 h  │
└─────────────────────────────────────────────┘
                    │
                    ▼
┌─────────────────────────────────────────────┐
│        Nanostructure-based CuO/Cu cathode     │
└─────────────────────────────────────────────┘
```
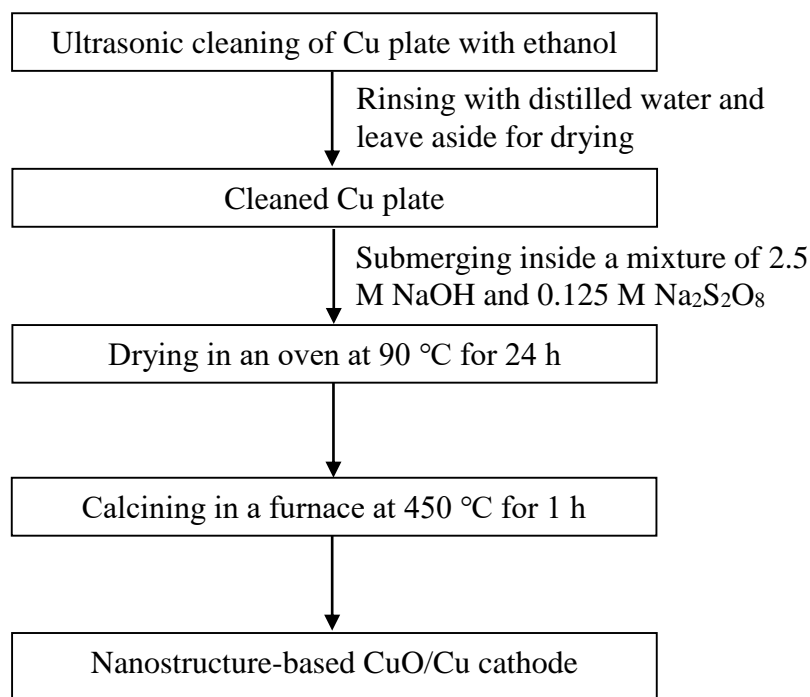
Figure 3.5: Procedure Used During Preparation of CuO/Cu Cathode.

3.5   Characterization of Photoelectrodes

3.5.1   Surface Morphology Analysis

The surface morphology of the photoelectrodes was determined by conducting field emission scanning electron microscopy with energy dispersive X-ray spectroscopy (FESEM-EDX) analysis. The electron microscope model used for this purpose was *JEOL JSM-6701F* FESEM. FESEM-EDX analysis was done to obtain information regarding the surface structure of the photoelectrodes such as crystallite size (Asha et al., 2020). A clean and dry surface was ensured for the samples before analysis. The samples were then properly fixed on a sample holder using carbon tape. A thin layer of platinum was applied as a conductive material. FESEM-EDX analysis was performed at the laboratory of Faculty of Science, UTAR, Perak Campus.

3.5.2 Functional Group Analysis

Fourier transform infrared spectroscopy (FTIR) was used to identify the molecular structure and functional groups of the nanostructure-based semiconductor photoelectrodes (Rao et al., 2020). FTIR analysis was conducted with the aid of a *Perkin Elmer Spectrum RX-1* FTIR spectrometer. Initially, the photocatalyst samples were ground until a fine powder was obtained. Next, the product was mixed with powdered KBr through grinding process again. The mixture was then fitted and pressed properly into the die set, which acts as a mould to form a pellet-shaped test sample. FTIR analysis was performed at the laboratory of Faculty of Science, UTAR, Perak Campus.

3.5.3 Crystalline Phase Analysis

X-ray diffraction (XRD) analysis was employed to determine the degree of crystallinity in the structure of the photocatalyst samples (Duta et al., 2013). Firstly, the photocatalyst samples were ground until a fine powder was obtained. Incident X-ray irradiation was then shot towards the samples. Various intensities of the diffracted X-ray beams were thus obtained at angles of 2 θ, which represents the angle between the diffracted beam and incident beam. FTIR analysis was conducted at the laboratory of Faculty of Science, UTAR, Perak Campus using *Shidmazu 6000* X-ray diffractometer.

3.5.4 Band Gap Potential Analysis

The band gap potential of photocatalyst samples were measured using UV-Vis diffuse reflectance spectroscopy (UV-Vis DRS) analysis. UV-Vis DRS test was carried out using *HACH DR6000* UV-Vis spectrophotometer. The wavelength used to scan through the sample ranged from 200 to 800 nm. UV-Vis DRS analysis was conducted at the laboratory of Faculty of Environment and Green Technology, UTAR, Perak

Campus.

3.5.5 Photoelectrochemical Experiments

The photoelectrochemical tests, which included transient photocurrent response (TPR), linear sweep voltammetry (LSV), electrochemical impendence spectroscopy (EIS) and Mott-Schottky (MS) were used to analyze the photocatalyst samples via *Gamry Interface 1000* potentiostat electrochemical workstation. A conventional three-electrode system was employed in this workstation. The electrodes used were fluorine-doped tin oxide (FTO) glass coated with fabricated photocatalysts (working electrode), platinum foil (counter electrode), Ag/AgCl (reference electrode). Besides that, the workstation was immersed inside a 0.5 M Na_2SO_4 supporting electrolyte solution throughout the analysis and irradiated using a 105 W compact fluorescent lamp. All of the aforementioned tests were conducted under light illumination, except MS test. The photoelectrochemical tests were conducted at the laboratory of Faculty of Science, UTAR, Perak Campus.

3.6 PFC System Constructed Using NiFe₂O₄/ZnO/Zn Photoanode and CuO/Cu Cathode

In contemplation of developing a more environmentally-sound dyestuff wastewater treatment technique, the dye removal efficiency and power generation ability of a PFC system having $NiFe_2O_4$/ZnO/Zn photoanode and CuO/Cu cathode was evaluated. In this research work, 100 mL of the dyestuff solution was poured into a beaker and placed inside an acrylic black box. Two-thirds of the 7.5 cm $\times$ 2.0 cm photoelectrodes were immersed inside the targeted wastewater solution. Constant aeration rate of 1 L/min was provided to the cathode all the time the experiment was going on. Prior to the conduct of the photocatalytic experiment, the dyestuff wastewater was required to be stirred in the dark for about 30 minutes. This was to ensure the realization of an adsorption-desorption equilibrium state between the dye particles and the

photocatalysts (Andronic et al., 2020; Vasiljevic et al., 2020). Once the aforesaid equilibrium was achieved, the photoanode was irradiated by turning on the visible-light lamp set at 2 cm from it. In order to evaluate the effectiveness of the photocatalytic degradation of the PFC, test samples were extracted at regular intervals using a pipette. After the samples were centrifuged, colour removal analysis was then done in order to assess the photodegradation efficiency of the PFC system using Equation (3.4) (Sangpour, Hashemi and Moshfegh, 2010).

$$\text{Degradation efficiency (\%)} = \frac{C_0 - C_f}{C_0} \times 100 \tag{3.4}$$

where
C_0 = the initial dye concentration value, mg/L,
C_f = the final dye concentration value, mg/L.

For the electrical values measurement, a *NJTY T-33* mini digital multimeter was used. The generated voltage and electric current flowing across the circuit connected with 1 kΩ variable resistor was determined. The power density output of the PFC system was computed based on the following Equation (3.3) (Fu et al., 2018).

$$\text{Power density} = \frac{I \times V}{A} \tag{3.2}$$

where
I = current,
V = voltage,
A = surface area of the photoanode, m^2.

3.7 Process Parameter Studies

The effectiveness of the developed PFC system in degrading dyestuff wastewater and inducing electricity will be assessed through varying parameters such as concentration

of electrolyte used and initial solution pH. Variations will be made to only one process parameter at a time, while other parameters will remain constant.

3.7.1 Concentration of Electrolyte Used

The involvement of electrolyte in PFC system is important as it increases the conductivity of the dyestuff wastewater involved, promoting the formation of oxidative radicals and subsequently achieving higher pollutant removal efficiency (Kee et al., 2018). In this research work, the electrolyte type and its amount used were made constant. For interpreting the performance of the PFC, different Na_2SO_4 electrolyte concentrations were used, specifically 0.1, 0.2, 0.5 and 1.0 M. The electrolyte volume added was fixed at 10 mL. The electrolyte and its concentrations were selected with regard to the research performed by Lee et al. (2016) and Ong et al. (2021). In this context, the initial concentration of the dyestuff wastewater was ensured to be at 5 mg/L with pH fixed at natural.

3.7.2 Initial Solution pH

Another dominant factor that affects the performance of PFC system is initial solution pH, which plays a major role in determining the charge properties on the surface of photoelectrodes (Lam et al., 2012). Based on the past research done by Lee et al. (2016), Khalik et al. (2017) and Fu et al. (2018), the range of pH chosen for the initial solution was pH 3 to 10. This was to determine the optimum pH condition for the PFC to function well, whether under natural, acidic, neutral or alkaline setting. Alteration of the initial solution pH was carried out using 1.0 M HCl solution and 1.0 M NaOH solution under the help of *HANNA Instruments HI* 2550 *pH/ORP/EC/TDS/NACL* benchtop meter. In this study, the initial concentrations of the dyestuff wastewater and the Na_2SO_4 electrolyte used were ensured to be at 5 mg/L and 0.5 M, respectively.

3.8 Radical Scavenging Test

Radical scavenging test was conducted to determine the most dominant reactive species involved in carrying out photocatalytic degradation of dye pollutants (Zhang and Zhang, 2013). Initially, test samples were extracted at regular intervals and centrifuged to remove unwanted particles. After that, UV-Vis analysis was done to obtain the initial dye concentration. A scavenger species was then added to the sample and the final dye concentration was measured. Next, degradation efficiency was obtained based on Equation (3.4). The lower the pollutant degradation efficiency due to the presence of a specific quencher, the more significant the role of the corresponding scavenged radical species. Table 3.2 lists down the generally used scavenger compounds and their targeted radical species. All the scavenger chemicals used in the research study were of 0.2 mM (Pereira et al., 2019).

Table 3.2: List of Commonly Used Radical Scavengers (Pelaez et al., 2016).

Radical Scavenger Compound	Targeted Radical Species
EDTA 2Na	h^+
Silver nitrate	e^-
1,4-benzoquinone (BQ)	$\bullet O_2^-$
Isopropyl alcohol (IPA)	$\bullet OH$

3.9 Real Industrial Dyestuff Wastewater Study

In an attempt to further justify the effectiveness of the developed PFC, it was employed in real industrial dyestuff wastewater treatment. The real wastewater used in this study was sourced from a local printing company, Hasrat Meranti Sdn. Bhd. located at Chemor, Perak. A huge quantity of dyestuff wastewater was collected to ensure sufficient supply for study purpose. In order to prevent the sunlight from interfering with the wastewater during collection process, a dark-coloured storage container was used. It was filled to the brim and sealed airtight to prevent aeration from occurring. Preservation was done by storing the container in a 4 °C freezer (Kee et al., 2018). Parameters as stated in the earlier parts such as BOD, COD and so forth were used to

analyze the real wastewater. The performance of the PFC system in treating the real wastewater was then assessed under natural sunlight using optimum electrolyte concentration and initial solution pH as determined earlier through standard dyes.

CHAPTER 4

RESULTS AND DISCUSSION

This chapter focused on the experimental results of the research study. First and foremost, characterization studies on the $NiFe_2O_4/ZnO/Zn$ photoanode and CuO/Cu cathode that were employed in the PFC system will be addressed through various analysis techniques. Subsequently, preliminary studies of the PFC system will be emphasized. The following section dealt with the performance of the PFC system with regards to dye pollutants degradation efficiency and amount of electricity generation under various process parameters such as concentration of electrolyte and initial solution pH. The succeeding section concentrated on the radical scavenging test, accompanied by mineralization study of the PFC system under optimum conditions as determined earlier. In order to gauge the stability of the developed $NiFe_2O_4/ZnO/Zn$ photoanode against continuous usage, recycling test will be conducted. After that, the photodegradation performance of the PFC system under direct sunlight was further assessed via real industrial printing ink wastewater. Lastly, cost analysis to fabricate the $NiFe_2O_4/ZnO/Zn$ photoanode and CuO/Cu cathode was conducted to study their economic feasibility in real-life applications.

4.1   Characterization of Photoelectrodes

Characterization of both photoelectrodes that were used in the developed PFC system was performed to analyze their physiochemical properties, which are instrumental in explaining the efficiency of the PFC system. The surface morphology and elemental composition of the photoelectrodes were identified through FESEM-EDX analyses. Besides that, FTIR analysis was executed to distinguish the functional groups present in the $NiFe_2O_4/ZnO/Zn$ photoanode and CuO/Cu cathode. In addition, XRD analysis were conducted to verify the crystallinity and phase purity degree of $NiFe_2O_4/ZnO/Zn$ photoanode and CuO/Cu cathode. In addition, UV-Vis DRS analysis was employed to measure the band gap potential of the photocatalyst. Furthermore, photoelectrochemical analysis was carried out to evaluate the electrochemical reaction of synthesized photoanode towards light irradiation. Under this part, the charge separation and transfer efficiency was studied through analyses such as TPR, LSV, EIS and MS.

4.1.1   Surface Morphology Analysis

Figures 4.1a and b depict the morphology of $NiFe_2O_4/ZnO/Zn$ photoanode obtained under different magnifications of FESEM analysis. As evidenced from the figures, the ZnO attached on the surface of Zn foil appeared to be tree-shaped. This unique hierarchical structure provided a larger surface area for the attachment of granular $NiFe_2O_4$ nanoparticles. Moreover, a deeper inspection of the figures revealed that the $NiFe_2O_4$ nanoparticles were densely packed over the ZnO layer. Furthermore, the sizes of the ZnO branches were found to be ranging from 310 nm to 5930 nm, whereas the sizes of the $NiFe_2O_4$ particles were established to fluctuate from 64 nm to 239 nm.
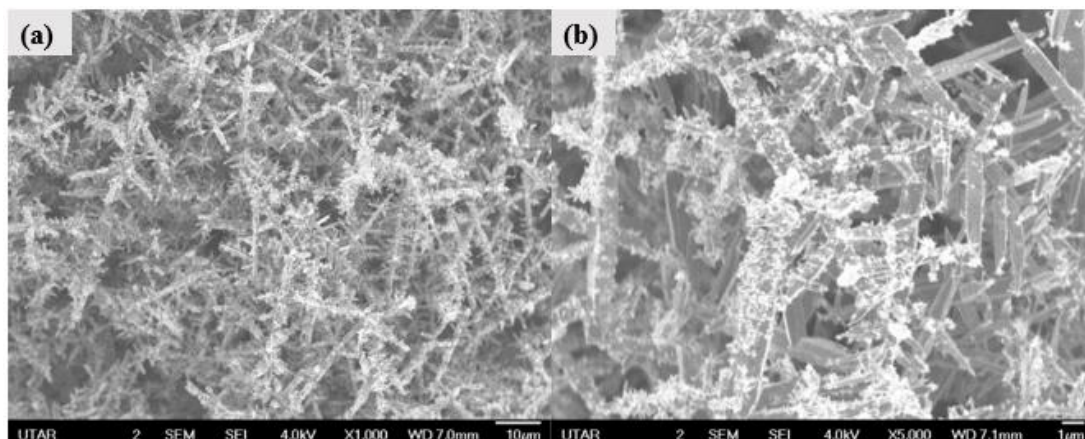
Figure 4.1: FESEM Images of NiFe$_2$O$_4$/ZnO/Zn Photoanode Under Magnification of (a) ×1,000 and (b) ×5,000.

Similarly, Figures 4.2a and b portray the morphological characterisation of CuO/Cu cathode under various magnifications. As represented in the figures, the rod-shaped CuO nanoparticles were uniformly distributed over the copper plate. Besides that, the measured sizes of the CuO particles varied from 91 nm to 392 nm.
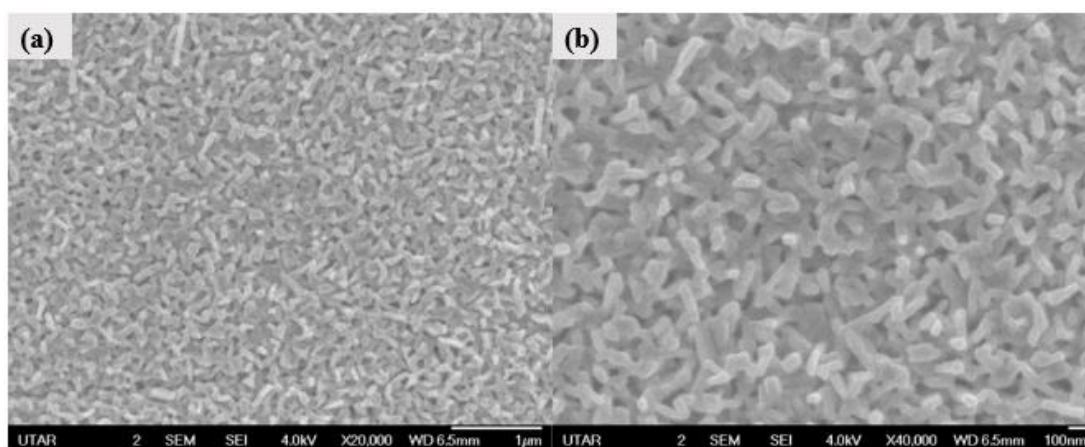
Figure 4.2: FESEM Images of CuO/Cu Cathode Under Magnification of (a) ×20,000 and (b) ×40,000.

4.1.2 Elemental Composition Analysis

The elemental composition of NiFe$_2$O$_4$/ZnO/Zn photoanode and CuO/Cu cathode were monitored through EDX analysis. The EDX spectra, which were reflected in

Figures 4.3a and b revealed that $NiFe_2O_4/ZnO/Zn$ photoanode composed of Ni, Fe, Zn and O elements, while the CuO/Cu cathode constituted of Cu and O elements. Besides that, the obtained results showed no other impurities were detected, implying that the $NiFe_2O_4$ and ZnO of the photoanode as well as CuO of the cathode were of high purity. The Ni, Fe, Zn and O elements in the photoanode sample were determined to have weight percentages in the following proportions: 1.33 %, 4.15 %, 57.68 % and 36.84 %. On the other hand, the weight percentages of Cu and O in the cathode were 61.86 % and 38.14 %.
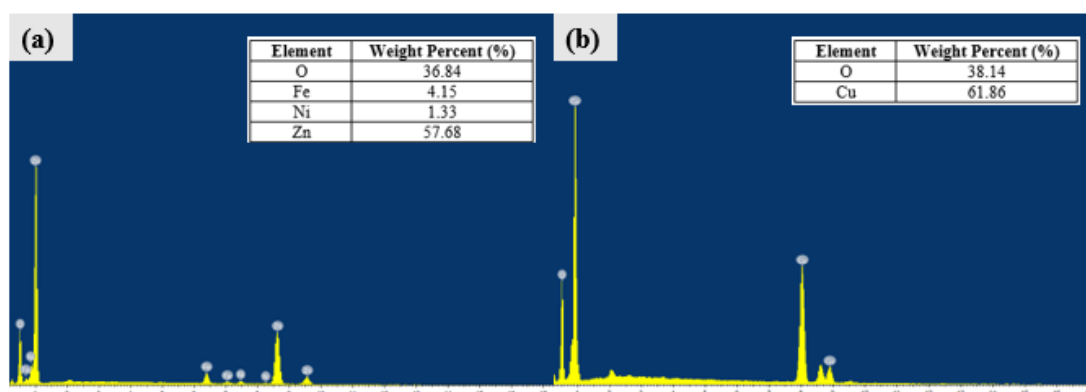
Figure 4.3: EDX Spectra of (a) NiFe₂O₄/ZnO/Zn Photoanode and (b) CuO/Cu Cathode.

4.1.3   Functional Group Analysis

Figures 4.4a and b disclose the FTIR spectra of $NiFe_2O_4/ZnO/Zn$ photoanode and CuO/Cu cathode. The absorption peak located at 3411 cm^{-1} as noted in Figure 4.4a were due to the stretching vibration of O-H groups, indicating the presence of water molecules on both the external and internal surfaces of the $NiFe_2O_4/ZnO/Zn$ photoanode (Harish et al., 2017). The detection of O-H groups verified that •OH radicals were possible to be formed from the reaction between H_2O molecules and h_{VB}^{+} during photoexcitation process. Besides that, the peak noticed at 867 cm^{-1} was attributed to the ionic vibrations of $NiFe_2O_4$ (Tiwari et al., 2020). In addition, the absorption peak observed at 540 cm^{-1} was credited to the stretching vibration of Zn-O bond in the photoanode (Król et al., 2017; Moradi, Fardood and Ramazani, 2018).
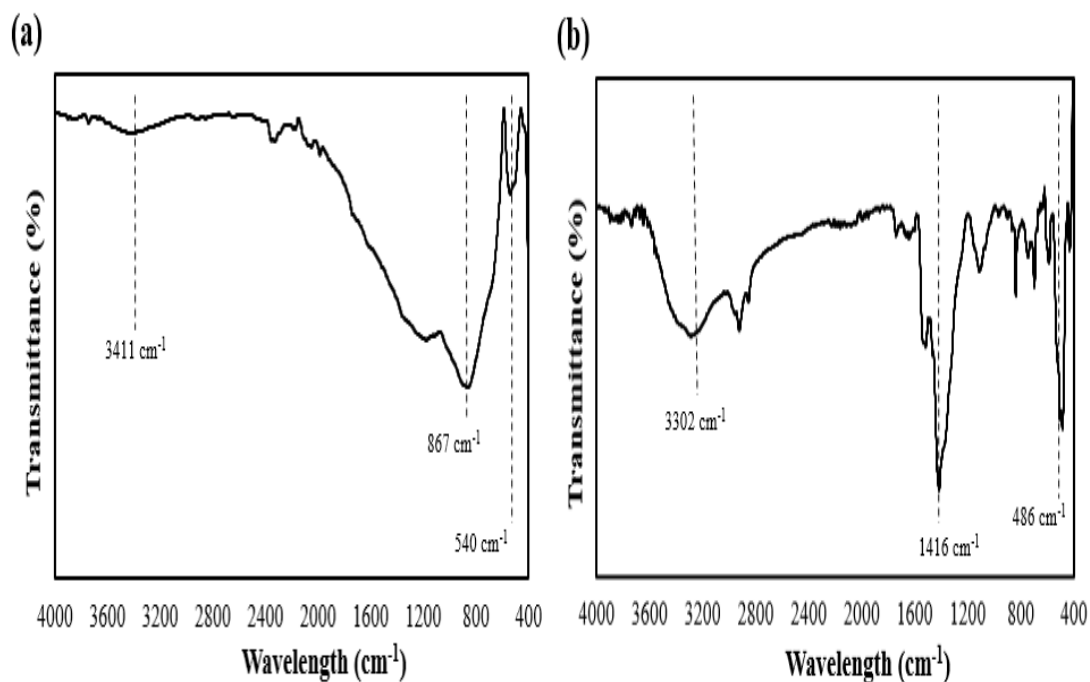
Figure 4.4: FTIR Spectra of (a) NiFe₂O₄/ZnO/Zn Photoanode and (b) CuO/Cu Cathode.

According to Figure 4.4b, several absorption peaks were revealed as well for the CuO/Cu cathode. The absorption peaks shown at 3392 cm^{-1} and 1416 cm^{-1} were attributed to the stretching vibration of O-H groups caused by the absorption and adsorption of water molecules on the surface of CuO/Cu cathode (Harish et al., 2017; Rao et al., 2017). Another prominent peak located at 486 cm^{-1} corresponded to the existence of CuO-Cu bond in the cathode (Rao et al., 2017).

4.1.4 Crystalline Phase Analysis

The crystalline structure of the NiFe₂O₄/ZnO/Zn photoanode and CuO/Cu cathode were characterized through XRD analysis. Figure 4.5 displays the XRD pattern of ZnO/Zn photoanode, NiFe₂O₄ powder and NiFe₂O₄/ZnO/Zn photoanode. The sharp, narrow and intense peaks exhibited by all the samples indicted that their structures were well crystallized. The diffraction peaks observed for ZnO/Zn were at 31.61 ° (100), 34.27 ° (002), 36.11 ° (101), 47.39 ° (102), 56.45 ° (110) and 64.89 ° (104). The identified ZnO/Zn peaks in this research work were in agreement with that reported by

Ullah et al. (2013), Zhu et al. (2016) and He et al. (2018b), confirming the phase purity of ZnO/Zn.

Moreover, the distinct diffraction peaks spotted for $NiFe_2O_4$ powder were at 18.44 ° (111), 30.30 ° (220), 35.70 ° (400), 43.38 ° (400), 57.38 ° (511), 63.02 ° (440) and 74.56 ° (533). The characteristic peaks obtained were in agreement with that reported by Zhu et al. (2016) and He et al. (2018b), which verified the absence of impurities. In the case of composite $NiFe_2O_4$/ZnO/Zn photoanode, the diffraction peaks located at (100), (002), (101), (102), (110) and (104) were attributed to ZnO/Zn, while those demonstrated at (400) and (553) were accredited to $NiFe_2O_4$, thus indicating the successful loading of $NiFe_2O_4$ nanoparticles onto the ZnO/Zn layer to form hybrid $NiFe_2O_4$/ZnO/Zn photoanode.
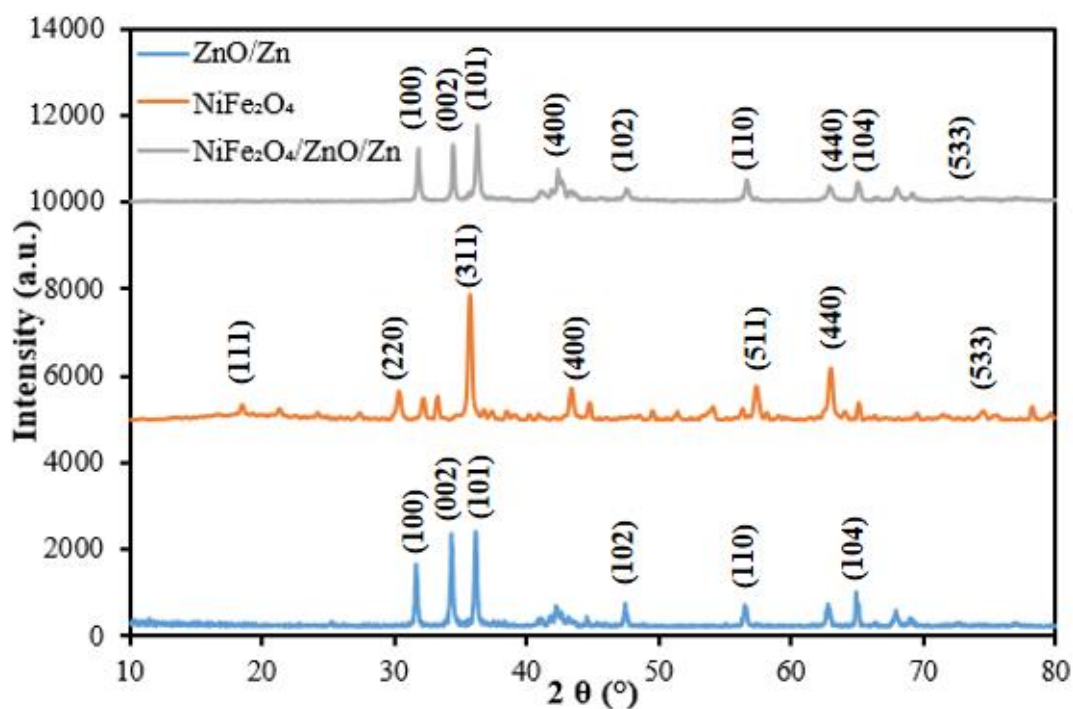
Figure 4.5: XRD Pattern of ZnO/Zn Photoanode, NiFe₂O₄ Powder and NiFe₂O₄/ZnO/Zn Photoanode.

Figure 4.6 shows the XRD pattern of CuO/Cu cathode. The diffraction peaks observed for CuO/Cu were at 31.89 ° (110), 35.79 ° (111), 38.99 ° (111), 42.69 ° (200), 49.69 ° (202) and 72.67 ° (221). All the observed peaks were due to the presence of Cu substrate. The identified CuO/Cu peaks in this research work were in line with that reported by Kee et al. (2018).
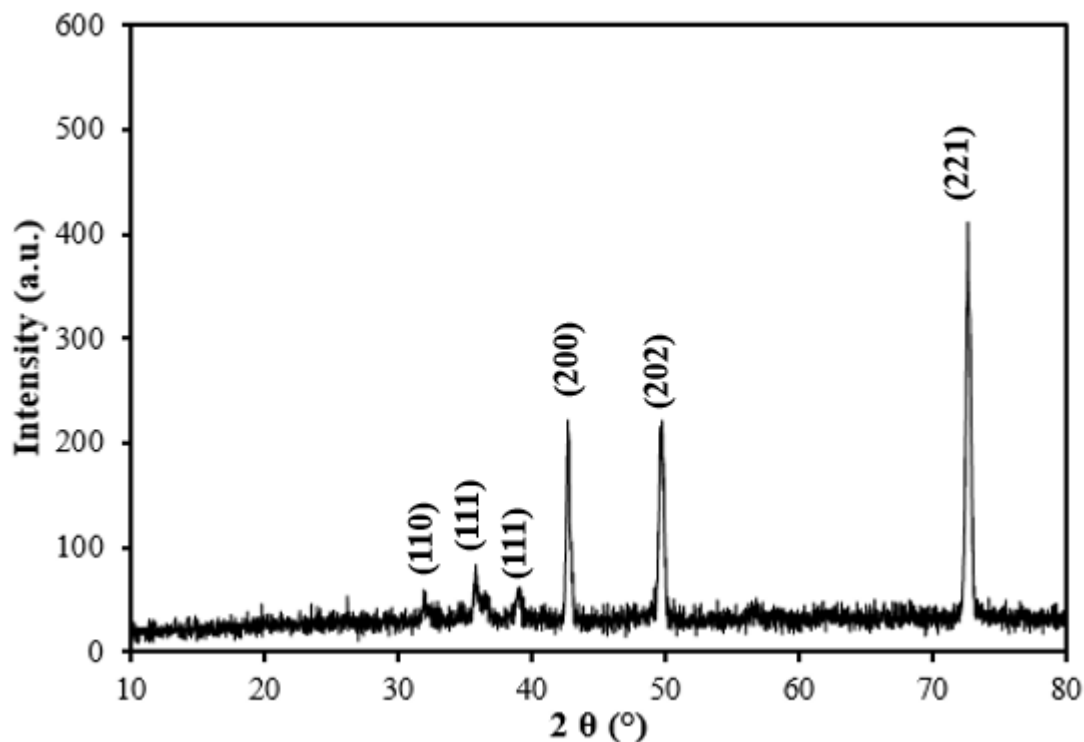
Figure 4.6: XRD Pattern of CuO/Cu Cathode.

4.1.5 Band Gap Potential Measurement

Figure 4.7 delineates the UV-Vis DRS spectra of ZnO, NiFe$_2$O$_4$ and NiFe$_2$O$_4$/ZnO. Through drawing a tangent to each of the graph and finding their x-intercepts, the band gap potential, E_g of ZnO, NiFe$_2$O$_4$ and NiFe$_2$O$_4$/ZnO were successfully determined to be 3.1 eV, 2.3 eV and 1.9 eV, respectively. This confirmed that the coupling of ZnO and NiFe$_2$O$_4$ successfully lowered the wide band gap of ZnO, which could allow higher effectiveness in separation efficiency of e_{CB}^{-}-h_{VB}^{+} pairs by improving the visible light harvesting effectiveness and therefore increasing the rate of photoexcitation (Wang et al., 2016; Zhang et al., 2016; Li et al., 2021a).
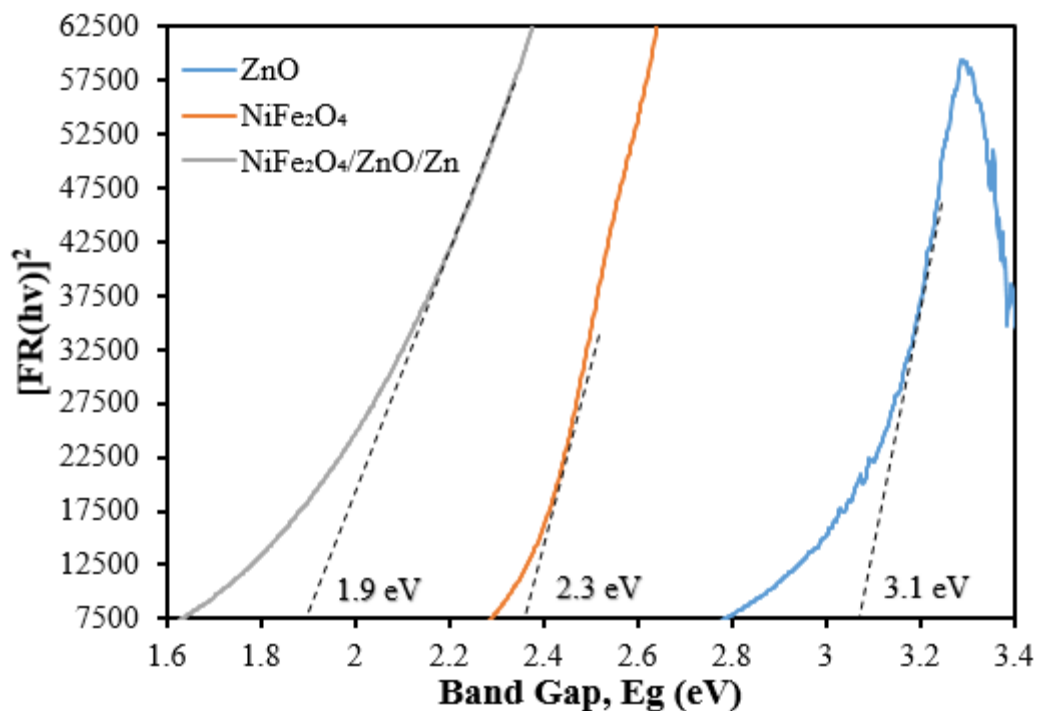
Figure 4.7: UV-Vis DRS Spectra of ZnO, NiFe₂O₄ and NiFe₂O₄/ZnO.

4.1.6 Photocurrent Density Measurement

The photocurrent density output of pure ZnO and composite NiFe$_2$O$_4$/ZnO was determined through TPR analysis. Figure 4.8 reveals the TPR results for the samples over five continuous cycles of alternately switching on and off the visible light. The two samples displayed good photoresponse with both of them initiated light generation immediately after the providence of light. Nevertheless, the composite NiFe$_2$O$_4$/ZnO clearly demonstrated better photoresponse compared to the pure ZnO. This justified that under the presence of visible light, the hybrid NiFe$_2$O$_4$/ZnO was able to rapidly undergo photoexcitation process, which led to better separation efficiency of e_{CB}^--h_{VB}^+ pairs, thus allowing higher electricity generation (Wang, Li and Zhang, 2019; Jiang et al., 2020).
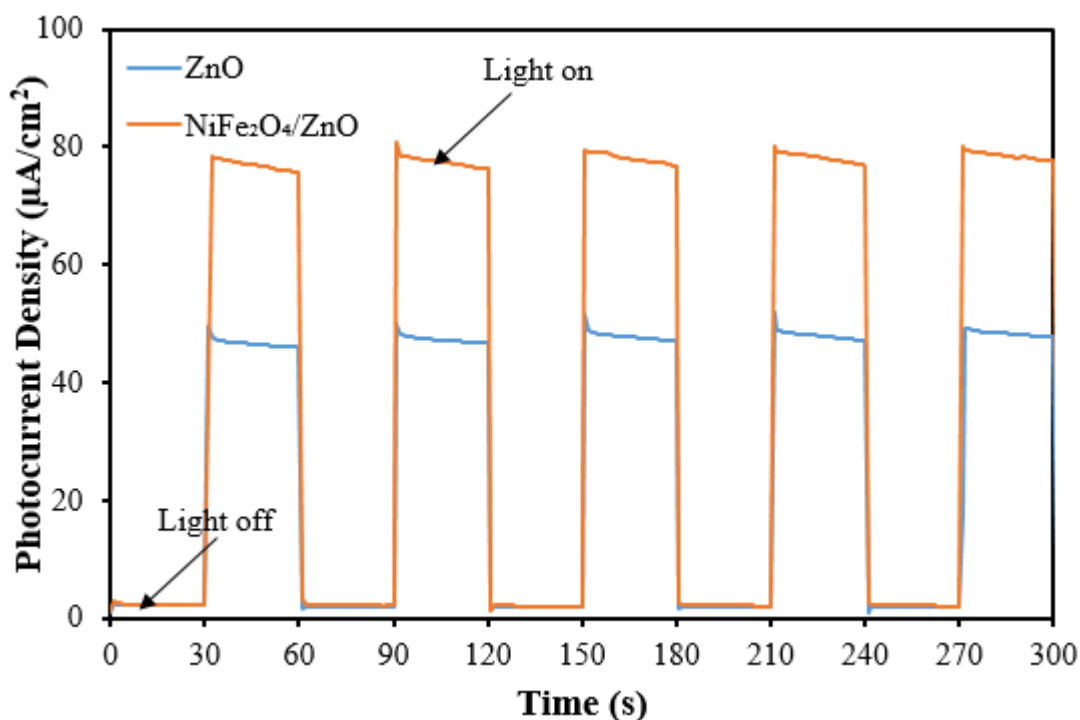
Figure 4.8: Photocurrent Density Measurement of Pure ZnO and Composite NiFe₂O₄/ZnO Through TPR Analysis.

Apart from that, the results obtained from LSV analysis as portrayed in Figure 4.9 have also proven that composite NiFe$_2$O$_4$/ZnO achieved higher photocurrent density than pure ZnO. This supplemented the fact that when exposed to visible light, hybrid NiFe$_2$O$_4$/ZnO was able to undergo photoexcitation process much easier than bare ZnO, which would hinder the recombinant of e_{CB}^--h_{VB}^+ pairs, thus facilitating the detachment of e_{CB}^- to induce electricity production.
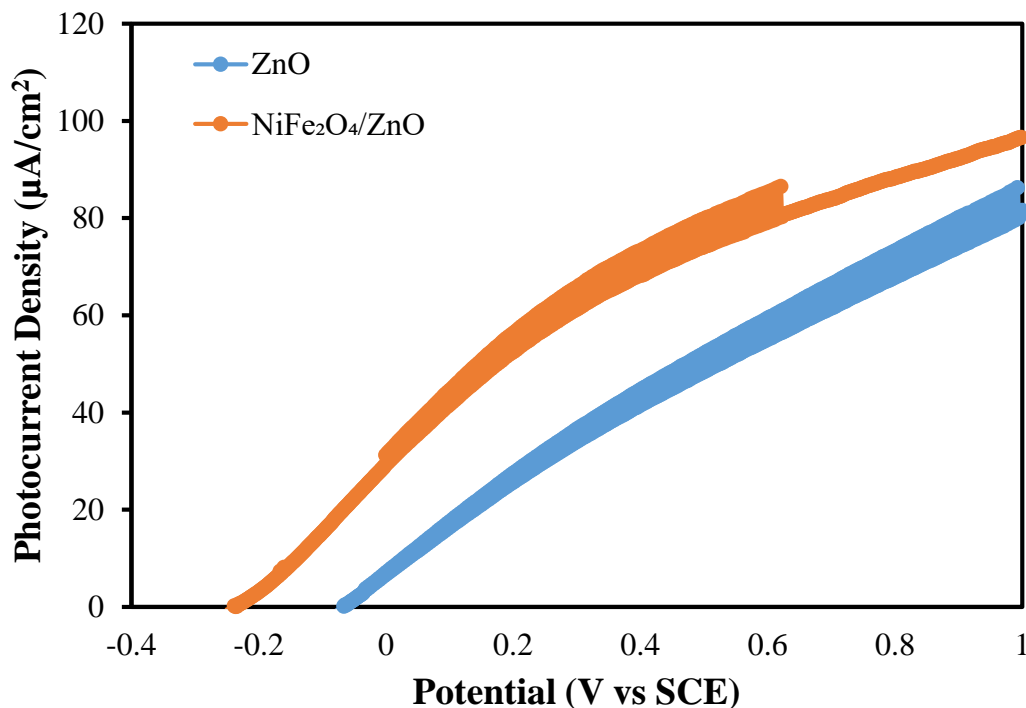
Figure 4.9: Photocurrent Density Measurement of Pure ZnO and Composite NiFe₂O₄/ZnO Through LSV Analysis.

4.1.7 Interfacial Charge Transfer Measurement

In order to further evaluate the charge separation and transfer efficiency of pure ZnO and composite NiFe$_2$O$_4$/ZnO, EIS analysis was conducted. Figure 4.10 portrays the Nyquist plots obtained for ZnO and NiFe$_2$O$_4$/ZnO in the absence of light. The results obtained indicated that the internal charge transfer resistance of NiFe$_2$O$_4$/ZnO was lower than ZnO, evidenced by the smaller arc radius of its plot (Sin et al., 2020). This smaller charge transfer resistance indicated that coupling of NiFe$_2$O$_4$ with ZnO helped to promote easier separation of e_{CB}^{-}-h_{VB}^{+} pairs at the photoanode interface, thus enhancing the interfacial solid-liquid reaction.
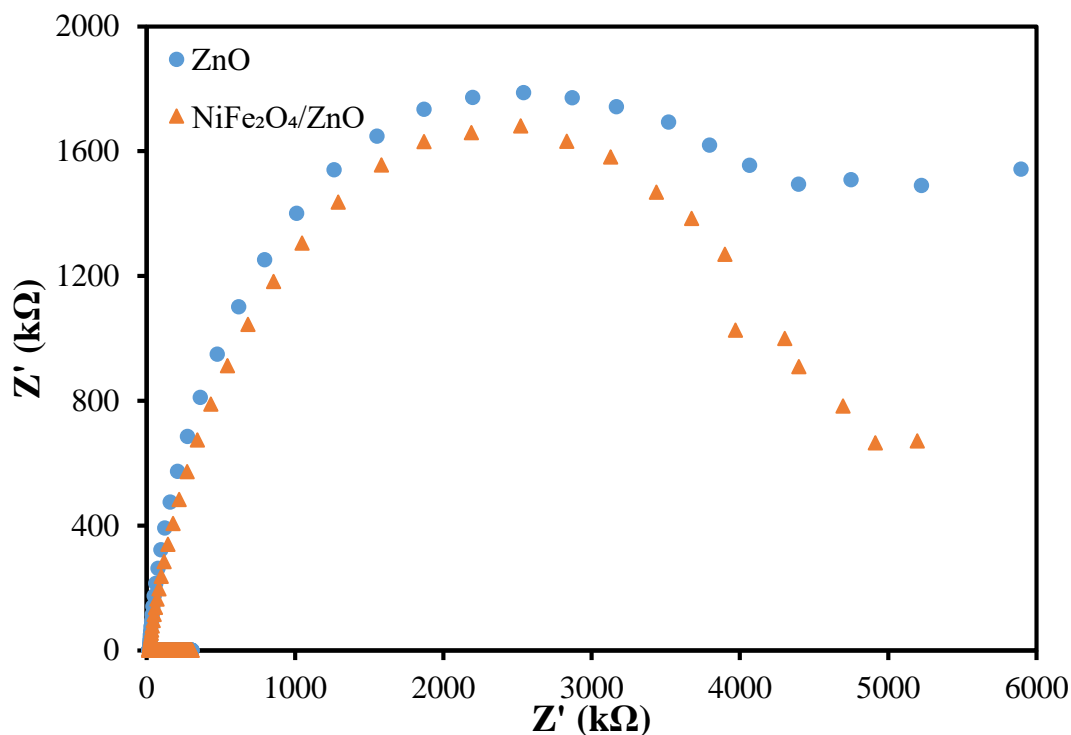
Figure 4.10: Nyquist Plots of Pure ZnO and Composite NiFe₂O₄/ZnO Under Dark Condition.

4.1.8   Conduction Band (CB) Potential Measurement

The conduction band (CB) potential, E_{CB} of ZnO and NiFe$_2$O$_4$ were determined through MS analysis. Figure 4.11 illustrates the MS plots for ZnO and NiFe$_2$O$_4$. In order to obtain the E_{CB} values, x-intercept was determined for each of the plot through interpolation of line tangent to the graph. The E_{CB} values for ZnO and NiFe$_2$O$_4$ were - 0.1 eV and - 0.55 eV, respectively. The CB values determined in this research work matched with the literature reported by Zhu et al. (2016). Since the band gap potential, E_g of ZnO and NiFe$_2$O$_4$ determined earlier through UV-Vis DRS were 3.1 eV and 2.3 eV, respectively, thus the valence band (VB) potential, E_{VB} for ZnO and NiFe$_2$O$_4$ were computed to be 3.0 eV and 1.75 eV using Equation (4.4) (Sim et al., 2018). According to Bhosale et al. (2019), the obtainment of a MS plot having a negative gradient means that the semiconductor is of n-type, whereas MS plot with positive gradient corresponds to p-type semiconductor. Thus, it was deduced that both ZnO and NiFe$_2$O$_4$ synthesized in this research work are p-type semiconductors since their MS plots

indicated negative slopes.

$$E_{VB} = E_{CB} + E_g \qquad (4.4)$$

where

E_{VB} = the valence band (VB) potential, eV,

E_{CB} = the conduction band (VB) potential, eV,

E_g = the band gap potential, eV.
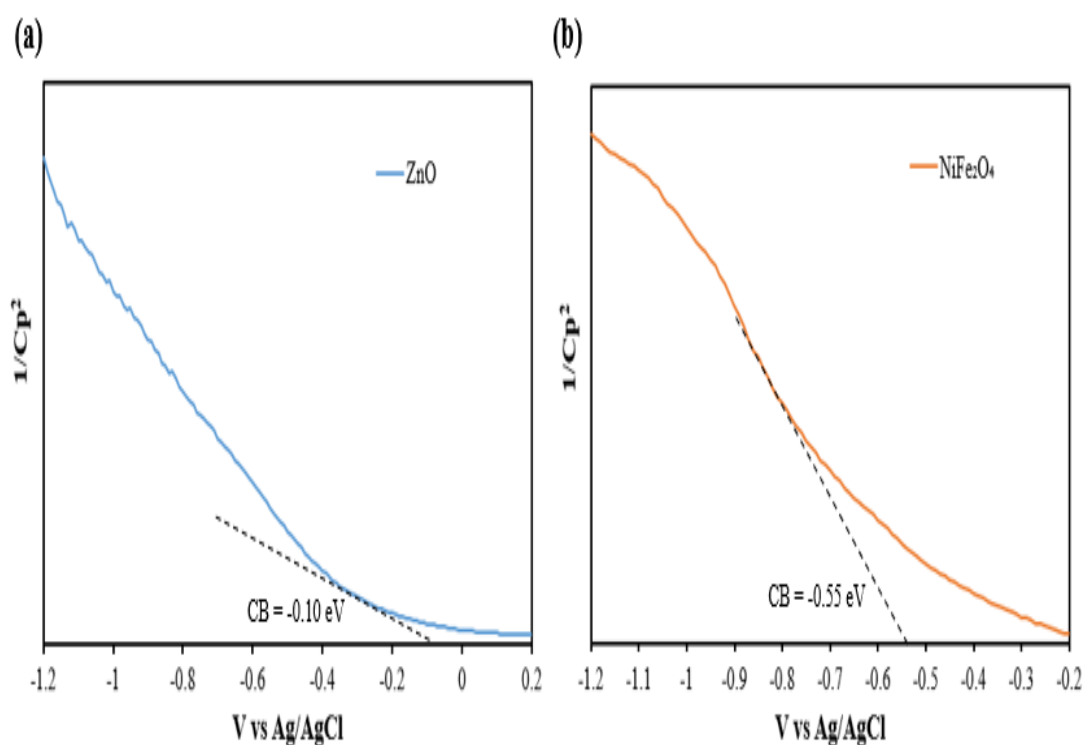
Figure 4.11: MS Plots of (a) ZnO and (b) NiFe₂O₄.

4.2 Preliminary Studies of PFC System

In this research work, Rhodamine B (RhB) was designated as the synthetic dye to gauge the pollutant degradation effectiveness of the constructed PFC system. Figure 4.12 presents the photodegradation of RhB dye subjected to different conditions. The photolysis process exhibited a mere degradation rate of 11 % after 240 minutes of irradiation time using visible light. However, RhB removal efficiency of 31 % was

achieved within 240 minutes of visible light irradiation when using the PFC system made up of ZnO/Zn photoanode and CuO/Cu cathode. Nevertheless, the RhB degradation efficiency further increased to 47 % after similar irradiation time when adopting 2.5 % NiFe$_2$O$_4$/ZnO/Zn as the photoanode for the developed PFC system.
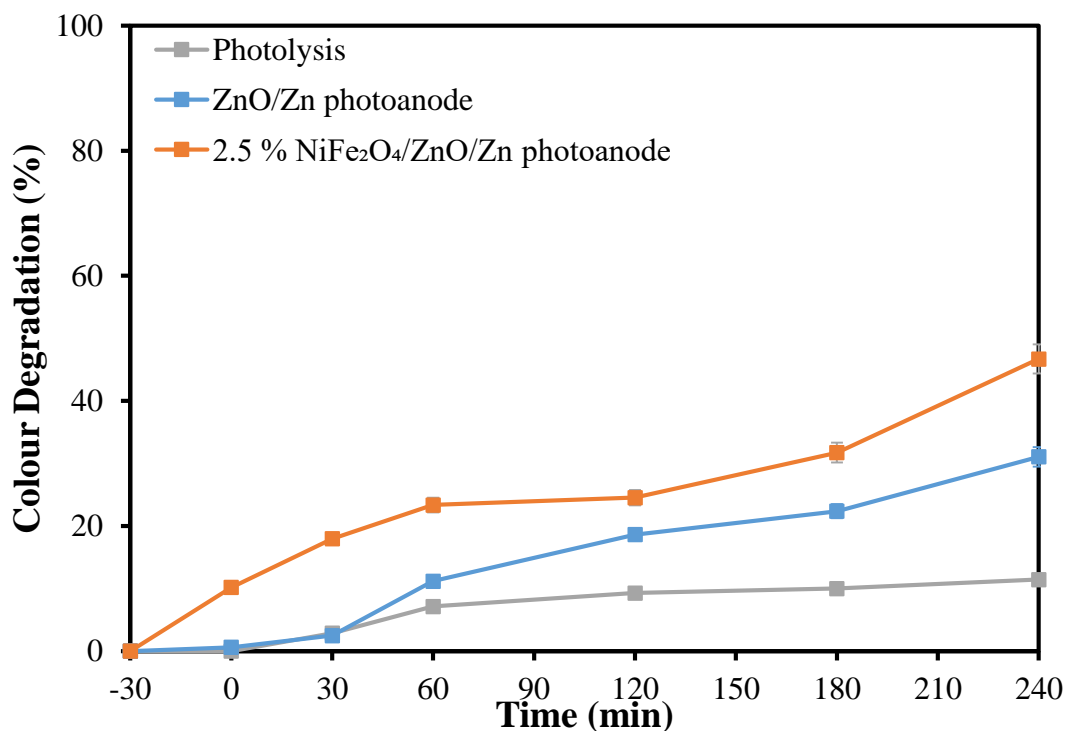
Figure 4.12: Photocatalytic Degradation of RhB Dye Using PFC System ([RhB] = 5 mg/L; Solution pH = 5.3).

The photolysis process showed an insignificant influence on the degradation of RhB, which was mainly ascribed to its decent photostability under visible light (Li et al., 2014). This affirmed that RhB barely underwent self-decomposition under visible light irradiation. This obtained result was in conformity with the studies conducted by Chankhanittha and Nanan (2021) as well as Ullah, Viglašová and Galamboš (2021).

In comparison, the higher colour degradation rate of RhB witnessed after the application of PFC system involving ZnO/Zn photoanode was predominantly due to the generation of highly reactive •OH and •O$_2^-$ radicals from oxidation of H$_2$O and O$_2$. When illuminated by visible light, the photoanode lined with photocatalysts on its surface underwent photoexcitation action. This initiated the generation of $e_{CB}^- $-$h_{VB}^+$

pair by the photoanode and concurrently encouraged the e_{CB}^- to flow by dint of an external circuit to the cathode, preventing the recombination of e_{CB}^--h_{VB}^+. At the same time, the h^+ remaining at the photoanode produced •OH radicals through reaction with H_2O, while the e_{CB}^- flowed to the aerated cathode reacted with O_2 to generate •O_2^- radicals, which were capable of decomposing the dye molecules (Kee et al., 2018; Vasseghian et al., 2020).

Contradictorily, the further enhancement of the photocatalytic degradation efficiency of RhB by the PFC system when adopting 2.5 % $NiFe_2O_4$/ZnO/Zn as the photoanode was accounted to increased separation effectiveness of e_{CB}^--h_{VB}^+. This strongly indicated that the coupling of $NiFe_2O_4$ with ZnO successfully formed a hybrid that has a better separation and transfer rate of e_{CB}^--h_{VB}^+ pair (Li et al., 2015). The photogenerated electrons in both $NiFe_2O_4$ and ZnO were readily excited from their respective valence band (VB) to conduction band (CB), leaving behind the detached photogenerated holes (He et al., 2018b). The results obtained in this part were vindicated by that achieved during the characterization studies of pure ZnO and composite $NiFe_2O_4$/ZnO/Zn.

Figure 4.13 compares the electricity generation efficiency of the PFC system between pure ZnO/Zn and composite $NiFe_2O_4$/ZnO/Zn photoanodes. It was observed that the electricity generation performance improved notably when using the latter. The open circuit voltage (V_{oc}) was enhanced from 436 mV to 606 mV, whereas short circuit current density (J_{sc}) increased from 0.0044 mA/cm^2 to 0.0069 mA/cm^2. In addition, the maximum power density (P_{max}) surged from 0.0004 mW/cm^2 to 0.0010 mW/cm^2. The coupling of $NiFe_2O_4$ and ZnO nanoparticles improved the absorption of visible light, leading to higher photoreactivity (He et al., 2018b). This resulted in the efficient transferring of e_{CB}^- from photoanode to cathode compartment, thus suppressing the recombination of e_{CB}^--h_{VB}^+ and generating higher electricity (Adeleke et al., 2018). The above results strongly suggested that photocatalytic performance adopting $NiFe_2O_4$/ZnO/Zn photoanode exceeding that of photolysis and even in the case of using bare ZnO/Zn photoanode.
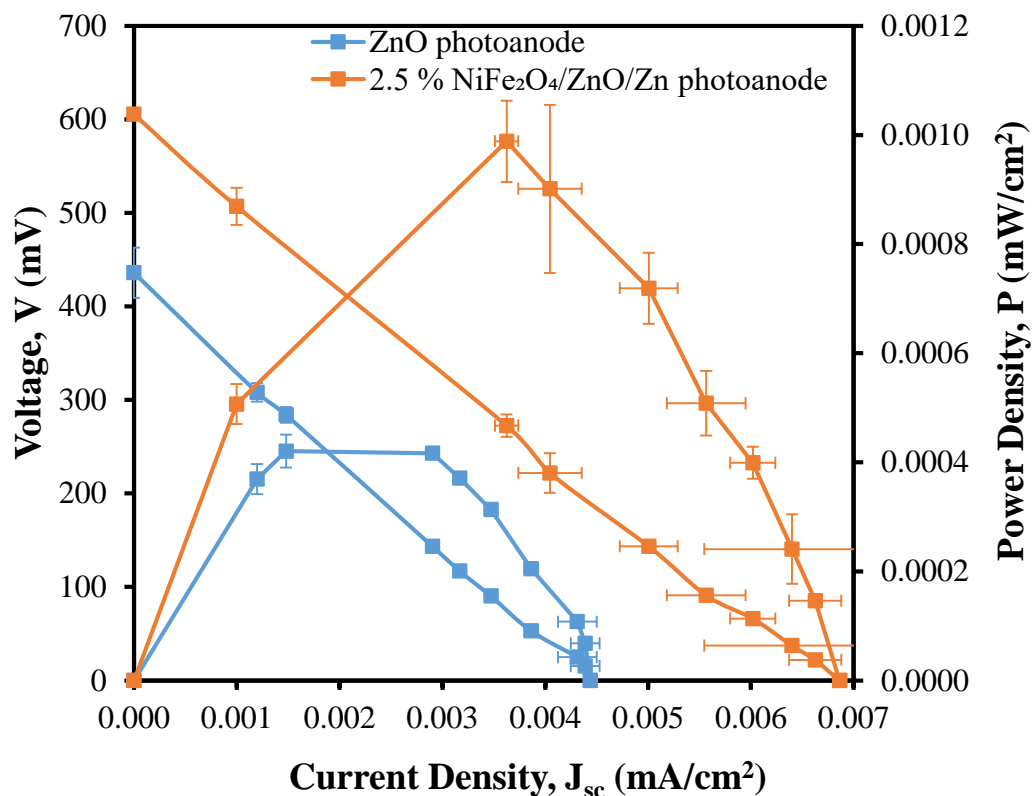
Figure 4.13: The Difference Between Bare ZnO and NiFe₂O₄/ZnO/Zn Photoanodes on Electricity Generation by the PFC System ([RhB] = 5 mg/L; ZnO Loading = 0.5 g/L; NiFe₂O₄ Loading = 2.5 %; Solution pH = 5.3).

Consistent findings also reported by other researchers. Hu et al. (2017) validated that employing TiO_2/Sn_3O_4 heterojunction successfully attained higher photocatalytic ability than using each of them alone. In addition, Chankhanittha et al. (2021) mentioned that fabrication of ZnO/Bi_2WO_6 exhibited improved photocatalytic performance compared to pure ZnO. Therefore, composite $NiFe_2O_4/ZnO/Zn$, which displayed better photocatalytic performance was selected over ZnO/Zn and employed in the following studies.

4.2.1 Effect of Open and Closed Circuit

In an attempt to understand the mechanism of e_{CB}^- transfer, the PFC system was assessed under the conditions of open and closed circuit. For open circuit study, the photoanode and cathode were not connected. Meanwhile, closed circuit analysis was

conducted by linking the photoanode and cathode via an external circuit joined to a 1000 Ω resistor. As per Figure 4.14, the PFC system achieved degradation of RhB dye in both open and closed circuit PFC system. The degradation rate of RhB dye was 32 % in the open circuit PFC system within 240 minutes of irradiation time, while 47 % of RhB dye removal was attained for the closed circuit PFC system within the same time interval.
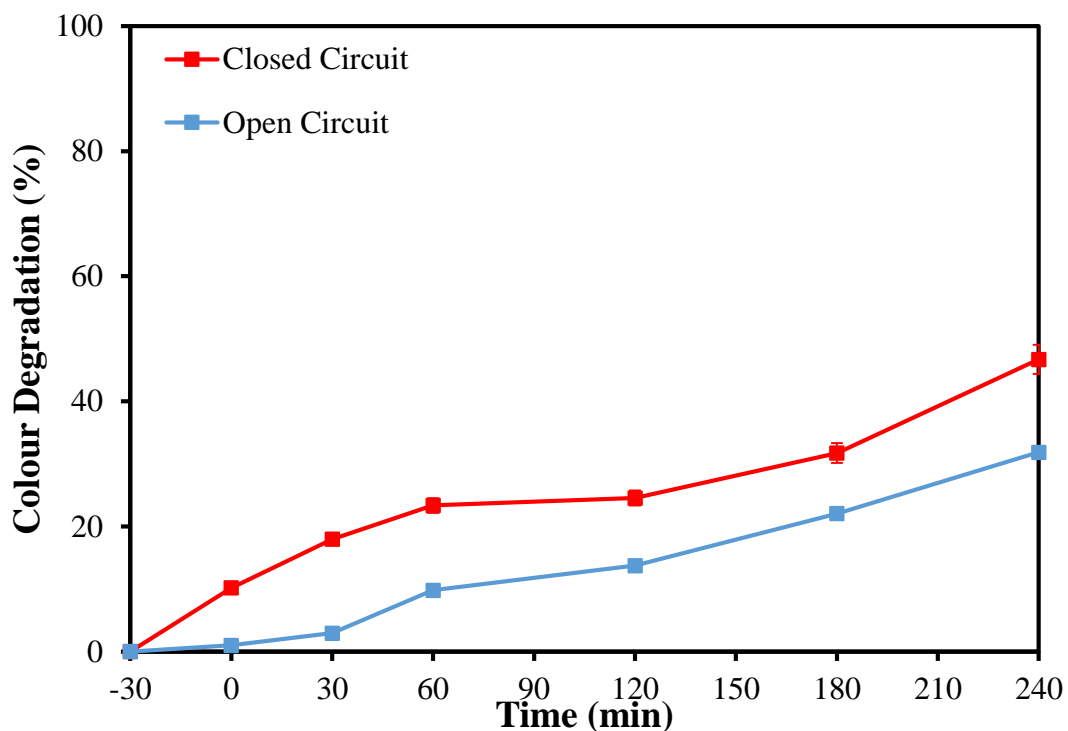
Figure 4.14: The Effect of Open and Closed Circuit on Photocatalytic Degradation of RhB Dye Using PFC System ([RhB] = 5 mg/L; Solution pH = 5.3).

Upon irradiation by the incoming light photons, e_{CB}^{-}-h_{VB}^{+} pair was formed at the photoanode compartment. The generated h_{VB}^{+} reacted with H_2O to form •OH radicals, which subsequently degraded the RhB dye molecules and caused discolouration in both open and closed circuit PFC system. Nevertheless, the removal efficiency of RhB was higher in closed circuit PFC system than that of open circuit PFC system. One of the justifications for this scenario was due to the encouragement of e_{CB}^{-} to flow from the photoanode and cathode owing to the existence of potential bias, which could ameliorate the problem of frequent recombination of e_{CB}^{-}-h_{VB}^{+} (Lee et al., 2016b). Furthermore, the e_{CB}^{-} arrived at the cathode reacted with O_2 providing •O_2^{-} radicals, leading to higher oxidation of RhB dye molecules (Lee et al., 2016c). On

the contrary, in the condition of open circuit PFC system, the e_{CB}^- produced were bound within the photoanode compartment, thus aggravating the recoupling rate of e_{CB}^--h_{VB}^+ and limiting the yielding of •OH radicals.

4.2.2 Effect of NiFe₂O₄ Loading of Photoanode

Modification of the dosage of $NiFe_2O_4$ added on the ZnO/Zn photoanode was used as the means of evaluating the effect of catalyst loading on the performance of the PFC system, with all other parameters held constant. The measured weight of the ZnO layer coated on the surface of Zn film was 0.05 g, while the weight of 2.5 %, 5 % and 10 % $NiFe_2O_4$ loaded on ZnO layer were 0.00125 g, 0.0025 g and 0.005 g, respectively. The data in Figure 4.15 indicates that using 5 % $NiFe_2O_4$/ZnO/Zn photoanode achieved the highest colour removal efficiency of 55 %. This was followed by 46 % attained for 2.5 % $NiFe_2O_4$/ZnO/Zn and 42 % obtained in the case of 10 % $NiFe_2O_4$/ZnO/Zn.
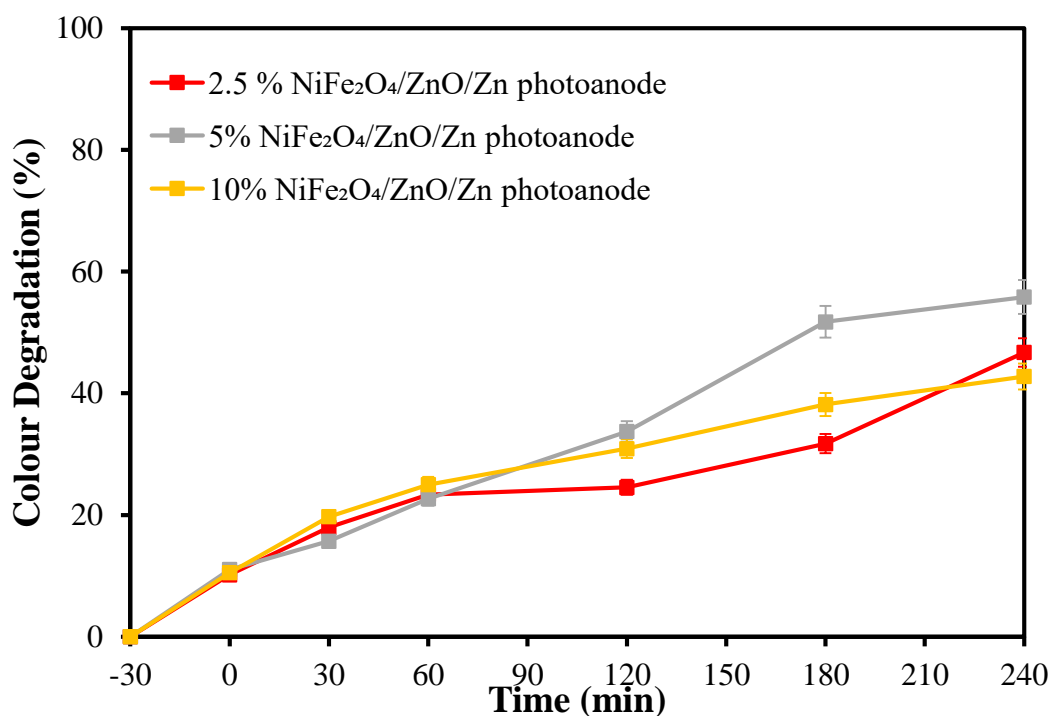
Figure 4.15: The Effect of NiFe₂O₄ Loading of NiFe₂O₄/ZnO/Zn Photoanode on the Colour Removal Efficiency of RhB Dye Using PFC System ([RhB] = 5 mg/L; ZnO Loading = 0.5 g/L; Solution pH = 5.3).

Figure 4.16 presents the performance of electricity generation of PFC system under the condition of altering amounts of $NiFe_2O_4$ catalyst added to fabricate $NiFe_2O_4/ZnO/Zn$ photoanode. The electricity performance improved as the $NiFe_2O_4$ loading increased from 2.5 % to 5 %, which then declined although the $NiFe_2O_4$ dosage was further increased from 5 % to 10 %. When replacing the 2.5 % $NiFe_2O_4/ZnO/Zn$ photoanode with 5 % $NiFe_2O_4/ZnO/Zn$ photoanode, the V_{oc} witnessed a slight increase from 605 mV to 611 mV, whereas the J_{sc} intensified from 0.0069 mA/cm^2 to 0.0081 mA/cm^2 and P_{max} improved from 0.0010 mW/cm^2 to 0.0011 mW/cm^2. However, contrasting scenario was noted in the case of using 10 % $NiFe_2O_4/ZnO/Zn$ photoanode, in which the PFC system experienced a drop in performance of electricity generation. The V_{oc} reduced from 611 mV to 578 mV, while the J_{sc} slumped from 0.0081 mA/cm^2 to 0.0067 mA/cm^2 and P_{max} dipped from 0.0011 mW/cm^2 to 0.0009 mW/cm^2. The results deduced that the photoanode with optimum $NiFe_2O_4$ loading was 5 % $NiFe_2O_4/ZnO/Zn$ photoanode, which demonstrated the highest degradation rate of RhB and electricity generation efficiency among all the photoanodes with varied $NiFe_2O_4$ loading.
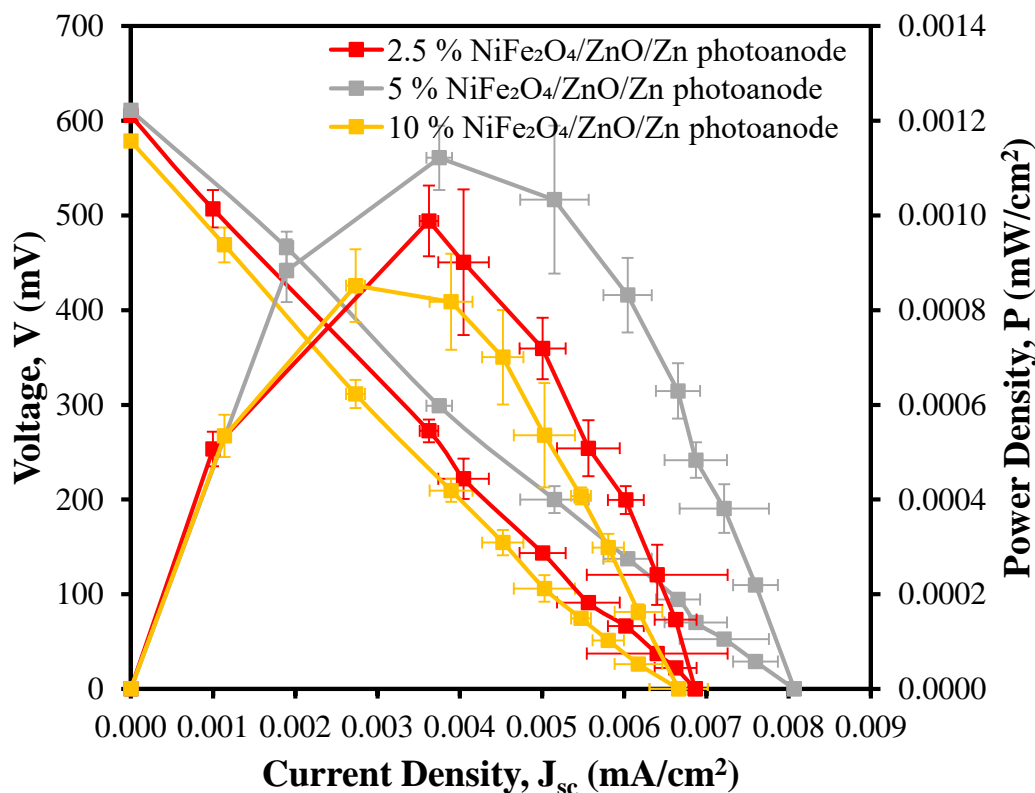
Figure 4.16: The Effect of NiFe₂O₄ Loading of NiFe₂O₄/ZnO/Zn Photoanode on Electricity Generation Efficiency by the PFC System ([RhB] = 5 mg/L; ZnO Loading = 0.5 g/L; Solution pH = 5.3).

The improvement of the PFC performance seen with increment of the NiFe₂O₄ loading from 2.5 % NiFe₂O₄/ZnO/Zn photoanode to 5 % NiFe₂O₄/ZnO/Zn photoanode validated that there was an increased number of active sites and surface area on the photoanode for adsorption of pollutant particles as well as light irradiation (Khalik et al., 2017; Lam et al., 2020a). The presence of high number of active sites of photocatalyst allowed the photoanode to be photoexcited easily, which then propelled the formation of •OH radicals to degrade the dye particles via oxidation of H_2O. These highly oxidative •OH radicals aid in achieving high colour removal efficiency and electricity generation. However, the performance of the photoanode deteriorated at higher NiFe₂O₄ loading (> 5 %). This could be explained by the presence of agglomeration of large amount of NiFe₂O₄ nanoparticles blocking the penetration and receiving of incoming light by the underlying photocatalyst, resulting in poor photocatalytic performance along with inefficient transferring of e_{CB}^- to stimulate electricity generation (Lam et al., 2020b; Zhang et al., 2021).

Figure 4.17 illustrates the UV-vis absorption spectra of RhB dye solution at different time intervals when exposed to photocatalysis using PFC system with 5 % $NiFe_2O_4/ZnO/Zn$ photoanode and under visible light irradiation. The maximum absorption peak was found at 553.4 nm, which was quite close to that reported by Kaviyarasu et al. (2019) and Zhang et al. (2017). The absorption peak of the RhB dye solution gradually decreased over reaction time, indicating the reduction of the dye particles concentration inside the solution due to the decomposition and destruction of their molecular structure (Chiu et al., 2019).
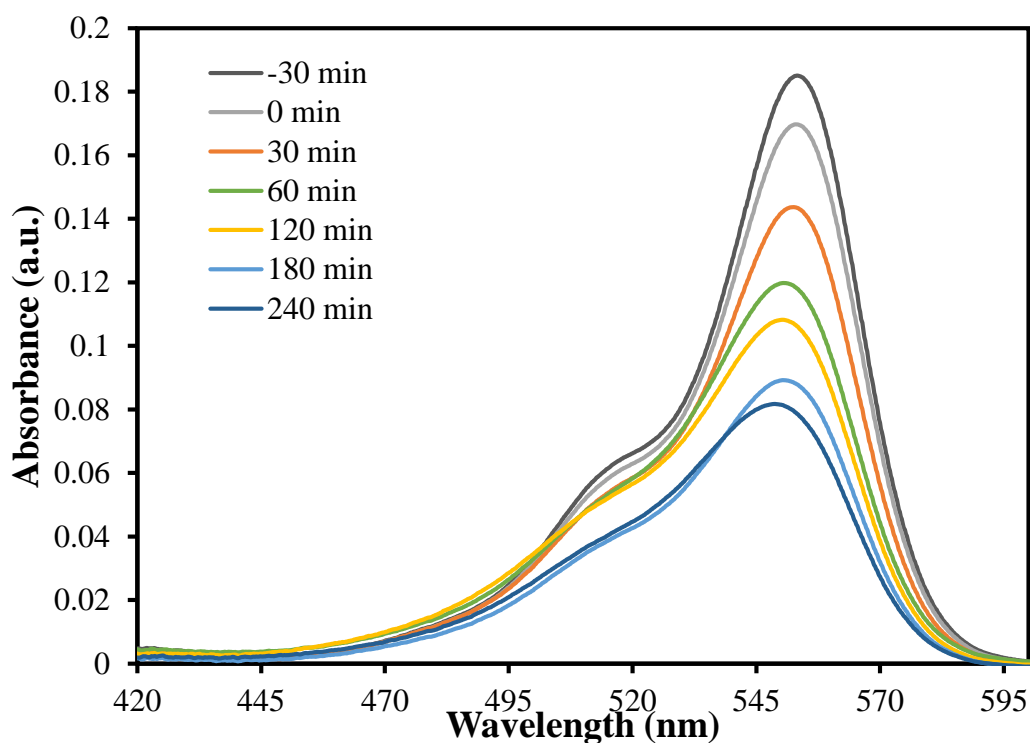
Figure 4.17: Declination of Absorption Spectra of RhB Dye Solution Over Time Using PFC System ([RhB] = 5 mg/L; ZnO Loading = 0.5 g/L; NiFe₂O₄ Loading = 5 %; Solution pH = 5.3).

The findings obtained from current study were in corroboration with that presented by other literature reports. Xia et al. (2018) verified that $SrTiO_3/BiOI$ composite photocatalyst with 30 wt% of $SrTiO_3$ achieved the highest photocatalytic degradation of crystal violet dye compared to 10 wt% $SrTiO_3/BiOI$, 20 wt% $SrTiO_3/BiOI$ and 40 wt% $SrTiO_3/BiOI$. In another separate study, Zhang et al. (2021) established that the photocatalytic ability of MoS_2/Bi_2WO_6 composite in treating RhB dye increased up to the point of 9 wt% MoS_2/Bi_2WO_6, beyond which the degrading

efficiency started to decline. The desirable photocatalytic performance of MoS_2/Bi_2WO_6 with 9 wt% MoS_2 could be due to the effective contact and absorbing of light by the photocatalysts. This enabled easy separation of e_{CB}^--h_{VB}^+ pair and promoted the production of radical species, which were responsible for the degradation of pollutants. Hence, in this study, $NiFe_2O_4/ZnO/Zn$ photoanode with 5 wt% of $NiFe_2O_4$ loading was selected as the optimum photoanode for the PFC system.

4.3 Effect of Process Parameters on PFC System

4.3.1 Effect of Supporting Electrolyte Concentration

The electrolyte concentration has a decisive influence on the performance of PFC system. In this study, Na_2SO_4 was chosen as the supporting electrolyte in view of its cost-effectiveness and ability to generate radicals which are capable of degrading the organic pollutants (Tan et al., 2019). Different concentrations of Na_2SO_4 were applied, specifically 0 M, 0.1 M, 0.2 M, 0.5 M and 1.0 M, with all other parameters remained unchanged.

Figure 4.18 demonstrates the performance of the PFC system in decolourising RhB dye solution in the absence of electrolyte and under various degrees of electrolyte concentration. From Figure 4.18, it was observed that the degradation efficiency of RhB dye solution by the PFC system was enhanced with the increment of Na_2SO_4 concentration from 0 M to 0.5 M. Nevertheless, the performance of the PFC system recorded a deterioration when Na_2SO_4 concentration was increased from 0.5 M to 1.0 M. The colour removal efficiency of RhB dye solution under 0 M, 0.1 M, 0.2 M, 0.5 M and 1.0 M were 55 %, 57 %, 59 %, 61 % and 57 %, respectively. This indicated that the presence of supporting electrolyte successfully improved the performance of the PFC system through reducing the internal resistance of the PFC system by enhancing the conductivity of the solution, eventually inducing smooth decoupling of e_{CB}^--h_{VB}^+ pair and generating more radicals (Ong et al., 2021).
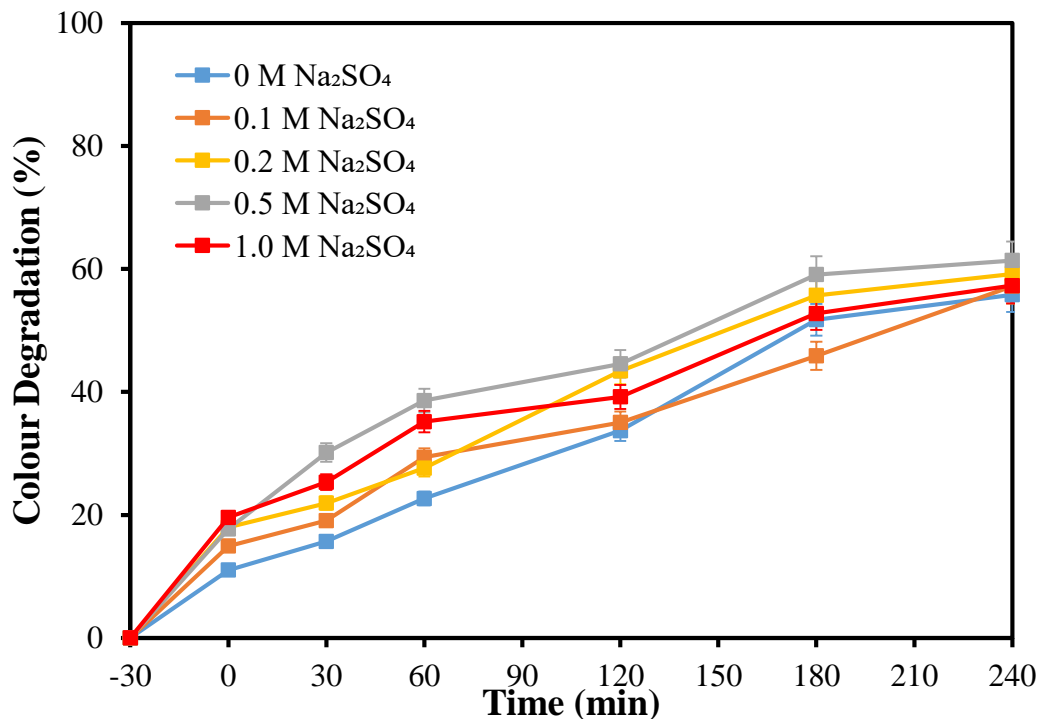
Figure 4.18: The Effect of Supporting Electrolyte Concentration on the Colour Removal Efficiency of RhB Dye Using PFC System ([RhB] = 5 mg/L; ZnO Loading = 0.5 g/L; NiFe$_2$O$_4$ Loading = 5 %; Solution pH = 5.3).

Figure 4.19 summarizes the impact of electrolyte concentration on the electricity generation efficiency of the PFC system. It was noteworthy that the electricity performance of the PFC system improved notably in the presence of electrolyte. The V_{oc} obtained for electrolyte concentrations of 0 M, 0.1 M, 0.2 M and 0.5 M were 611 mV, 625 mV, 633 mV and 634 mV, respectively. In addition, the J_{sc} achieved under electrolyte concentrations of 0 M, 0.1 M, 0.2 M and 0.5 M were 0.0081 mA/cm^2, 0.1088 mA/cm^2, 0.1219 mA/cm^2 and 0.1316 mA/cm^2. Besides that, the P_{max} attained in the event of 0 M, 0.1 M, 0.2 M and 0.5 M Na$_2$SO$_4$ concentrations were 0.0011 mW/cm^2, 0.0144 mW/cm^2, 0.0157 mW/cm^2 and 0.0168 mW/cm^2. Nonetheless, additional increase in the electrolyte concentration to 1.0 M was found to have negative effect on the electricity performance of the PFC system with V_{oc}, J_{sc}, and P_{max} dwindled to 626 mV, 0.1204 mA/cm^2 and 0.0151 mW/cm^2. The experimental data further confirmed that in terms of overall performance of the PFC system, 0.5 M was the optimum supporting electrolyte concentration among the varying levels of Na$_2$SO$_4$ concentrations.
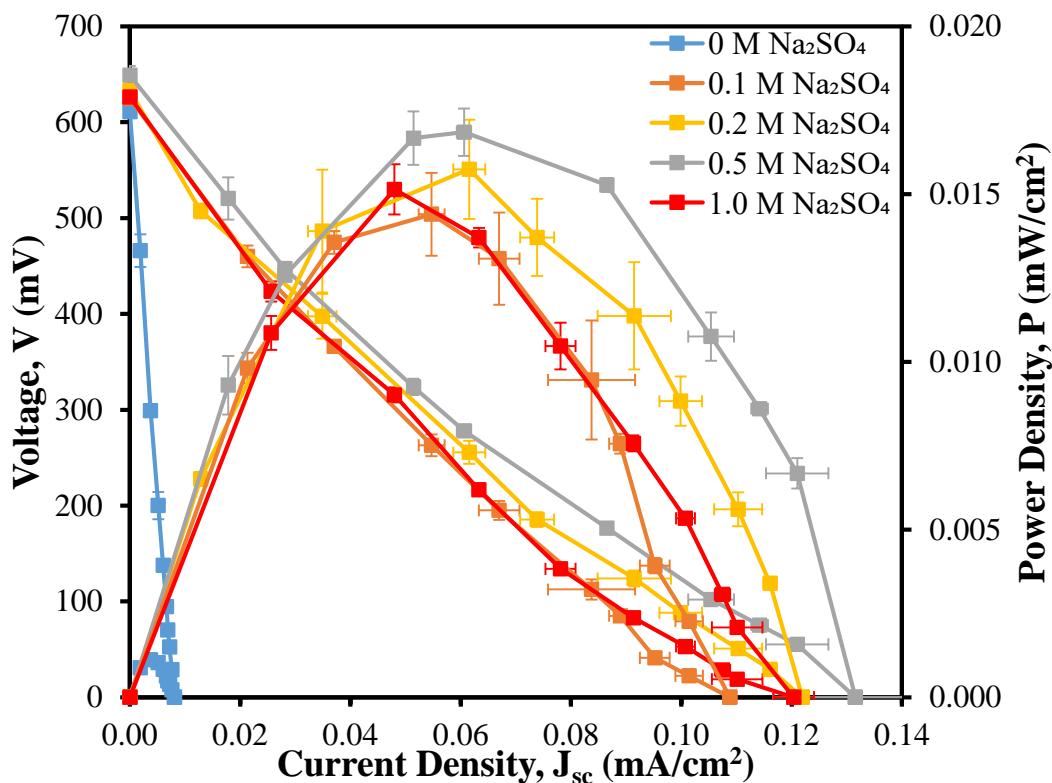
Figure 4.19: The Effect of Electrolyte Concentration on Electricity Generation Efficiency by the PFC System ([RhB] = 5 mg/L; ZnO Loading = 0.5 g/L; NiFe₂O₄ Loading = 5 %; Solution pH = 5.3).

The increase in colour removal efficiency and electricity performance as seen when using electrolyte with concentrations ranging from 0.1 M to 0.5 M could be on account of enhanced conductivity of the solution, which reduced the internal resistance of the PFC system (Liu et al., 2012). This promoted the detachment of e_{CB}^--h_{VB}^+ pairs, overcoming the undesired phenomenon of frequent combination between them. Moreover, the large potential bias created by the electrolyte propelled the unpaired e_{CB}^- to move from photoanode to cathode through an external circuit, thus generating higher amount of electricity (Wang et al., 2014). As a result, the free h^+ at the photoanode readily reacted with H_2O to produce •OH, whereas the e_{CB}^- transported to the aerated cathode reacted with O_2 to produce •O_2^- (Kee et al., 2018; Vasseghian et al., 2020). All these radicals contributed to higher colour degradation of RhB dye solution, consequently enhancing the electricity performance of the PFC system.

The usage of Na₂SO₄ as the supporting electrolyte could also be one of the reasons behind higher performance of the PFC system. As elucidated by Equations

(4.1) and (4.2), the SO_4^{2-} ions reacted with h_{VB}^+ to form $\bullet SO_4^-$, thus encouraging the separation of $e_{CB}^- \text{-} h_{VB}^+$ (Ong et al., 2020).

$$SO_4^{2-} + h_{VB}^+ \rightarrow \bullet SO_4^- \tag{4.1}$$

$$\bullet SO_4^- + H_2O \rightarrow SO_4^{2-} + \bullet OH + H^+ \tag{4.2}$$
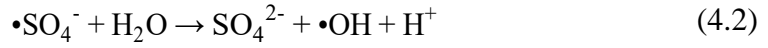
The generated $\bullet SO_4^-$ radicals are unexceptionally strong oxidants with high redox potential of +2.6 V, indirectly aiding in degrading the RhB dye particles and improving the performance of the PFC system (Wang, Jia and Wang, 2011). Equations (4.1) and (4.2) also reflect the recyclability of SO_4^{2-} ions and $\bullet SO_4^-$ radicals, ensuring high separation efficiency of $e_{CB}^- \text{-} h_{VB}^+$ as well as continuous supply of strong oxidative radicals to decompose the dye particles (Tan et al., 2019).

The depreciation in both photodegradation efficiency and electricity generation performance of the PFC system spotted when the electrolyte concentration was increased to 1.0 M could be ascribed to the presence of excess SO_4^{2-} ions, which blocked the movement of h_{VB}^+ and $\bullet SO_4^-$ radicals (Hu et al., 2003). This deduced that at high concentration of Na_2SO_4, the main element affecting the performance of the PFC system was the persistent recombination between $e_{CB}^- \text{-} h_{VB}^+$ in lieu of internal resistance of the system (Xu, Xu and Zheng, 2019). Hence, there was no improvement in the performance of the PFC system even though the Na_2SO_4 concentration was increased above 0.5 M.

The experimental data attained were in line with several previous studies. Xie and Ouyang (2017) stated that the electricity generation was the highest when Na_2SO_4 having a concentration of 0.2 M was used compared to that achieved by 0 M, 0.01 M, 0.05 M and 0.1 M. In another separate study done by Ong and his co-workers (2021), they mentioned that the optimum performance of the PFC system was attained when the Na_2SO_4 electrolyte concentration was enhanced from 0.05 M to 0.1 M, while electrolyte above 0.1 M displayed no profound effect on the PFC operation. Based on these reported literatures, it was found that different research works achieved different optimum Na_2SO_4 electrolyte concentrations. Therefore, Na_2SO_4 electrolyte of 0.5 M was selected as the optimum concentration and adopted in the subsequent study.

4.3.2 Effect of Initial Solution pH

Another pivotal factor affecting the performance of the PFC system is the initial solution pH since it is able to influence the surface charge properties of photoanode (Wang et al., 2013). The effect of pH on the photodegradation of RhB dye solution and electricity generation was investigated using pH ranging from 3 to 10, with all other parameters held unchanged. The measured natural pH of the RhB dye solution was 5.3 and adjustment of the dye solution pH was done using 1.0 M HCl solution and 1.0 M NaOH solution.

Figure 4.20 details the photocatalytic ability of the PFC system when treating RhB dye solution under various pH levels. The highest colour removal of 65 % was recorded at pH 10 (alkaline), followed by 61 % at pH 5.3 (natural), 45 % at pH 3 (acidic) and 35 % at pH 7 (neutral).
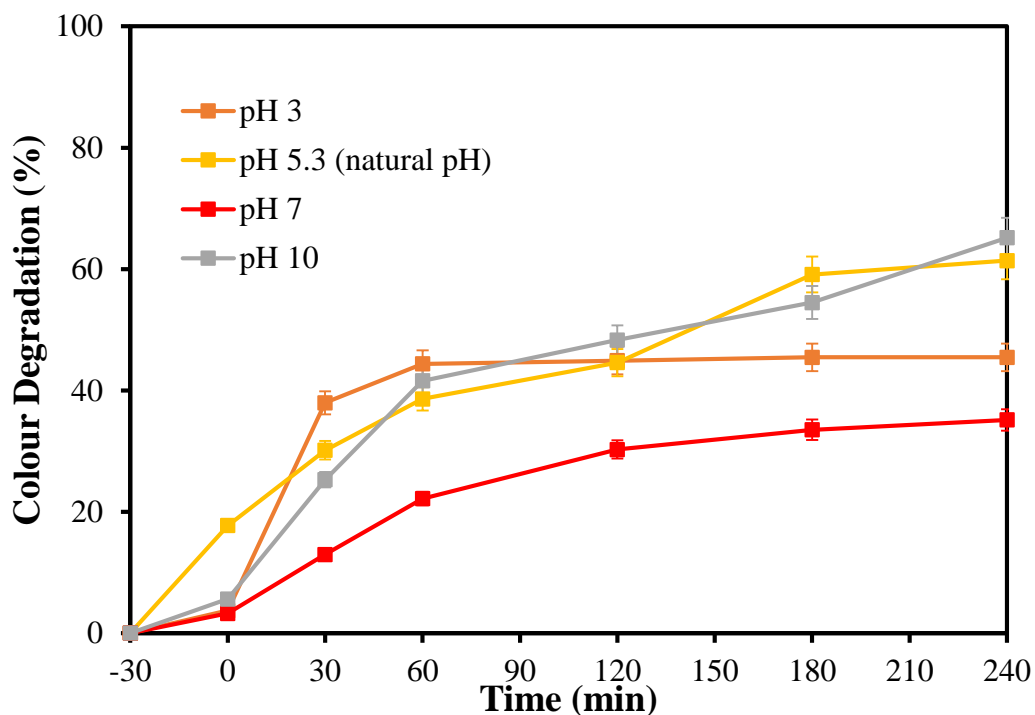
Figure 4.20: The Effect of pH on the Colour Removal Efficiency of RhB Dye Using PFC System ([RhB] = 5 mg/L; ZnO Loading = 0.5 g/L; NiFe$_2$O$_4$ Loading = 5 %; [Na$_2$SO$_4$] = 0.5 M).

Figure 4.21 shows the electricity generation performance of the PFC system

under different pH conditions. The highest electricity output was recorded at pH 3 (acidic), in which the V_{oc}, J_{sc}, and P_{max} were 649 mV, 0.3763 mA/cm^2 and 0.0531 mW/cm^2, respectively. On the other hand, when subjecting to pH 7 (neutral), the electricity performance of the PFC system was the weakest, where the V_{oc}, J_{sc}, and P_{max} yielded were 539 mV, 0.1163 mA/cm^2 and 0.0143 mW/cm^2. Besides that, the V_{oc}, J_{sc}, and P_{max} measured at pH 5.3 (natural) were 634 mV, 0.1316 mA/cm^2 and 0.0168 mW/cm^2, whereas that obtained under pH 10 (alkaline) were 637 mV, 0.1831 mA/cm^2 and 0.0253 mW/cm^2.
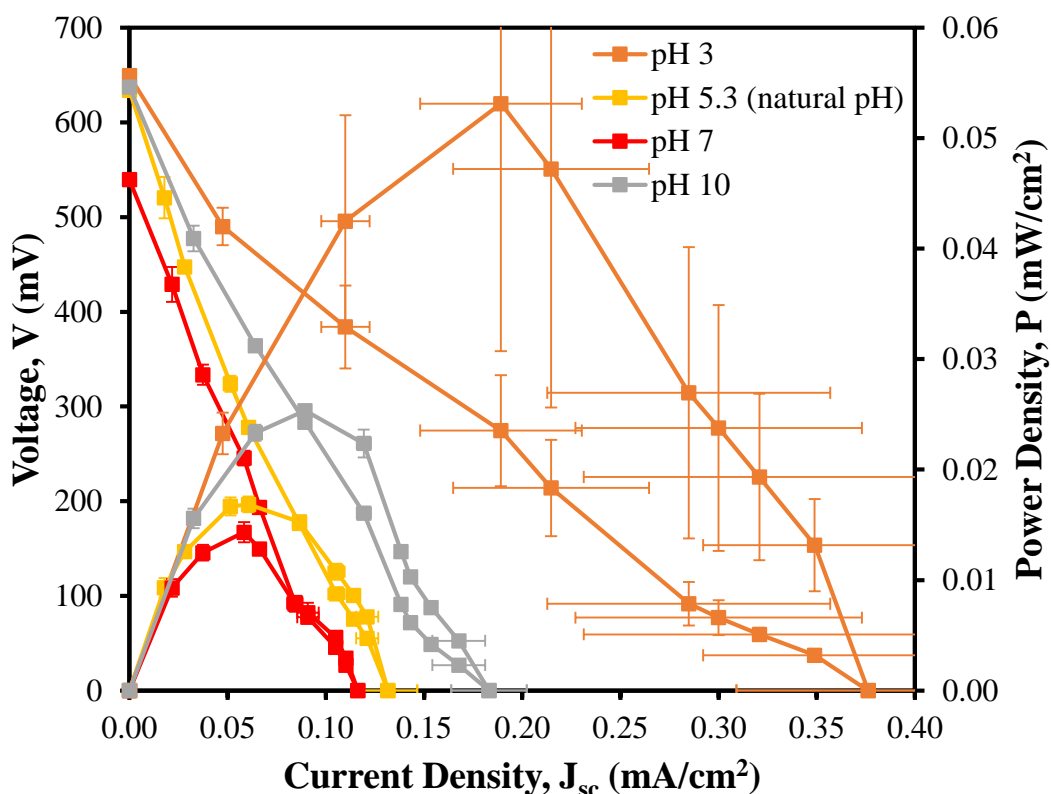
Figure 4.21: The Effect of pH on Electricity Generation Efficiency by the PFC System ([RhB] = 5 mg/L; ZnO Loading = 0.5 g/L; NiFe₂O₄ Loading = 5 %; [Na₂SO₄] = 0.5 M).

The varying photodegradation efficiency and electric yielding of the PFC system observed with alteration of pH levels could be explained using the concept of point of zero charge (pH$_{zpc}$) (Azeez et al., 2018). In simple terms, pH$_{zpc}$ is defined as the pH where an oxide will have zero surface charge. At pH levels below pH$_{zpc}$, the surface of the oxide will be positively-charged and vice-versa (Abbas, 2021). According to Abdollahi et al. (2012), the pH$_{zpc}$ for ZnO is pH 9, while Amulya et al.

(2020) reported that $NiFe_2O_4$ has a pH_{zpc} of pH 6. This justified the high colour removal of RhB dye solution and electricity production by the PFC system at pH 10. At pH 10, the surface of the 5 % $NiFe_2O_4/ZnO/Zn$ photoanode was negatively charged. Owing to the fact that RhB is a cationic dye, the presence of electrostatic attraction encouraged more RhB dye particles to adsorb onto the photoanode, leading to effective photodegradation of pollutants and favourable electricity production.

The remarkably high electricity generation by the PFC system observed at pH 3 could be due to the presence of H^+ ions from the addition of HCl (Kee et al., 2018). As a result, higher amount of H^+ ions participated in the oxygen reduction reaction at the oxygenated cathode, thus generating more electricity (Wang et al., 2014). Another possible justification was because of the derivation of anions, i.e. Cl^- from HCl, which was used as pH adjuster. Since at pH 3, the surface of the 5 % $NiFe_2O_4/ZnO/Zn$ photoanode was positively charged, the negatively-charged Cl^- ions were prompted to adsorb onto the photoanode surface and underwent reduction, eventually leading to enhanced electricity generation (Jiang et al., 2017). Although the PFC system achieved the highest electricity generation at pH 3, the colour removal efficiency was unsatisfactory. This could be due to the happening of frequent combination between $e_{CB}^- - h_{VB}^+$ as a result of insufficient OH^- ions to react with h_{VB}^+, causing low generation of •OH radicals to decolourise the RhB dye solution. One interesting finding from Figure 4.20 was that at pH 3, the photodegradation efficiency of the PFC system seemed to be stagnant after 60 minutes of irradiation time. This could be accredited to the dissolution of ZnO particles on the 5 % $NiFe_2O_4/ZnO/Zn$ photoanode by H^+ ions. The photocorrosion reaction of photoanode was shown by Equation (4.3) (Le et al., 2021).

$$ZnO + 2H^+ \rightarrow Zn^{2+} + H_2O \qquad (4.3)$$

From Figure 4.20, it was noted that the photodegradation efficiency of the PFC system attained at pH 5.3 was quite close to that achieved at pH 10. This was probably due to non-existence of pH adjuster either HCl or NaOH in the PFC system. The absence of HCl or NaOH prevented the dissociation of additional ions, which could compete with the RhB dye particles for adsorption surface provided by photoanode. At acidic pH, the Cl^- anions derived from HCl experienced a higher tendency than RhB

dye molecules to adsorb onto the photoanode having a positively-charged surface, thus lowering the photocatalytic activity (Phonsy et al., 2015). Conversely, at alkaline pH, Na^+ cations ionized from NaOH rivaled with cationic RhB dye molecules for the negatively-charged surface of photoanode, hence reducing the colour removal efficiency (Abdollahi et al., 2011; Lam, Quek and Sin, 2018). The lack of these undesirable competition led to higher chance of reaction between h_{VB}^+ and H_2O molecules, subsequently higher chance of •OH radicals formation as well as electricity production (Khalik et al., 2018). However, the superior photocatalytic performance and electricity generation amount at pH 10 than that under pH 5.3 indicated that strong electrostatic attraction force between the oppositely-charged photoanode surface and RhB dye molecules played a much crucial role in this research work.

On the other hand, the inferior electricity generation witnessed under pH 7 compared to all the other various pH levels could be attributed to the low degree of positive charge on the photoanode, which exerted insufficient attraction force on the OH^- ions. Instead, the OH^- ions interfered and decreased the rate of collision between h_{VB}^+ and H_2O molecules, impeding the formation of •OH radicals and greatly hampering the colour removal efficiency and electricity production by the PFC system (Khalik et al., 2018).

The findings obtained were in tally with past studies. El-Bindary, Ismail and Eladi (2019) reported that the highest photocatalytic degradation of reactive blue 21 using Ag/ZnO catalyst was obtained at alkaline pH 11. Another study conducted by Lee et al. (2017) revealed that the selection of optimal point for each predefined parameter was based on the overall performance of the PFC system with reference to photodegradation efficiency together with electricity generation performance, not solely based on any one of them. Hence, the alkaline pH 10 was designated as the optimum initial solution pH for the subsequent sections.

4.4   Radical Scavenging Test

It is acknowledged that active radical species contribute greatly to the photocatalytic mechanism of the PFC system. Therefore, radical trapping test was conducted, with silver nitrate, ethylenediaminetetraacetic acid disodium salt (EDTA-2Na), isopropanol and 1,4-benzoquinone (1,4-BQ) being selected to specifically quench e_{CB}^-, h_{VB}^+, •OH and •O$_2^-$, respectively. As displayed in Figure 4.22, the colour removal efficiency achieved by the PFC system deteriorated sharply after the addition of 1,4-BQ, i.e. from 65 % to 36 %, indicating •O$_2^-$ superiority in the photocatalytic degradation of RhB dye solution. On the contrary, h_{VB}^+ was the least dominant species since the colour removal rate attained decreased slightly from 65 % to 60 % after adding EDTA-2Na into the RhB dye solution. Moreover, the colour removal rates observed for the RhB dye solution after phototcatalytic reaction under the presence of silver nitrate and isopropanol were 42 % and 45 %, respectively. The results obtained in this study indicated that the main radical species affecting the photodegradation performance of the PFC system was •O$_2^-$, followed by e_{CB}^-, •OH and h_{VB}^+.
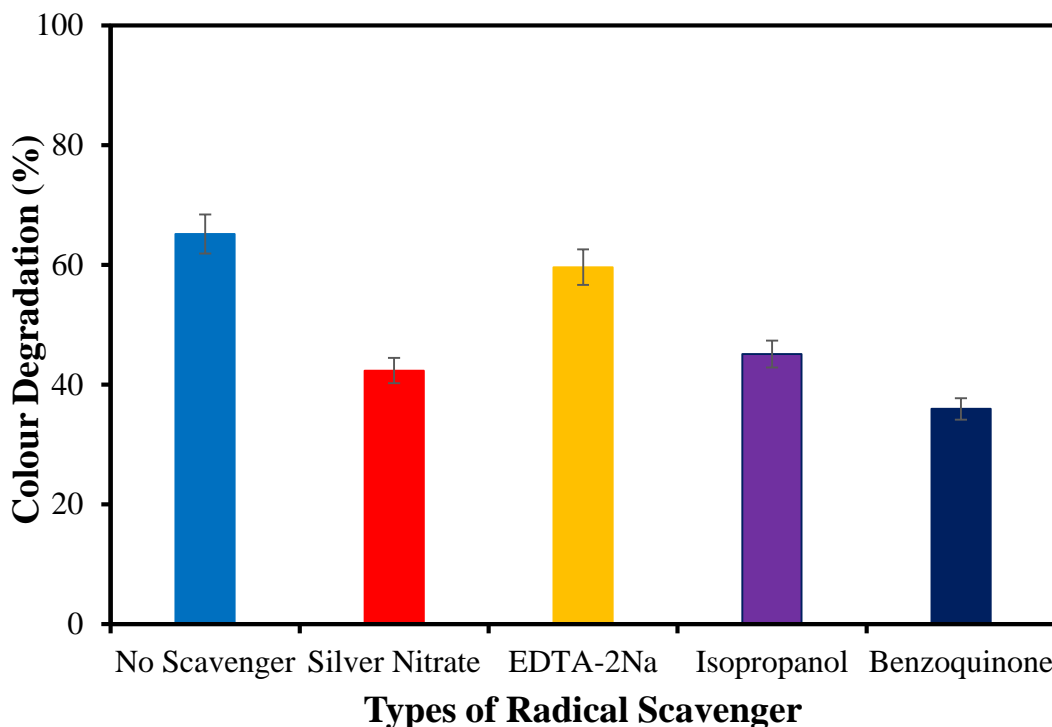
Figure 4.22: Colour Removal Efficiencies of RhB Dye Using PFC System After Addition of Various Radical Capturing Agents ([RhB] = 5 mg/L; ZnO Loading = 0.5 g/L; NiFe₂O₄ Loading = 5 %; [Na₂SO₄] = 0.5 M; Solution pH = 10; [Radical Trapping Agent] = 0.2 mM).

Based on the results obtained in the radical scavenging test as well as data obtained from UV-Vis DRS and Mott-Schottky analyses, the Z-scheme photocatalytic mechanism as shown in Figure 4.23 was proposed. When irradiated by incoming visible light, both ZnO and $NiFe_2O_4$ nanoparticles on the Zn plate experienced photoexcitation. This facilitated the excitation of their e^- from VB to CB with the h^+ left behind in each of their VB, thus forming $e_{CB}^- $-$h_{VB}^+$ pair. Due to the presence of an internal electric field, the detached e_{CB}^- in VB of ZnO readily transferred to the CB of $NiFe_2O_4$, subsequently recombined with the h_{VB}^+ present there (Wang et al., 2018). This scenario led to the occurrence of Z-scheme photocatalytic mechanism to photodegrade the RhB dye solution. Since the standard reduction potential of $O_2/\bullet O_2^-$ (- 0.33 eV) was less negative than the CB potential of $NiFe_2O_4$ (- 0.55 eV), the dissolved O_2 in the solution was easily reduced into $\bullet O_2^-$ by the e_{CB}^- in CB of $NiFe_2O_4$ (Liu et al., 2017). On the other hand, owing to the fact that the standard reduction potential of $H_2O/\bullet OH$ (2.4 eV) was less positive than the VB potential of ZnO (3.0 eV), the h_{VB}^+ in VB of ZnO promptly oxidized H_2O to generate $\bullet OH$ (Yang et al., 2016). The generation

of highly oxidative •O_2^- and •OH radicals aided in the degradation of RhB dye solution, simultaneously yielding electricity. In fact, Z-scheme photocatalytic mechanism provides numerous advantages compared to conventional photocatalytic mechanisms since it offers good segregation efficiency of e_{CB}^--h_{VB}^+, holds strong redox potential et cetera (Xu et al., 2018; Li et al., 2021b).
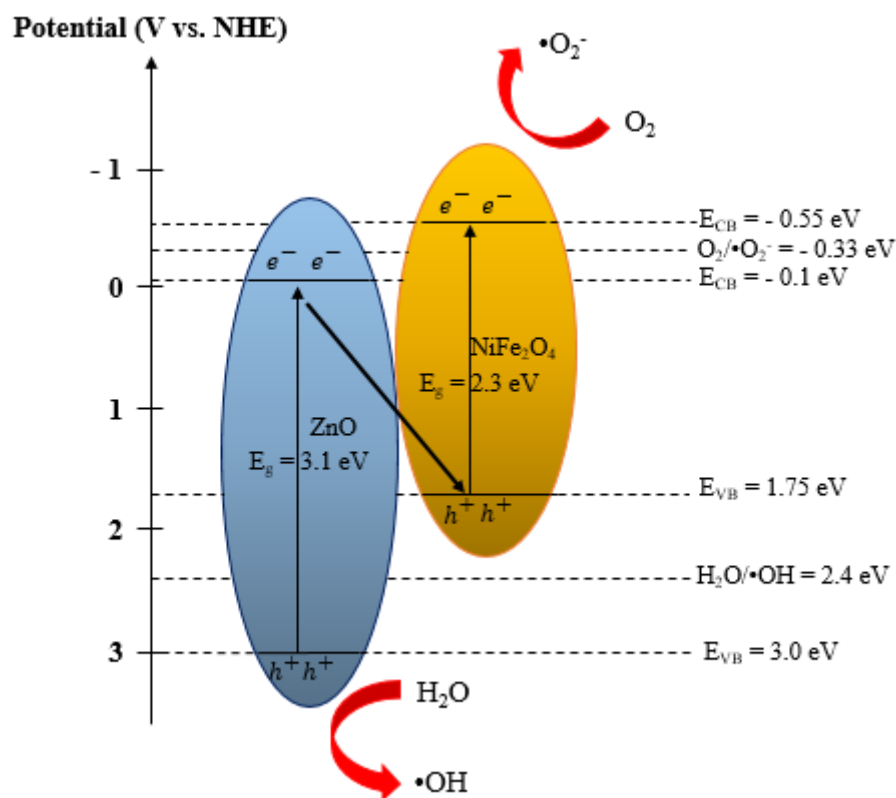
Figure 4.23: Schematic Diagram of Z-scheme Photocatalytic Mechanism of NiF$_e$O$_4$/ZnO/Zn Composite Photocatalyst.

The Z-scheme photocatalytic mechanism achieved in this research work was in accordance with past reported studies. Shi, Guo and Yuan (2017) reported the formation of an effective Z-scheme system using Ag$_3$PO$_4$/CuBi$_2$O$_4$/Ag, which helped to degrade tetracycline through formation of •O_2^- and •OH radicals. Moreover, Deng et al. (2019) stated that the coupling of WO$_3$ nanosheets with g-C$_3$N$_4$ nanosheets successfully degraded 78.6 % of RhB dye solution via an effective Z-scheme photocatalytic mechanism, which produced abundant amount of •O_2^- and •OH radicals to degrade the dye pollutants.

4.5   Mineralization Study

Aside from colour removal efficiency, another vital criterion for analyzing the performance of the PFC system in carrying out photocatalytic degradation of RhB dye solution is the attained mineralization rate of intermediate organic pollutants generated during the running of the experimental work. Consequently, mineralization study of RhB dye solution through COD analysis was performed using PFC system under optimum conditions determined earlier. Figure 4.24 compares the colour removal and COD degradation achieved by the PFC system within 240 minutes of irradiation time. As per Figure 4.24, the colour removal efficiency achieved was 65 %, higher than the 45 % obtained for COD degradation. This could be ascribed to formation of numerous small colourless intermediates caused by the photocatalytic degradation of RhB dye solution such as benzoic acid and butane-1,3-diol (Yu, 2009; Al-Kahtani, 2017). The presence of these intermediate products induced competition with the RhB dye molecules and constrained the supply of free active sites, subsequently lowering the COD removal rate (Chen and Lu, 2007). Unlike colour removal process which merely involved the cleavage of chromophore structure, the more comprehensive COD removal focused on the complete degradation of organics into harmless inorganic compounds such as CO_2 and H_2O, hence required longer reaction time to achieve complete mineralization (Mohammadzadeh et al., 2015; Pica et al., 2018; Sudha, Renu and Sangeeta, 2021).
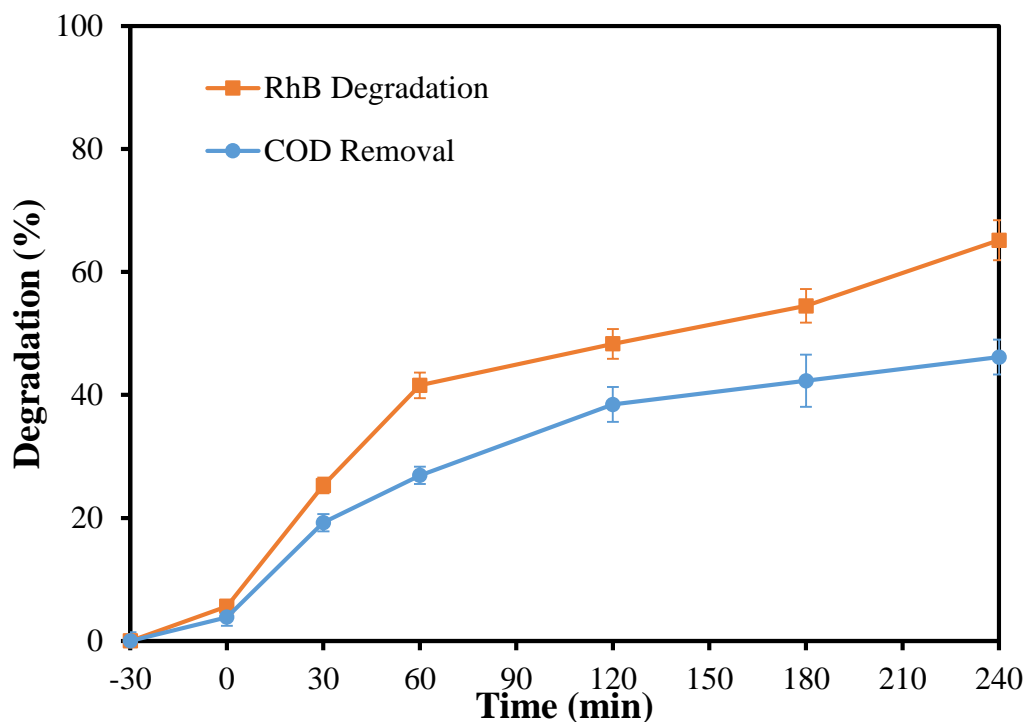
Figure 4.24: Comparison Between Colour Removal Efficiency of RhB Dye and COD Degradation Using PFC System ([RhB] = 5 mg/L; ZnO Loading = 0.5 g/L; NiFe$_2$O$_4$ Loading = 5 %; [Na$_2$SO$_4$] = 0.5 M; Solution pH = 10).

The findings obtained were congruent with previous studies. Biglar et al. (2021) revealed that mineralization process of Reactive Red 198 occurred at a much slower pace as opposed to decolourisation. The reason provided by them was that during the breaking down of azo bond -N=N- present in the dye molecular structure, colourless organic compounds were generated as well, indirectly increasing the amount of pollutants present although colour removal was achieved. In addition, Hadjltaief et al. (2016) reported lower COD removal rate than colour degradation efficiency when treating methyl green dye. In another separate study, 32 types of achromatic intermediates formed from photodecomposition of methyl green dye after exposed to 12 hours of irradiation by visible light were successfully identified by Mai et al. (2008). Due to the formation of persistent by-products from the photocatalytic degradation process, a longer reaction time would be required to accomplish complete mineralization.

4.6 Photoanode Recycling Test

One of the main factors determining the commercial potential and practical applications of the constructed PFC system is the capability of photoanode to maintain decent photocatalytic performance for long-term removal of organic pollutants. Therefore, the recyclability of the 5 % $NiFe_2O_4/ZnO/Zn$ photoanode was evaluated by conducting four continuous cycles of photocatalytic degradation of RhB dye solution using the PFC system. The experimental results in Figure 4.25 reflected that the photodegradation performance of the PFC system weakened with each cycle, dropping from 65 % in the first cycle to 50 % in the fourth cycle.
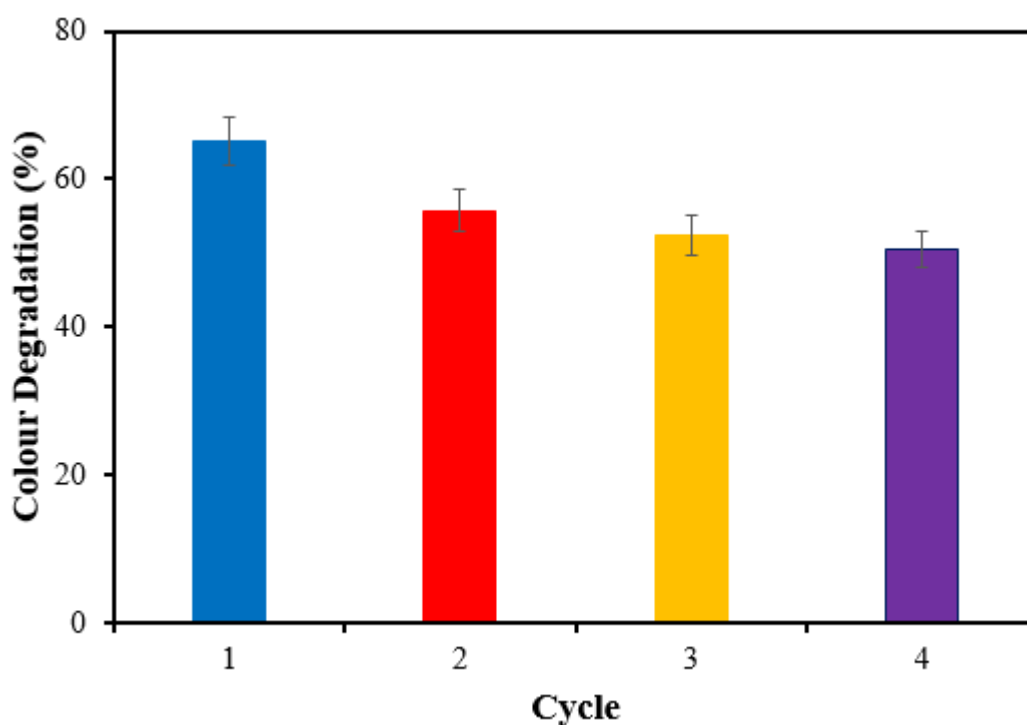
Figure 4.25: Colour Removal Efficiency of RhB Dye Using PFC System for Four Consecutive Cycles ([RhB] = 5 mg/L; ZnO Loading = 0.5 g/L; $NiFe_2O_4$ Loading = 5 %; [Na_2SO_4] = 0.5 M; Solution pH = 10).

The declination in colour degradation efficiency of RhB dye solution by the PFC system could be accredited to inevitable loss of $NiFe_2O_4/ZnO$ photocatalyst from the surface of photoanode. During the experiment, some of the photocatalyst forming a layer covering the photoanode might get detached and lost into the dye solution (Wang, Fei and Zhang, 2010; Arimi et al., 2016). Moreover, the loss of the

photocatalyst could be caused by the repetitive action of rinsing and drying the photoanode after each run (El-Bindary, Ismail and Eladi, 2019). The steady loss of photocatalyst reduced the amount of active sites available for photoexcitation, resulting in inefficient formation of e_{CB}^{-}-h_{VB}^{+}, which involved in generation of radical species. As a result, the performance of the PFC system depreciated with each repetition as fewer radical species were able to take part in the photocatalytic process.

The results obtained in this section clearly indicated that the film-type photoanode employed in the PFC system achieved a high stability, since it is still able to maintain adequate photocatalytic performance even after four successive cycles. This could be justified by the immobilization of the photocatalysts on film-type photoanode due to strong attachment onto the photoanode surface, which allowed ease in rinsing and retrieving the photocatalyst for recycling purpose as opposed to photocatalyst in powder form (Ghosh and Mondal, 2015; Marcello et al., 2020). Besides that, the present and past studies were unanimous in their findings. A research conducted by Barahimi, Moghimi and Taheri (2019) revealed that the photodegradation efficiency of Cu doped TiO_2/Bi_2O_3 in treating methyl orange solution under visible light irradiation declined from 74 % to 55 % after five cycles. In another study, Lu et al. (2021) confirmed the decent stability of $WO_3/BiOI$ in photocatalytic degradation of RhB dye solution under visible light irradiation, whereby the colour removal efficiency dropped from 98 % to 80 % after four cycles.

4.7   Photodegradation of Real Industrial Printing Ink Wastewater

The effectiveness of utilizing PFC system in treating synthetic dye solution had been proven by numerous past studies (Vasseghian et al., 2020). However, exiguous research is available on the applicability of PFC system to degrade various types of real wastewaters, specifically industrial printing ink wastewater. For this reason, the treatment of industrial printing ink wastewater using PFC system was assessed. The PFC system was operated under the sunlight and subjected to optimum conditions determined in the earlier parts of this research work. Typically, wastewater released

from printing industries is extremely complex because it contains different classes of dyes and various additives such as salts, resins along with other chemicals (Yaseen and Scholz, 2018; Liu, 2020). Table 4.1 presents the concentrations of BOD_5, COD and BOD_5/COD in addition to other important water quality parameters such as turbidity and pH measured before and after treatment period of 240 minutes.

Table 4.1: Characteristics of Real Industrial Printing Ink Wastewater Pre- and Post-Photocatalytic Degradation Using PFC System of 5 % $NiFe_2O_4$/ZnO/Zn Photoanode and CuO/Cu Cathode Under Sunlight (ZnO Loading = 0.5 g/L; $NiFe_2O_4$ Loading = 5 %; $[Na_2SO_4]$ = 0.5 M; Solution pH = 10; Sunlight Intensity = 907 × 100 lux; Irradiation Time = 240 minutes).

Parameter	Before Treatment	After Treatment	Efficiency (%)
BOD_5 (mg/L)	2730	1800	37.7
COD (mg/L)	68000	46000	32.4
BOD_5/COD	0.040	0.043	-
Turbidity (NTU)	115000	51900	54.9
pH	10.11	8.36	-

From the table, the measured initial concentrations of BOD_5, COD, BOD_5/COD and turbidity in addition to solution pH (before doing adjustment) for the real industrial printing ink wastewater were 2730 mg/L, 68000 mg/L, 0.040, 115000 NTU and 8.85, respectively. The determined BOD_5 from the industrial printing ink effluent could be pertained to the availability of biodegradable organic matter such as fats, oils and wax (Shindhal et al., 2020). In contrast, the obtained COD concentration affirmed the existence of chemical auxiliaries such as acids and alkalis, surfactants, pigments and resins (Holkar et al, 2016). Furthermore, the pH value of the industrial printing ink wastewater, which was 8.85 (alkaline) could possibly due to the higher usage of alkaline salts such as sodium hydroxide, sodium sulfate and sodium carbonate by the printing industry (Yaseen and Scholz, 2018). The computed biodegradability index or BOD_5/COD ratio prior to treatment was 0.040. According to Abdalla and Hammam (2014), wastewater having a BOD_5/COD ratio below 0.3 tend to resist biological treatment by inducing toxic effect on microorganisms and suppressing their growth. The notably low BOD_5/COD ratio obtained in this study inferred that there existed a significant proportion of biorefractory pollutants in the printing ink

wastewater, which contributed to its non-biodegradability. The characteristics of the industrial printing ink wastewater in this study were in consonance with other literature reports (Ding, Chen and Fan, 2011; Ghaly et al., 2014; Kehinde and Aziz, 2014). Hence, the constructed PFC system, which is an emerging technology with promising future could be applied to unselectively treat industrial printing ink wastewater and concomitantly produce power output.

4.7.1   Monitoring of Real Industrial Printing Ink Wastewater Photodegradation

The quality of the real industrial printing ink wastewater after photocatalytic treatment via the constructed PFC system under optimum conditions and 240 minutes of sunlight irradiation was reflected in Table 4.1. The BOD_5 and COD removal efficiencies achieved were 37.7 % and 32.4 %, respectively. It was obvious that the COD degradation rate of real industrial printing ink wastewater was lower than the 45 % achieved for RhB dye. This could be justified by the presence of various types of dyes, ions, trace elements and other contaminants in the printing ink wastewater, which led to intricate photocatalytic reaction and heavily disrupted the degradation process of the PFC system (Lam, Kee and Sin, 2018). Furthermore, the BOD_5/COD ratio increased from 0.040 to 0.043, signifying slight improvement in terms of biodegradability of the printing ink wastewater (Lam et al., 2021). In addition, the printing ink wastewater experienced a reduction of 54.9 % in turbidity. Moreover, the pH value of the printing ink wastewater improved from 10.11 to 8.36 after the treatment operation. This pH decrement could be due to the formation of organic acids such as lactic acid and acetic acid caused by the breaking of molecular structure of dyes by photocatalytic degradation (Mitrović et al., 2012).

As depicted in Figure 4.26, during the treatment of real industrial printing ink wastewater under sunlight irradiation, the PFC system recorded V_{oc}, J_{sc} and P_{max} values of 637 mV, 0.5119 mA/cm^2 and 0.0677 mW/cm^2, respectively. The electricity data of the PFC system in this case was apparently much better than that attained during the photocatalytic degradation of RhB dye solution using visible light. This could be attributed to the presence of large amount of dye and other organic particles inside the

printing ink wastewater in comparison to the solely RhB dye solution, which led to efficient separation of e_{CB}^{-}-h_{VB}^{+} as dye compounds reacted more readily with h_{VB}^{+} than H_2O molecules because they are strong reducing agent (Antoniadou and Lianos, 2010; Ying et al., 2016). As a result, more uncoupled e_{CB}^{-} flowed from the photoanode to cathode, causing the PFC system to yield higher power output. The higher COD removal efficiency achieved in the treatment of RhB dye solution could be due to the low concentration of dye used, i.e. 5 mg/L. Although this made it easier to attain a better COD degradation rate, it indirectly resulted in lower electric performance.
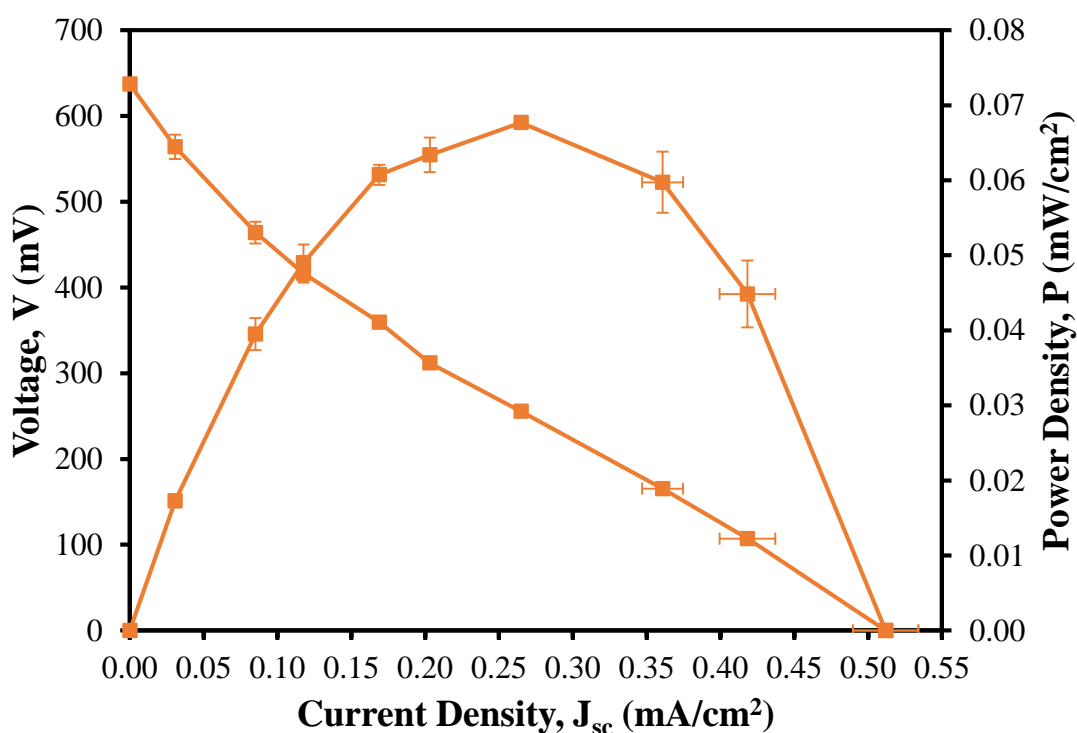
Figure 4.26: The Electricity Generation by PFC System When Treating Real Industrial Printing Ink Wastewater Under Sunlight (ZnO Loading = 0.5 g/L; NiFe₂O₄ Loading = 5 %; [Na₂SO₄] = 0.5 M; Solution pH = 10; Sunlight Intensity = 907 × 100 lux; Irradiation Time = 240 minutes).

4.8 Cost Estimation

Besides photocatalytic performance of the developed PFC system, economical aspect of it is also vital. Thus, the cost of preparing the photoanode and cathode was analyzed. The bill preparation is based on Tariff B (Low Voltage Commercial Tariff) as imposed by Tenaga Nasional Berhad. The total electricity cost needed for the fabrication of 5 % $NiFe_2O_4/ZnO/Zn$ photoanode and CuO/Cu cathode is summarized in Table 4.2, whereas Table 4.3 shows the total cost of materials expended during the synthesizing process. The electricity consumption was computed using Equation (4.4) suggested by Martínez, Ebenhack and Wagner (2019):

$$\text{Electricity Consumption (kWh)} = \frac{\text{Power (W)} \times \text{Operation Hour (h)}}{1000} \qquad (4.4)$$

Table 4.2: Total Electricity Consumption and Cost for Fabrication of Photoanode and Cathode.

Equipment	Power (W)	Duration (h)	Total Consumption (kWh)
i. Photoanode			
Ultrasonic Homogenizer	500	0.5	0.25
Tube Furnace	4500	3.5	15.75
Oven	1000	17	17
DC Power Supply	420	2	0.84
Magnetic Stirrer	650	3	1.95
		Sub Total	**35.79**
ii. Cathode			
Ultrasonic Homogenizer	500	0.5	0.25
Tube Furnace	4500	2	9
Oven	1000	24	24
		Sub Total	**33.25**
		Grand Total	**69.04**

Total Electricity Cost $\qquad$ = **69.04 kWh × RM 0.435 / kWh**

$\qquad\qquad\qquad\qquad\qquad$ = **RM 30.03**

Table 4.2: Total Material Cost for Synthesizing of Photoanode and Cathode.

Material	Quantity	Unit	Unit Price (RM)	Price (RM)
i. Photoanode				
Zn Foil	20	cm^2	0.76	15.20
$Zn(CH_3COO)_2 \cdot 2H_2O$	0.22	g	0.08	0.02
$Zn(NO_3)_2 \cdot 4H_2O$	0.16	g	0.15	0.02
$Ni(NiO_3)_2 \cdot 6H_2O$	0.29	g	0.26	0.08
$Fe(NO_3)_3 \cdot 9H_2O$	0.81	g	0.15	0.13
NaOH	0.82	g	0.03	0.03
C_2H_5OH	0.010	L	12.00	0.12
			Sub Total	**15.60**
ii. Cathode				
Cu Foil	15	cm^2	0.14	2.10
$Na_2S_2O_8$	2	g	0.06	0.12
NaOH	8	g	0.03	0.24
C_2H_5OH	0.010	L	12.00	0.12
			Sub Total	**2.58**
			Grand Total	**18.18**

Total Production Cost $\qquad$ = **Total Electricity Cost + Total Material Cost**

$\qquad\qquad\qquad\qquad\qquad$ = **RM 30.03 + RM 18.18**

$\qquad\qquad\qquad\qquad\qquad$ = **RM 48.21**

The total production cost for the photoanode and cathode of the constructed PFC system was RM 48.21. From this amount, approximately 63 % was accredited to the usage of electricity during the fabrication process of photoanode and cathode. Nevertheless, PFC system has a bright prospect to be applied extensively as an alternative green method to treat dyestuff wastewater and concurrently retrieving electricity. In addition, the photoanode demonstrated high ability to be recycled and

reused for continuous cycles of photocalytic activity without losing its photoreactivity. This recyclable property exhibited by the photoanode could reduce the treatment cost of PFC system and further suggests the commercialization possibility of the PFC system.

CHAPTER 5

CONCLUSION AND RECOMMENDATIONS

5.1   Conclusion

In current study, a PFC system having $NiFe_2O_4/ZnO/Zn$ photoanode and CuO/Cu cathode was successfully developed for treating dyestuff wastewater and synchronously inducing electricity generation under visible light irradiation. The fabricated photoelectrodes were characterized via analyses such as FESEM, EDX, FTIR, XRD, UV-Vis DRS, TPR, LSV, EIS and MS. Through FESEM analysis, the morphology of ZnO was demonstrated as tree-shaped with particle sizes varying from 310 nm to 5930 nm, while $NiFe_2O_4$ appeared in granular form having particle sizes ranging from 64 nm to 239 nm. The CuO on the surface of Cu cathode occurred in rod shapes with size differing from 91 nm to 392 nm. The elemental composition in both photoelectrodes were determined using EDX analysis. The results revealed that the photoanode consisted of Ni, Fe, Zn and O elements, whereas the cathode constituted of Cu and O elements, verifying their high level of purity. FTIR analysis disclosed the presence of Zn-O bonds and ionic vibrations of $NiFe_2O_4$ nanoparticles as well as O-H groups from water molecules, assuring the presence of $NiFe_2O_4/ZnO$ hybrid photocatalyst on the Zn plate and generation of highly oxidative •OH radicals. Through FTIR analysis, the presence of Cu-O bonds and O-H groups were identified, indicating the presence of CuO on the cathode surface. In addition, the XRD analysis successfully verified the phase purity of $NiFe_2O_4/ZnO/Zn$ photoanode and CuO/Cu cathode

through detection of the corresponding diffraction peaks. Furthermore, UV-Vis DRS test proved that the hybrid formed by coupling $NiFe_2O_4$ with ZnO successfully reduced the wide band gap of ZnO, i.e. from 3.1 eV to 1.9 eV, enabling easier separation of $e_{CB}^- - h_{VB}^+$. The results obtained from TPR and LSV justified that $NiFe_2O_4$/ZnO composite achieved higher photocurrent density than pure ZnO, signaling the realization of enhanced photoresponse. Moreover, EIS analysis showed that the charge transfer resistance was well improved after forming $NiFe_2O_4$/ZnO hybrid, which prevented the frequent recombination of $e_{CB}^- - h_{VB}^+$, thus elevating the photocatalytic activity and producing more electricity. The outcomes of MS analysis showed that the conduction band (CB) potential of ZnO and $NiFe_2O_4$ were - 0.10 eV and - 0.55 eV, respectively. The computed valence band (VB) potential of ZnO and $NiFe_2O_4$ were 3.0 eV and 1.75 eV, respectively.

The results of preliminary studies unveiled that PFC system using $NiFe_2O_4$/ZnO/Zn photoanode and CuO/Cu cathode manifested highest RhB colour removal efficiency and electricity yield compared to photolysis and PFC system using ZnO/Zn photoanode when subjected to visible light irradiation. This showed that the forming of hybrid $NiFe_2O_4$/ZnO/Zn photoanode had alleviated the problem of easy recombination of $e_{CB}^- - h_{VB}^+$, thus improving the photocatalytic performance of the PFC system. On the other hand, PFC system operated under closed circuit condition exhibited better RhB colour removal efficiency and electricity output compared to PFC functioning with an open circuit. This was due to the presence of external circuit, which facilitated the shifting of e_{CB}^- from photoanode to cathode, subsequently promoting the separation of $e_{CB}^- - h_{VB}^+$ and cause better photocatalytic performance.

Furthermore, the effect of numerous process parameters on the photocatalytic performance of the PFC system in the context of RhB dye colour removal efficiency and electricity generation were studied, specifically $NiFe_2O_4$ loading, electrolyte concentration and initial solution pH. The results obtained implied that the PFC system performed the best under optimum operating conditions of 5 % $NiFe_2O_4$/ZnO/Zn photoanode, 0.5 M Na_2SO_4 supporting electrolyte and alkaline condition of pH 10. Under these optimum settings, the PFC system attained colour removal efficiency of 65 %, while in terms of electricity generation, it achieved V_{oc}, J_{sc}, and P_{max} of 637 mV,

0.1831 mA/cm^2 and 0.0253 mW/cm^2, respectively.

Consecutively, radical scavenging test was conducted and the main radical species identified were $\bullet O_2^-$ and $\bullet OH$. Thus, a Z-scheme photocatalytic mechanism was proposed to explain the photodegradation process of the PFC system. This was followed by mineralization study of RhB dye solution using the constructed PFC system. The achieved COD degradation rate was much lower relative to RhB colour removal efficiency, suggesting longer time might be crucial to achieve total mineralization. The stability and reusability of the fabricated NiFe$_2$O$_4$/ZnO/Zn photoanode was further assessed through recycling test. The colour removal efficiency of the RhB dye solution declined with each repetition, whereby it deteriorated from 65 % to 50 % after four continuous cycles. This could be credited to the unescapable loss of photocatalyst. Ultimately, the active sites available for photoexcitation were significantly reduced, resulted in inefficient formation of e_{CB}^--h_{VB}^+ and directly retarded the generation of free radicals.

Moreover, the performance of the PFC system in treating real industrial printing ink wastewater was evaluated under sunlight. The BOD$_5$, COD and turbidity removal efficiencies achieved were 37.7 %, 32.4 % and 54.9 %. Besides that, the electricity output attained by the PFC system in terms of V_{oc}, J_{sc} and P_{max} values were 637 mV, 0.5119 mA/cm^2 and 0.0677 mW/cm^2, respectively. The higher electricity performance could be ascribed to the presence of abundant amount of dye particles, which acted as good reducing agent that easily reacted with h_{VB}^+, thus promoting the detachment of e_{CB}^--h_{VB}^+ and producing large amount of electricity. On the other hand, the unsatisfactory COD removal rate compared to RhB dye solution could be supported by the fact that the RhB dye solution concentration used was much lower, which allowed easy achievement of high COD degradation rate on the expense of inferior electricity performance.

Lastly, cost analysis was conducted for the fabrication of NiFe$_2$O$_4$/ZnO/Zn photoanode and CuO/Cu cathode. The total production cost calculated was RM 48.21. In summary, PFC system is an emerging approach with bright future and large potential to be further untapped for dyestuff wastewater treatment and simultaneous

electricity generation.

5.2   Recommendations

Upon completion of current study, the following fundamental aspects were determined and should be taken into consideration in the future PFC studies:

1. The influence of other process parameters that were not analysed in current study, namely initial concentration of pollutants, light intensity, air flow rate, initial solution temperature and so forth should be evaluated to further enhance the photodegradation efficiency and electricity generation of the PFC system.

2. The base film of the photoanode, i.e. the Zn plate is suggested to be replaced with fluorine-doped tin oxide (FTO) glass since it is transparent, which could allow the light irradiation to activate the photocatalysts on both the front and back sides, leading to improvement in the performance of the PFC system.

3. HPLC and GC tests could be employed to determine the photodegradation mechanism of the PFC system through identification of the intermediate chemicals generated from the photocatalytic reaction.

REFERENCES

Abbas, M., 2021. Factors influencing the adsorption and photocatalysis of direct red 80 in the presence of a TiO$_2$: equilibrium and kinetic modelling. *Journal of Chemical Research*, pp. 694-701.

Abdalla, K. Z. and Hammam, G., 2014. Correlation between biological oxygen demand and chemical oxygen demand for various wastewater treatment plants in Egypt to obtain the biodegradability indices. *International Journal of Sciences: Basic, and Applied Research (IJSBAR)*, 13, pp. 42-48.

Abdollahi, Y., Abdullah, A. H., Zainal, Z. and Yusof, N. A., 2012. Photocatalytic degradation of p-cresol by zinc oxide under UV irradiation. *International Journal of Molecular Sciences*, 13, pp. 302-315.

Adeleke, J. T., Theivasanthi, M., Thiruppathi, M., Swaminathan, M., Akomolafe, T. and Alabi, A. B., 2018. Photocatalytic degradation of methylene blue by ZnO/NiFe$_2$O$_4$ nanoparticles. *Applied Surface Science*, 455, pp. 195-200.

Ahmad, A., Mohd-Setapar, S. H., Chuong, C. S., Khatoon, A., Wani, W. A., Kumar, R. and Rafatullah, M., 2015. Recent advances in new generation dye removal technologies: novel search for approaches to reprocess wastewater. *RSC Advances*, 5, pp. 30801-30818.

Al-Kahtani, A. A., 2017. Photocatalytic degradation of rhodamine B dye in wastewater using gelatin/CuS/PVA under solar light irradiation. *Journal of Biomaterials and Nanobiotechnology*, 8, pp. 66-82.

Amulya, M. A. S., Nagaswarupa, H. P., Kumar, M. R. A., Ravikumar, C. R.,

Prashantha, S. C. and Kusuma, K. B., 2020. Sonochemical synthesis of $NiFe_2O_4$ nanoparticles: characterization and their photocatalytic and electrochemical applications. *Applied Surface Science Advances*, 1, pp. 1-10.

Andronic, L., Isac, L., Cazan, C. and Enesca, A., 2020. Simultaneous adsorption and photocatalysis processes based on ternary TiO_2-Cu_xS-fly ash hetero-structures. *Applied Sciences*, 10, pp. 1-16.

Antoniadou, M. and Lianos, P., 2010. Production of electricity by photoelectrochemical oxidation of ethanol in a PhotoFuelCell. *Applied Catalysis B: Environmental*, 99, pp. 307-313.

Antoniadou, M. and Lianos, P., 2014. Photo-fuel-cells: an alternative route for solar energy conversion. In: B. Viswanathan, V. R. Subramaniam and J. S. Lee, ed. 2014. *Materials and Processes for Solar Fuel Production*. New York: Springer. pp. 135-153.

Arimi, A., Farhadian, M., Nazar, A. R. S. and Homayoonfal, M., 2016. Assessment of operating parameters for photocatalytic degradation of a textile dye by Fe_2O_3/TiO_2/clinoptilolite nanocatalyst using Taguchi experimental design. *Research on Chemical Intermediates*, 42, pp. 4021-4040.

Arulmathi, P., Jeyaprabha, C., Sivasankar, P. and Rajikumar, V., 2019. Treatments of textile wastewater by coagulation-flocculation process using *Gossypium herbaceum* and polyaniline coagulants. *CLEAN – Soil, Air, Water*, 47, pp. 1-10.

Asha, K., Satsangi, V. R., Shrivastav, R., Kant, R., Dass, S., 2020. Effect of morphology and impact of the electrode/electrolyte interface on the PEC response of Fe_2O_3 based systems – comparison of two preparation techniques. *Royal Science of Chemistry*, 10, pp. 42256-42266.

Aydemir, C., Yenidoğan, S., Karademir, A. and Kandirmaz, E. A., 2017. The examination of vegetable- and mineral oil-based inks' effects on print quality: green printing effects with different oils. *Journal of Applied Biomaterials and Functional Materials*, 16, pp. 137-143.

Ayele, A., Getachew, D., Kamaraj, M. and Suresh, A., 2021. Phycoremediaton of synthetic dyes: an effective and eco-friendly algal technology for the dye abatement. *Journal of Chemistry*, 6, pp. 1-14.

Azeez, F., Al-Hetlani, E., Arafa, M., Abdelmonem, Y., Nazeer, A. A., Amin, M. O. and Madkour, M., 2018. The effect of surface charge on photocatalytic degradation of methylene blue dye using chargeable titania nanoparticles. *Scientific Reports*, 8, pp. 1-9.

Bai, J., Wang, R., Li, Y., Tang, Y., Zeng, Q., Xia, L., Li, X., Li, J., Li, C. and Zhou, B., 2016. A solar light driven dual photoelectrode photocatalytic fuel cell (PFC) for simultaneous wastewater treatment and electricity generation. *Journal of Hazardous Materials*, 311, pp. 51-62.

Banerjee, S., Dubey, S., Gautum, R. K., Chattopadhyaya, M. C. and Sharma, Y. C., 2019. Adsorption characteristics of alumina nanoparticles for the removal of hazardous dye, Orange G from aqueous solutions. *Arabian Journal of Chemistry*, 12, pp. 5339-5354.

Bankole, P. O., Adekunle, A. A. and Govindwar, S. P., 2018. Enhanced decolourisation of acid red 88 dye by newly isolated fungus, *Achaetomium strumarium. Journal of Environmental Chemical Engineering*, 6, pp. 1589-1600.

Barahimi, V., Moghimi, H. and Taheri, R. A., 2019. Arafa, M., Abdelmonem, Y., Nazeer, A. A., Amin, M. O. and Madkour, M., 2018. Cu doped TiO_2-Bi_2O_3 nanocomposite for degradation of azo dye in aqueous solution: process modelling and optimization using central composite design. *Journal of Environmental Chemical Engineering*, 7, pp. 1-8.

Benkhaya, S., M'rabet, S. and El Harfi, A., 2020. Classifications, properties, recent synthesis and applications of azo dyes. *Heliyon*, 6, pp. 1-26.

Bhosale, R., Jain, S., Vinod, C. P., Kumar, S. and Ogale, S., 2019. Direct Z-scheme g-C_3N_4/Fe_2WO_4 nanocomposite for enhanced and selective photocatalytic CO_2 reduction under visible light. *ACS Applied Materials and Interfaces*, 11, pp. 6174-6183.

Biglar, F., Talaiekhozani, A., Aminsharei, F., Park, J. B., Barghi, A. and Rezania, S., 2021. Application of ZnO-Nd nano-photocatalyst for the reactive red 198 dye decolourisation in the falling-film photocatalytic reactor. *Toxics*, 9.

Bilińska,, L., Gmurek, M. and Ledakowicz, S., 2017. Textile wastewater treatment by AOPs for brine reuse. *Process Safety and Environmental Protection*, 109, pp. 420-428.

Boretti, A. and Rosa, L., 2019. Reassessing the projections of the world water development report. *NPJ Clean Water*, 2, pp. 1-6.

Chankhanittha, T. and Nanan, S., 2021. Visible light-driven photocatalytic degradation of ofloxacin (OFL) antibiotic and Rhodamine B (RhB) dye by solvothermally grown ZnO/Bi_2MoO_6 heterojunction. *Journal of Colloid and Interface Science*, 582, pp. 412-427.

Chankhanittha, T., Somaudon, V., Photiwat, T., Youngme, S., Hemavibool, K. and Nanan, S., 2021. Enhanced photocatalytic performance of ZnO/Bi_2WO_6 heterjunctions toward photocatalytic degradation of fluoroquinolone-based antibiotics in wastewater. *Journal of Physics and Chemistry of Solids*, 153, pp. 1-20.

Chellam, S. and Sari, M. A., 2016. Aluminium electrocoagulation as pretreatment during microfiltration of surface water containing NOM: a review of fouling, NOM, DBP and virus control. *Journal of Hazardous Materials*, 304, pp. 490-501.

Chen, C. C. and Lu, C. S., 2017. Mechanistic studies of the photocatalytic degradation of methyl green: an investigation of products of the decomposition processes. *Environmental Science Technology*, 41, pp. 4389-4396.

Chiu, Y. H., Chang, M. T. F., Chen, C. Y., Sone, M. and Hsu, Y. J., 2019. Mechanical insights into photodegradation of organic dyes using heterostructure photocatalysts. *Catalysts*, 9, pp. 430-461.

Collivignarelli, M. C., Abbà, A., Miino, M. C. and Damiani, S., 2019. Treatments for colour removal from wastewater: state of the art. *Journal of Environmental*

Management, 236, pp. 727-745.

Da S. Pereira, W., Gozzo, C. B., Longo, E., Leite, E. R. and Sczancoski, J. C., 2019. Investigation on the photocatalytic performance of $Ag_4P_2O_7$ microcrystals for the degradation of organic pollutants. *Applied Surface Science*, 493, pp. 1195-1204.

Dahamsheh, A. and Wedyan, M., 2017. Evaluation and assessment of performance of Al-Hussein bin Talal University (AHU) wastewater treatment plants. *International Journal of Advanced and Applied Sciences*, 4, pp. 84-89.

Dayi, B., Kyzy, A. D. and Akdogan, H. A., 2019. Characterization of recuperating talent of white-rot fungi cells to dye-contaminated soil/water. *Chinese Journal of Chemical Engineering*, 27, pp. 634-638.

De Roos, A. J., Gurian, P. L., Robinson, L. F., Rai, A., Zakeri, I. and Kondo, M. C., 2017. Review of epidemiological studies of drinking-water turbidity in relation to acute gastrointestinal illness. *Environmental Health Perspectives*, 125.

Deaconu, M., Senin, R., Stoica, R., Athanasiu, A., Crudu, M., Oproiu, L., Ruse, M. and Filipescu C., 2016. Adsorption decolourisation technique of textile/leather – dye containing effluents. *International Journal of Waste Resources*, 6, pp. 1-7.

Deng, S. L., Yang, Z. B., Lv, G. J., Zhu, Y. Q., Li, H. C., Wang, F. M. and Zhang, X. B., 2019. WO_3 nanosheets/g-C_3N_4 nanosheets' nanocomposite as an effective photocatalyst for degradation of rhodamine B. *Applied Catalysis A*, 125, pp. 44-55.

Dewata, I. and Zainul, R., 2015. Determination of pH-BOD-COD and degradation in Batang Arau watersheds at Padang city. *Journal of Chemical and Pharmaceutical Research*, 49, pp. 445-451.

Ding, L., Chen, Y. and Fan, J., 2011. An overview of the treatment of print ink wastewaters. *Journal of Environmental Chemistry and Ecotoxicology*, 3, pp. 272-276.

Duta, L., Serban, N., Oktar, F. N. and Mihailecsu, I. N., 2013. Biological hydroxyapatite thin films synthesized by pulsed laser deposition *Optoelectronics and Advanced Materials*, 7, pp. 1040-1044.

El-Bindary, A. A., Ismail, A. and Eladi, E. F., 2019. Photocatalytic degradation of reactive blue 21 using Ag doped ZnO nanoparticles. *Journal of Materials and Environmental Science*, 10, pp. 1258-1271.

Fu, S., Deng, B., Ma, D., Cheng, H. and Dong, S., 2018. Visible-light-driven photocatalytic fuel cell with an Ag-TiO$_2$ carbon foam anode for simultaneous 4-chlorophenol degradation and energy recovery. *ChemEngineering*, 2, pp. 20-29.

Galeono, L. A., Guerrero-Flórez, M., Sánchez, C. A., Gil, A., and Vicente, M. Á., 2019. Disinfection by chemical oxidation methods. In: A. Gil, L. A., Galeono and M. Á Vicente, ed. 2019. *Applications of advanced oxidation processes (AOPs) in drinking water treatment.* Cham: Springer. pp. 257-296.

Gao, Y., Yang, B. and Wang, Q., 2018. Biodegradation and decolourisation of dye wastewater: a review. *IOP Conference Series: Earth and Environmental Science*, 178, pp. 1-5.

Gawande, M. B., Goswami, A., Felpin, F. X., Asefa, T., Huang, X., Silva, R., Zou, X., Zboril, R. and Varma, R. S., 2016. Cu and Cu-based nanoparticles: synthesis and applications in catalysis. *Chemical Reviews*, 116, pp. 3722-3811.

Ghaly, A. E., Ananthashankar, R., Alhattab, M. and Ramakrishnan, V. V., 2014. Production, characterization and treatment of textile effluents: a critical review. *Journal of Chemical Engineering and Process Technology*, 5, pp. 1-18.

Ghosh, A. and Mondal, A., 2015. Fabrication of stable, efficient and recyclable p-CuO/n-ZnO thin film heterojunction for visible light driven photocatalytic degradation of organic dyes. *Materials Letters*, 164, pp. 221-224.

Giannakis, S., Ritmi, S. and Pulgarin, C., 2017. Light-assisted advanced oxidation processes for the elimination of chemical and microbiological pollution of wastewaters in developed and developing countries. *Molecules*, 22, pp. 1070-1091.

HACH, 2021. Oxygen demand, chemical. *USEPA Reactor Digestion Method 8000*. 13th ed.

Hadjltaief, H. B., Zina, M. B., Galvez, M. E. and Costa, P. D., 2016. Photocatalytic

degradation of methyl green dye in aqueous solution over natural clay-supported ZnO-TiO$_2$ catalysts. *Journal of Photochemistry and Photobiology A: Chemistry*, 315, pp. 25-33.

Hagan, E. and Poulin, J., 2021. Statistics of the early synthetic dye industry. *Heritage Science*, 9, pp. 1-14.

Han, C., Yang, M., Weng, B. and Xu, Y., 2014. Improving the photocatalytic activity and anti-photocorrosion of semiconductor ZnO by coupling with versatile carbon. *Physical Chemistry Chemical Physics*, 16, pp. 16891-16903.

Harish, S., Archana, J., Sabarinathan, M., Mavaneethan, M., Nisha, K. D., Ponnusamy, S., Muthamizhchelvan, C., Ikeda, H., Aswal, D. K. and Hayakawa, Y., 2017. Controlled structural and compositional characteristic of visible light active ZnO/CuO photocatalyst for the degradation of organic pollutant. *Applied Surface Science*, 418, pp. 103-112.

Hassaan, M. A. and Nemr, A. E., 2017. Advanced oxidation processes for textile wastewater treatment. *International Journal of Photochemistry and Photobiology*, 2, pp. 85-93.

Hassan, M. M. and Carr, C. M., 2018. A critical review on recent advancements of the removal of reactive dyes from dyehouse effluent by ion-exchange adsorbents. *Chemosphere*, 209, pp. 201-219.

He, X., Chen, M., Chen, R., Zhu, X., Liao, Q., Ye, D., Zhang, B., Zhang, W. and Yu, Y., 2018a. A solar responsive photocatalytic fuel cell with the membrane electrode assembly design for simultaneous wastewater treatment and electricity generation. *Journal of Hazardous Materials*, 358, pp. 346-354.

He, Z. M., Xia, Y. M., Tang, B., Su, J. B. and Jiang, X. F., 2018b. Optimal co-catalytic effect of NiFe$_2$O$_4$/ZnO nanocomposites toward enhanced photodegradation for dye MB. *Zeitschrift für Physikalische Chemie*, 233, pp. 347-359.

Hisatomi, T., Kubota, J. and Domen, K., 2014. Recent advances in semiconductors for photocatalytic and photoelectrochemical water splitting. *Chemical Society Reviews*,

43, pp. 7520-7535.

Holkar, C. R., Jadhav, A. J., Pinjari, D. V., Mahamuni, N. M. and Pandit, A. B., 2016. A critical review on textile wastewater treatment: possible approaches. *Journal of Environmental Management*, 182, pp. 351-366.

Hu, C., Yu, J. C., Hao, Z. and Wong, P. K., 2003. Effects of acidity and inorganic ions on the photocatalytic degradation of different azo dyes. *Applied Catalysis B: Environmental*, 46, pp. 35-47.

Hu, J. L., Tu, J. H., Li, X. Y., Wang, Z. Y., Li, Y., Li, Q. S. and Wang, F. P., 2017. Enhanced UV-visible light photocatalytic activity by constructing appropriate heterostructures between mesosphere TiO$_2$ nanospheres and Sn$_3$O$_4$ nanoparticles. *Nanomaterials*, 7, pp. 1-11.

Hutagalung, S. S., Muchlis, I. and Khotimah, K., 2020. Textile wastewater treatment using advanced oxidation process (AOP). *IOP Conference Series: Materials Science and Engineering*, 722, pp. 1-9.

Hynes, N. R. J., Kumar, J. S., Kamyab, H., Sujana, J. A. J., Al-Khashman, O. A., Kuslu, Y., Ene, A and Kumar, B. S., 2020. Modern enabling techniques and adsorbents based dye removal with sustainability concerns on textile industrial sector – a comprehensive review. *Journal of Cleaner Production*, 272.

Imran, M., Crowley, D. E., Khalid, A., Hussain, S., Mumtaz, M. W. and Arshad, M., 2014. Microbial biotechnology for decolourisation of textile wastewaters. *Reviews in Environmental Science and Biotechnology*, 14, pp. 73-92.

Iraqui, S., Kashyap, S. S. and Rashid, M. H., 2020. NiFe$_2$O$_4$ nanoparticles: an efficient and reusable catalyst for the selective oxidation of benzyl alcohol to benzaldehyde under mild conditions. *Nanoscale Advances*, 2, pp. 5790-5802.

Jaafar, J., Nor, N. A. M., Othman, M. H. D. and Rahman, M. A., 2013. A review study of nanofibers in photocatalytic process for wastewater treatment. *Jurnal Teknologi*, 65, pp. 83-88.

Jamee, R. and Siddique, R., 2019. Biodegradation of synthetic dyes of textile effluent

by microorganisms: an environmentally and economically sustainable approach. *European Journal of Microbiology and Immunology*, 9, pp. 114-118.

Jiang, C., Yang, Q., Wang, D. B., Zhong, Y., Chen, F., Li, X., Zeng, G. M., Li, X. M. and Shang, M. R., 2017. Simultaneous perchlorate and nitrate removal coupled with electricity generation in autotrophic denitrifying biocathode microbial fuel cell. *Chemical Engineering Journal*, 308, pp. 783-790.

Jiang, T. G., Wang, K., Guo, T., Wu, X. Y. and Zhang, G. K., 2020. Fabrication of Z-scheme MoO_3/Bi_2O_4 heterojunction photocatalyst with enhanced photocatalytic performance under visible light irradiation. *Chinese Journal of Catalysis*, 41, pp. 161-169.

Jouanneau, S., Recoules, L., Durand, M. J., Boukabache, A., Picot, V., Primault, Y., Lakel, A., Sengelin, M., Barillon, B. and Thouand, G., 2014. Methods for assessing biochemical oxygen demand (BOD): a review. *Water Research*, 49, pp. 62-82.

Kappadan, S., Thomas, S. and Kalarikkal, N., 2020. $BaTiO_3/ZnO$ heterostructured photocatalyst with improved efficiency in dye degradation. *Materials Chemistry and Physics*, 255.

Katheresan, V., Kansedo, J. and Lau, S. Y., 2018. Efficiency of various recent wastewater dye removal methods: a review. *Journal of Environmental Chemical Engineering*, 6, pp. 4676-4697.

Kaviyarasu, K., Maria Magdalane, C., Jayakumar, D., Samson, Y., Bashir, A. K. H., Maaza, M., Letsholathebe, D., Mahmoud, A. H. and Kennedy, J., 2017. High performance of pyrochlore like $Sm_2Ti_2O_7$ heterojunction photocatalyst for efficient degradation of rhodamine-B dye with waste water under visible light irradiation. *Journal of King Saud University - Science*, 32, pp. 1516-1522.

Kee, M. W., Soo, J. W., Lam, S. M., Sin, J. C. and Mohamed, A. R., 2018. Evaluation of photocatalytic fuel cell (PFC) for electricity production and simultaneous degradation of methyl green in synthetic and real greywater effluents. *Journal of Environmental Management*, 228, pp. 383-392.

Kehinde, F. and Aziz, H. A., 2014. Textile waste water and the advanced oxidative treatment process, an overview. *International Journal of Innovative Research in Science, Engineering and Technology*, 3, pp. 15310-15317.

Kerkez, D., Bečelić-Tomin, M., Milidrag, G. P., Gvoić, V., Mandić, A. K., Maćerak, A. L. and Pilipović, D. T., 2020. Treatment of wastewater containing printing dyes: summary and perspectives. *Conference: 10th International Symposium on Graphic Engineering and Design*, pp. 289-295.

Khalik, W. F., Ho, L. N., Ong, S. A., Voon, C. H., Wong Y. S., Yusuf, S. Y., Yusoff, N. A. and Lee, S. L., 2018. Reactive black 5 as electron donor and/or electron acceptor in dual chamber of solar photocatalytic fuel cell. *Chemosphere*, 202, pp. 467-475.

Khalik, W. F., Ho, L. N., Ong, S. A., Voon, C. H., Wong, Y. S., Yusoff, N. A., Lee, S. L. and Yusuf, S. Y., 2017. Optimization of degradation of Reactive Black 5 (RB5) and electricity generation in solar photocatalytic fuel cell system. *Chemosphere*, 184, pp. 112-119.

Khan, S. and Ali, J., 2018. Chemical analysis of air and water. In: D. P. Häder and G. S. Erzinger, ed. 2018. *Bioassays: Advanced Methods and Applications*. Netherlands: Elsevier. pp. 21-39.

Khatri, J., Nidheesh, P. V., Anantha Singh, T. S. and Suresh Kumar, M., 2018. Advanced oxidation processes based on zero-valent aluminium for treating textile wastewater. *Chemical Engineering Journal*, 348, pp. 67-73.

Kittpanyangam, S. and Eguchi, K., 2019. The development of a fuzzy-based light absorbance measurement device for chemical education. *International Journal of Innovative Computing, Information and Control*, 15, pp. 1-15.

Kokkinos, P., Venieri, D. and Mantzavinos, D., 2021. Advanced oxidation processes for water and wastewater viral disinfection. A systematic review. *Food and Environmental Virology*, pp. 1-20.

Król, A., Pomastowski, P., Rafińska, K., Railean-Plugaru, V. and Buszewski, B., 2017.

Zinc oxide nanoparticles: synthesis, antiseptic activity and toxicity mechanism. *Advances in Colloid and Interface Science*, 16, pp. 37-52.

Kumar, P., Agnihotri, R., Wasewar, K. L., Uslu, H. and Yoo, C., 2012. Status of adsorptive removal of dye from textile industry effluent. *Desalination and Water Treatment*, 50, pp. 226-244.

Kumar, S., Kumar, A., Bahuguna, A., Sharma, V. and Krishnan, V., 2017. Two-dimensional carbon-based nanocomposites for photocatalytic energy generation and environmental remediation applications. *Beilstein Journal of Nanotechnology*, 8, pp. 1571-1600.

Kurt, E., Koseoglu-Imer, D. Y., Dizge, N., Chellam, S. and Koyuncu, I., 2012. Pilot-scale evaluation of nanofiltration and reverse osmosis for process reuse of segregated textile dyewash wastewater. *Desalination*, 302, pp. 24-32.

Lam, S. M., Choong, M. K., Sin, J. C. and Zeng, H. H., 2020a. Synchronous organics removal and copper reduction in semiconductor wastewater with energy recuperation via photocatalytic fuel cell. *E3S Web of Conferences*, 167, pp. 1-4.

Lam, S. M., Jaffari, Z. H., Sin, J. C., Zeng, H. H., Lin, H., Li, H. X. and Mohamed, A. R., 2021. Insight into the influence of noble metal decorated on $BiFeO_3$ for 2,4-dichlorophenol and real herbicide wastewater treatment under visible light. *Colloids and Surfaces A: Physiochemical and Engineering Aspects*, 614, pp. 1-13.

Lam, S. M., Kee, M. W. and Sin, J. C., 2018. Influence of PVP surfactant on the morphology and properties of ZnO micro/nanoflowers for dye mixtures and textile wastewater degradation. *Materials Chemistry and Physics*, 212, pp. 35-43.

Lam, S. M., Quek, J. A. and Sin, J. C., 2018. Mechanistic investigation of visible light responsive Ag/ZnO micro/nanoflowers for enhanced photocatalytic performance and antibacterial activity. *Journal of Photochemistry and Photobiology A: Chemistry*, 353, pp. 171-184.

Lam, S. M., Sin, J. C., Abdullah, A. Z. and Mohamed, A. R., 2012. Degradation of wastewaters containing organic dyes photocatalysed by zinc oxide: a review.

Desalination and Water Treatment, 41, pp. 131-169.

Lam, S. M., Sin, J. C., Abdullah, A. Z. and Mohamed, A. R., 2013. Efficient photodegradation of endocrine-disrupting chemicals with Bi_2O_3-ZnO nanorods under a compact fluorescent lamp. *Water, Air and Soil Pollution*, 224, pp. 1565-1578.

Lam, S. M., Sin, J. C., Lin, H., Li, H. X. and Zeng, H. H., 2020b. Greywater and bacteria removal with synchronized energy production in photocatalytic fuel cell based on anodic TiO_2/ZnO/Zn and cathodic CuO/Cu. *Chemosphere*, 245, pp. 1-10.

Le, A. T., Samsuddin, N. S., Chiam, S. L. and Pung, S. Y., 2021. Synergistic effect of pH solution and photocorrosion of ZnO particles on the photocatalytic degradation of rhodamine B. *Bulletin of Materials Science*, 44, pp. 1-10.

Lee, S. L., Ho, L. N., Ong, S. A., Lee, G. M., Wong, Y. S., Voon, C. H., Khalik, W. F., Yusoff, N. A. and Nordin, N., 2016a. Comparative study of photocatalytic fuel cell for degradation of methylene blue under sunlight and ultra-violet light irradiation. *Water, Air and Soil Pollution*, 227, pp. 445-452.

Lee, S. L., Ho, L. N., Ong, S. A., Wong, Y. S., Voon, C. H., Khalik, W. F., Yusoff, N. A. and Nordin, N., 2018. Exploring the relationship between molecular structure of dyes and light sources for photodegradation and electricity generation in photocatalytic fuel cell. *Chemosphere*, 209, pp. 935-943.

Lee, S. L., Ho, L. N., Ong, S. A., Wong, Y. S., Voon, C. H., Khalik, W. F. and Nordin, N., 2016b. A highly efficient immobilised ZnO/Zn photoanode for degradation of azo dye Reactive Green 19 in a photocatalytic fuel cell. *Chemosphere*, 166, pp. 118-125.

Lee, S. L., Ho, L. N., Ong, S. A., Wong, Y. S., Voon, C. H., Khalik, W. F., Yusoff, N. A. and Nordin, N., 2016c. Enhanced electricity generation and degradation of the azo dye Reactive Green 19 in a photocatalytic fuel cell using ZnO/Zn as the photoanode. *Journal of Cleaner Production*, 127, pp. 579-584.

Lee, S. L., Ho, L. N., Ong, S. A., Wong, Y. S., Voon, C. H., Khalik, W. F., Yusoff, N.

A. and Nordin, N., 2017. A highly efficient immobilized ZnO/Zn photoanode for degradation of azo dye reactive green 19 in a photocatalytic fuel cell. *Chemosphere*, 166, pp. 118-125.

Lellis, B., Fávaro-Polonio, C. Z., Pamphile, J. A., and Polonio, J. C., 2019. Effects of textile dyes on health and the environment and bioremediation potential of living organisms. *Biotechnology Research and Innovation*, 3, pp. 275-290.

Li, D. and Liu, S., 2019. Water quality monitoring in aquaculture. *Water quality monitoring and management: basic, technology and case studies*. Cambridge: Academic Press. pp. 21-39.

Li, D., Song, H., Meng, X., Shen, T., Sun, J., Han, W. and Wang, X., 2020. Effects of particle size on the structure and photocatalytic performance by alkali-treated TiO_2. *Nanomaterials*, 10, pp. 546-559.

Li, X. Y., Li, W. J., Gu, S. N., Liu, X. T., Li, H. D., Ren, C. J., Ma, X. H. and Zhou, H. L., 2021a. Efficient ytterbium-doped Bi_2WO_6 photocatalysts: synthesis, the formation of oxygen vacancies and boosted superoxide yield for enhanced visible-light photocatalytic activity. *Journal of Alloys and Compounds*, 851, pp. 1-9.

Li, X., Garlisi, C., Guan, Q. S., Anwer, S., Ali-Ali, K., Palmisano, G. and Zheng, L. X., 2021b. A review of material aspects in developing direct Z-scheme photocatalysts. *Materials Today*, 47, pp. 75-107.

Li, Y. F., Zhang, W. P., Li, X. R. and Yu, Y., 2014. TiO_2 nanoparticles with high ability for selective adsorption and photodegradation of textile dyes under visible light by feasible preparation. *Journal of Physics and Chemistry of Solids*, 75, pp. 86-93.

Li, Y. M., Wang, K., Wu, J., Gu, L., Lu, Z. F., Wang, X. J. and Cao, X. B., 2015. Synthesis of highly permeable Fe_2O_3/ZnO hollow spheres for printable photocatalysis. *RSC Advances*, 5, pp. 88277-88286.

Liao, Q., Li, L., Chen, R., Zhu, X., Wang, H., Ye, D., Cheng, X., Zhang, M. and Zhou, Y., 2015. Respective electrode potential characteristics of photocatalytic fuel cell

with visible-light responsive photoanode and air-breathing cathode. *International Journal of Hydrogen Energy*, 40, pp. 16547-16555.

Lin, K., Zhu, Y., Zhang, Y. and Lin, H., 2019. Determination of ammonia nitrogen in natural waters: recent advances and applications. *Trends in Environmental Analytical Chemistry*, 24.

Liu, M., Lü, Z., Chen, Z., Yu, S. and Gao, C., 2019. Comparison of reverse osmosis and nanofiltration membranes in the treatment of biologically treated textile effluent for water reuse. *Desalination*, 281, pp. 372-378.

Liu, Q., 2020. Pollution and treatment of dye waste-water. *IOP Conference Series: Earth and Environmental Science*, 514, pp. 1-7.

Liu, X., Jin, A. L., Jia, Y. S., Xia, T. L., Deng, C. X., Zhu, M. H., Chen, C. F. and Chen, X. S., 2017. Synergy of adsorption and visible-light photocatalytic degradation of methylene blue by a bifunctional Z-scheme heterojunction of WO$_3$/g-C$_3$N$_4$. *Applied Surface Science*, 405, pp. 359-371.

Liu, Y. B., Li, J. H., Zhou, B. X., Lv, S. B., Li, X. J., Chen, H. C., Chen, Q. P. and Cai, W. M., 2012. Photoelectrocatalytic degradation of refractory organic compounds enhanced by a photocatalytic fuel cell. *Applied Catalysis B: Environmental*, 111-112, pp. 485-491.

Lu, Q., Yu, Y., Ma, Q., Chen, B. and Zhang, H., 2016. 2D transition-metal-dichalcogenide-nanosheet-based composites for photocatalytic and electrocatalytic hydrogen evolution reactions. *Advanced Materials*, 28, pp. 1917-1933.

Lu, X. X., Li, Q., Wang, L. J., Jiang, W., Luo, R., Zhang, M., Cui, C. P., Tian, Z. F. and Zhu, G. P., 2021. Fabrication of one dimensional hierarchical WO$_3$/BiOI heterojunctions with enhanced visible light activity for degradation of pollutants. *RSC Advances*, 11, pp. 16608-16618.

Ma, X. and Xia, H., 2009. Treatment of water-based printing ink wastewater by Fenton process combined with coagulation. *Journal of Hazardous Materials*, 162, pp. 386-390.

Ma, X. and Xia, H., 2010. Optimization of coagulation process for treatment of water-based printing ink wastewater. *4th International Conference on Bioinformatics and Biomedical Engineering*, pp. 1-4.

Mai, F. D., Chen, C. C., Chen, J. L. and Liu, S. C., 2008. Photodegradation of methyl green using visible irradiation in ZnO suspensions: determination of the reaction pathways and identification of intermediates by a high-performance liquid chromatography-photodiode array-electrospray ionization-mass spectrometry method. *Journal of Chromatography A*, 1189, pp. 335-365.

Marcello, B. A., Correa, O. V., Bento, R. T. and Pillis, M. F., 2020. Effect of growth paramters on the photocatalytic performance of TiO_2films prepared by MOCVD. *Journal of Brazilian Chemical Society*, 31, pp. 1-14.

Martínez, D. M., Ebenhack, B. W. and Wagner, T. P., 2019. Chapter 5 – electric power sector energy efficiency. *Energy Efficiency: Concepts and Calculations*. Amsterdam: Elsevier. pp. 129-160.

Mitrović, J., Radović, M. D., Bojić, D., Andjelković, T., Purenovic, M. and Bojić, A., 2012. Decolourisation of textile azo dye reactive orange 16 with UV/H_2O_2 process. *Journal of the Serbian Chemical Society*, 77, pp. 465-481.

Mohammadzadeh, S., Olya, M., Arabi, A., Shariati, A., and Nikou, M. K., 2015. Synthesis, characterization and application of ZnO-Ag as a nanophotocatalyst for organic compounds degradation, mechanism and economic study. *Journal of Environmental Science*, 35, pp. 194-207.

Moradi, S., Fardood, S. T. and Ramazani, A., 2018. Green synthesis and characterization of magnetic $NiFe_2O_4$@ZnO nanocomposite and its application for photocatalytic degradation of organic dyes. *Journal of Materials Science: Materials in Electronics*, 29, pp. 14151-14160.

Mostafa, A. A. F., Elshikh, M. S., Al-Askar, A. A., Hadibarata, T., Yuniarto, A. and Syafiuddin, A., 2019. Decolourisation and biotransformation pathway of textile dye by *Cylindrocephalum aurelium*. *Bioprocess and Biosystems Engineering*, 42, pp. 1483-1494.

Moussa, D. T., El-Naas, M. H., Nasser, M. and Al-Marri, M. J., 2017. A comprehensive review of electrocoagulation for water treatment: potentials and challenges. *Journal of Environmental Management*, 186, pp. 24-41.

Omotosho, O. O. and Ameuru, U. S., 2019. Synthesis and dyeing properties of acid dyes derived from 1-amino-2-naphthol-4-sulphonic acid. *World Journal of Applied Chemistry*, 4, pp. 63-68.

Ong, Y. P., Ho, L. N., Ong S. A., Banjuraizah, J., Ibrahim, A. H., Lee, S. L. and Nordin, N., 2020. Comparative study of different polyatomic ions of electrolytes on electricity generation and dye decolourisation in photocatalytic fuel cell. *Journal of Water Process Engineering*, 37.

Ong, Y. P., Ho, L. N., Ong, S. A., Banjuraizah, J., Ibrahim, A. H., Thor, S. H. and Teoh, T. P., 2021. Dye decolourisation and energy recovery of photocatalytic fuel cell subjected to optimization of supporting electrolyte concentration and external resistance. *Journal of Environmental Chemical Engineering*, pp. 1-9.

Orozco-Messana, J. and Camaratta, R., 2022. ZnO electrodeposition model for morphology control. *Nanomaterials*, 12, pp. 1-12.

Pal, P., 2017. Industry-specific water treatment: case studies. *Industrial Water Treatment Process Technology*. United Kingdom: Butterworth-Heinemann. pp. 243-511.

Papadopoulos, K. P., Argyriou, R., Economou, C. N., Charalampous, N., Dailianis, S., Tatoulis, T. I., Tekerlekopoulou, A. G. and Vayenas, D. V., 2019. Treatment of printing ink wastewater using electrocoagulation. *Journal of Environmental Management*, 237, pp. 442-448.

Patel, H. and Vashi, R. T., 2015. Characterization of textile wastewater. *Characterization and treatment of textile wastewater*. Netherlands: Elsevier. pp. 21-71.

Pei, G. and Yu, F., 2016. Review article review on ink wastewater treatment technology. *Journal of Scientific and Engineering Research*, 3, pp. 67-70.

Pelaez, M., Falaras, P., Likodimos, V., O'Shea, K., de la Cruz, A. A., Dunlop, P. S. M., Bryne. J. A. and Dionysiou, D. D., 2016. Use of selected scavengers for the determination of NF-TiO$_2$ reactive oxygen species during the degradation of Microcystin-LR under visible light irradiation. *Journal of Molecular Catalysis A: Chemical*, 425, pp. 183-189.

Phonsy, P. D., Anju, S. G., Jyothi, K. P., Yesodharan, S., Yesodharan, E. P., 2015. Semiconductor mediated photocatalytic degradation of plastics and recalcitrant organic pollutants in water: effect of additives and fate of in situ formed H$_2$O$_2$. *Journal of Advanced Oxidation Technologies*, 18, pp. 85-97.

Piaskowski, K., Świderska-Dąbrowska, R. and Zarzycki, P., 2018. Dye removal from water and wastewater using various physical, chemical and biological processes. *Journal of AOAC International*, 101, pp. 1371-1384.

Pica, M., Calzuola, S., Donnadio, A., Gentili, P. L., Nocchetti, M. and Casciola, M., 2018. De-ethylation and cleavage of rhodamine B by a zirconium phosphate/silver bromide composite photocatalyst. *Catalysts*, 9, pp. 1-15.

Rahmayeni, Zulhadjri, Jamarun, N., Emriandi and Arieff, S., 2016. Synthesis of ZnO-NiFe$_2$O$_4$ magnetic nanocomposites by simple solvothermal for photocatalytic dye degradation under solar light. *Oriental Journal of Chemistry*, 32, pp. 1411-1419.

Ramirez, J. C. C. and Tulmova, T. P., 2018. Analysis and optimization of printing ink formulations for polyethylene films. *Applied Adhesion Science*, 6, pp. 1-21.

Rane, A. V., Kanny, K., Abitha, V. K. and Thomas, S., 2018. Methods for synthesis of nanoparticles and fabrication of nanocomposites. *Synthesis of Inorganic Nanomaterials*, pp. 121-139.

Rao, M. P., Wu, J. J., Asiri, A. M., Anandan, S. and Ashokkumar, M., 2018. Photocatalytic properties of hierarchical CuO nanosheets synthesized by a solution phase method. *Journal of Environmental Sciences*, 69, pp. 115-124.

Rao, V. J., Matthiesen, M., Goetz, K. P., Huck, C., Yim, C., Siris, R., Han, J., Bunz, U. H. F., Dreuw, A., Duesberg, G. S., Pucci, A. and Zaumseil, J., 2020. AFM-IR

and IR-SNOM for the characterization of small molecule organic semiconductors. *Journal of Physical Chemistry C*, 124, pp. 5331-5344.

Ravichandran, K., Mohan, R., Sakthivel, B., Varadharajaperumal, S., Devemdran, P., Alagesan, T. and Pandian, K., 2014. Enhancing the photocatalytic efficiency of sprayed ZnO thin films through double doping (Sn + F) and annealing under different ambiences. *Applied Surface Science*, 321, pp. 310-317.

Ren, K. and Gan, Y. X., 2012. Advances in photoelectrochemical fuel cell research. *Small-Scale Energy Harvesting*, pp. 3-26.

Reshchikov, M. A., 2021. Measurement and analysis of photoluminescence in GaN. *Journal of Applied Physics*, 129.

Safwat, S. M., 2018. Performance of moving bed biofilm reactor using effective microorganisms. *Journal of Cleaner Production*, 185, pp. 723-731.

Sahayarayan, J. J., Ramasamy, V. and Kandasamy, K., 2019. Treatment of textile wastewater using vertical flow constructed wetland with planted *Alternanthera sessilis* and *Zea mays*. *International Journal of Advanced Research*, 7, pp. 731-741.

Saimy, I. S. and Raji, F., 2015. Applications and sustainability in groundwater extraction in Malaysia. *Jurnal Teknologi (Science and Engineering)*, 73, pp. 39-45.

Saimy, I. S. and Yusuf, N. A. M., 2013. The need for better water policy and governance in Malaysia. *Procedia – Social and Behavioural Sciences*, 81, pp. 371-375.

Sall, M. L., Diaw, A. K. D., Gningue-Sall, D., Efremova Aaron, S. and Aaron, J. J., 2020. Toxic heavy metals: impact on the environment and human health, and treatment with conducting organic polymers, a review. *Environmental Science and Pollution Research*, 27, pp. 1-16.

Samsani, S., Mohamadi, M., Sarrafzadeha, M. H., Hadibarata, T., Rene, E. R. and Firoozbahr, M., 2020. Recent advances in the treatment of dye-containing wastewater from textile industries: overview and perspectives. *Process Safety and Environmental Protection*, 143, pp. 138-163.

Samsudin, E. M., Goh, S. N., Wu, T. Y., Tan, T. L., Abd Hamid, S. B. and Juan, J. C., 2015. Evaluation on the photocatalytic degradation activity of Reactive Blue 4 using pure anatase nano-TiO$_2$. *Sains Malaysiana*, 44, pp. 1011-1019.

Sangpour, P., Hashemi, F. and Moshfegh, A. Z., 2010. Photoenhanced degradation of methylene blue on cosputtered M:TiO$_2$ (M = Au, Ag, Cu) nanocomposite systems: a comprehensive study. *Journal of Physical Chemistry C*, 114, pp. 13955-13961.

Seger, B. and Kamat, P.V., 2009. Fuel cell geared in reverse: photocatalytic hydrogen production using a TiO$_2$/Nafion/Pt membrane assembly with no applied bias. *Journal of Physical Chemistry C*, 113, pp. 18946-18952.

Sfaelou, S. and Lianos, P., 2016. Photoactivated fuel cells (PhotoFuelCells). An alternative source of renewable energy with environmental benefits. *AIMS Materials Science*, 3, pp. 270-288.

Shabat-Hadas, E., Mamane, H. and Gitis, V., 2017. Rhodamine B in dissolved and nano-bound forma: indicators for light-based advanced oxidation processes. *Chemosphere*, 184, pp. 1020-1027.

Shamey, R. and Zhao, X., 2014. *Modelling, simulation and control of the dyeing process*. 1st ed. Cambridge: Woodhead Publishing.

Shen, K. and Gondal, M. A., 2017. Removal of hazardous Rhodamine dye from water by adsorption onto exhausted coffee ground. *Journal of Saudi Chemical Society*, 21, pp. 120-127.

Shen, S., Chen, J., Wang, M., Sheng, X., Chen, X., Feng, X., and Mao, S. S., 2018. Titanium dioxide nanostructures for photoelectrochemical applications. *Progress in Materials Science*, 98, pp. 299-385.

Shen, Z. M., Wu, D., Yang, J., Yuan, T., Wang, W. H. and Jia, J. P., 2006. Methods to improve electrochemical treatment effect of dye wastewater. *Journal of Hazardous Materials*, 131, pp. 90-97.

Shi, W. L., Guo, F. and Yuan, S. L., 2017. In situ synthesis of Z-scheme Ag$_3$PO$_4$/CuBi$_2$O$_4$ photocatalysts and enhanced photocatalytic performance for the

degradation of tetracycline under visible light irradiation. *Applied Catalysis B: Environmental*, 209, pp. 720-728.

Shindhal, T., Rakholiya, P., Varjani, S., Pandey, A., Ngo, H. H., Guo, W. S., Ng, H. Y. and Taherzadeh, M. J., 2020. A critical review on advances in the practices and perspectives for the treatment of dye industry wastewater. *Bioengineered*, 12, pp. 70-87.

Sim, L. C., Wong, J. L., Hak, C. H., Tai, J. Y., Leong, K. H. and Saravanan, P., 2018. Sugarcane juice derived carbon dot-graphitic carbon nitride composites for bisphenol A degradation under sunlight irradiation. *Beilstein Journal of Nanotechnology*, 9, pp. 353-363.

Sin, J. C., Lam, S. M., Zeng, H. H., Lin, H., Li, H. X., Kumaresan, A. K., Mohamed, A. R. and Lim, J. W., 2020. Z-scheme heterojunction nanocomposite fabricated by decorating magnetic $MnFe_2O_4$ nanoparticles on BiOBr nanosheets for enhanced visible light photocatalytic degradation of 2,4-dichlorophenoxyacetic acid and Rhodamine B. *Separation and Purification Technology*, 250.

Sivarajasekar, N. and Baskar, R., 2014. Adsorption of basic red 9 on activated waste *Gossypium hirsutum* seeds: process modelling, analysis and optimization using statistical design. *Journal of Industrial and Engineering Chemistry*, 20, pp. 2699-2709.

Solís, M., Solís, A., Pérez, H. I., Manjarrez, N. and Flores, M., 2012. Microbial decolouration of azo dyes: a review. *Process Biochemistry*, 47, pp. 1723-1748.

Solomon, G., Kohan, M. G., Landström, A., Vomiero, A. and Concina, I., *2020.* Semiconducting metal oxides empowered by graphene and its derivatives: progresses and critical perspective on selected functional applications. *Journal of Applied Physics*, 128, pp. 1-44.

Somoghi, R., Purcar, V., Alexandrescu, E., Gilfu, I. C., Ninciuleanu, C. M., Cotrut, C. M., Oancea, F. and Stroescu, H., 2021. Synthesis of zinc oxide nanomaterials via sol-gel process with anti-corrosive effect for Cu, Al and Zn metallic substrates. *Coatings*, 11, pp. 1-15.

Stumpp, M., Damtew, D., Stock, D., Hess, K., Schröder, D. and Schlettwein, D., 2018. Controlled electrodeposition of zinc oxide on conductive meshes and foams enabling its use as secondary anode. *Journal of the Electrochemical Society*, 165, pp. 461-466.

Sudha, M., Renu, G. and Sangeeta, G., 2021. Mineralization and degradation of 4-nitrophenol using homogenous Fenton oxidation process. *Environmental Engineering Research*, 26, pp. 1-10.

Sun, K., Yuan, D., Liu, Y., Song, Y., Sun, Z., and Liu, R., 2019a. Study on the efficiency and mechanism of Direct Red 80 dye by conventional ozonation and peroxone (O_3/H_2O_2) treatment. *Separation Science and Technology*, pp. 1-9.

Sun, Q., Wu, S., You, D., Zang, T. and Dong, L., 2019b. Novel composite functional photocatalytic fuel cell assisted by Fenton-like reactions. *Applied Surface Science*, 467-468, pp. 825-835.

Sun, Y. and Yang, K., 2020. Discussion on printing and dyeing wastewater treatment methods. *IOP Conference Series: Earth and Environmental Science*, 514, pp. 1-4.

Tan, X. H., Bai, J., Zheng, J. Y., Li, J. H., Zhou, T. S., Xia, L. G., Xu, Q. J. and Zhou, B. X., 2019. Photocatalytic fuel cell based on sulfate radicals converted from sulfates in situ for wastewater treatment and chemical energy utilization. *Catalysis Today*, 335, pp. 485-491.

Tiwari, R., Manojit, D., Tewari, H.S. and Ghoshal, S. K., 2020. Structural and magnetic properties of tailored $NiFe_2O_4$ nanostructures synthesized using auto-combustion method. *Results in Physics*, 16, pp. 1-8.

Tortajada, C., 2020. Contributions of recycled wastewater to clean water and sanitation sustainable development goals. *NPJ Clean Water*, 3, pp. 1-6.

Ullah, H., Viglašová, E. and Galamboš, M., 2021. Visible light-driven photocatalytic Rhodamine B degradation using CdS nanorods. *Processes*, 9, pp. 1-11.

Ungan, H. and Tekin, T., 2019. Effect of the sonication and coating time on the photcatalytic degradation of TiO_2, TiO_2-Ag and TiO_2-ZnO thin film photocatalysts.

Chemical Engineering Communications, 207, pp. 869-903.

United Nations World Water Assessment Programme, 2018. *The United Nations world water development report 2018: nature-based solutions for water*. [e-book] Paris: UNESCO.

Vasiljevic, Z. Z., Dojcinovic, M. P., Vujancevic, J. D., Jankovic-Castvan, I., Ognjanovic, M., Tadic, N. B., Stojadinovic, S., Brankovic, G. O. and Nikolic, M. V., 2020. Photocatalytic degradation of methylene blue under natural sunlight using iron titanate nanoparticles prepared by a modified sol-gel method. *Royal Society Open Science*, 7, pp. 1-14.

Vasseghian, Y., Khataee, A., Dragoi, E.-N., Moradi, M., Nabavifard, S., Conto, G. O. and Khaneghah, 2020. Pollutants degradation and power generation by photocatalytic fuel cells: a comprehensive review. *Arabian Journal of Chemistry*, 13, pp. 8458-8480.

Verma, R., Kundu, L. M. and Pandey, L. M., 2021. Decontamination of distillery spent wash through advanced oxidation methods. In: M. P. Shah, ed. 2020. *Advanced oxidation processes for effluent treatment plants*. Netherlands: Elsevier. pp. 103-117.

Vymazal, J., 2011. Constructed wetlands for wastewater treatment: five decades of experience. *Environmental Science and Technology*, 45, pp. 61-69.

Wang, B., Zhang, H., Lu, X. Y., Xuan, J. and Leung, M. K. H., 2014. Solar photocatalytic fuel cell using CdS-TiO$_2$ photoanode and air-breathing cathode for wastewater treatment and simultaneous electricity production. *Chemical Engineering Journal*, 253, pp. 174-182.

Wang, K., Li, J. and Zhang, G. K., 2019. Ag-bridged Z-scheme 2D/2D Bi$_5$FeTi$_3$O$_{15}$/g-C$_3$N$_4$ heterojunction for enhanced photocatalysis: mediator-induced interfacial charge transfer and mechanism insights. *ACS Applied Materials and Interfaces*, 11, pp. 27686-27696.

Wang, M., Fei, G. T. and Zhang, L. D., 2010. Porous ZnO-nanobelt film as recyclable

photocatalysts with enhanced photocatalytic activity. *Nanoscale Research Letters*, 5, pp. 1800-1803.

Wang, W., Zhou, Q., Fei, X., He, Y., Zhang, P., Zhang, G., Peng, L. and Xie, W., 2010. Synthesis of CuO nano- and micro-structures and their Raman spectroscopic studies. *CrystEngComm*, 12, pp. 2232-2237.

Wang, X. B., Liu, J., Leong, S. W., Lin, X. C., Wei, J., Kong, B., Xu, Y. F., Low, Z. X., Yao, J. F. and Wang H. T., 2016. Rapid construction of ZnO@ZIF-8 heterostructures with size-selective photocatalysis properties. *ACS Applied Materials and Interfaces*, 8, pp. 9080-9087.

Wang, X. J., Wu, Z., Wang, Y., Wang, W., Wang, X., Bu, Y. J. and Zhao, J. F., 2013. Adsorption-photodegradation of humic acid in water by using ZnO coupled TiO_2/bamboo charcoal under visible light irradiation. *Journal of Hazardous Materials*, 262, pp. 16-24.

Wang, X. N., Jia, J. P. and Wang, Y. L., 2011. Degradation of C.I. reactive red 2 through photocatalysis coupled with water jet cavitation. *Journal of Hazardous Materials*, 185, pp. 315-321.

Wu, X., Wen, L., Lv, K., Deng, K., Tang, D., Ye, H., Du, D., Liu, S. and Li, M., 2014. Fabrication of ZnO/graphene flake-like photocatalyst with enhanced photoreactivity. *Applied Surface Science*, 358, pp. 130-136.

Wu, Z., Zhao, G., Zhang, Y., Liu, J. and Shi, H., 2015. A solar-driven photocatalytic fuel cell with dual photoelectrode for simultaneous wastewater treatment and hydrogen production. *Journal of Materials Chemistry A*, 3, pp. 3416-3424.

Xia, Y. M., He, Z. M., Su, J. B., Liu, Y., Tang, B. and Li, X. P., 2018. Fabrication of novel n-$SrTiO_3$/p-BiOI heterojunction for degradation of crystal violet under simulated solar light irradiation. *Nano*, 13, pp. 1-12.

Xie, S. and Ouyang, K., 2017. Degradation of refractory organic compounds by photocatalytic fuel cell with solar responsive WO_3/FTO photoanode and air-breathing cathode. *Journal of Colloid and Interface Science*, 500, pp. 220-227.

Xu, P., Xu, H. and Zheng, D., 2019. Simultaneous electricity generation and wastewater treatment in a photocatalytic fuel cell integrating electro-Fenton process. *Journal of Power Sources*, 421, pp. 156-161.

Xu, Q. L., Zhang, L. Y., Yu, J. G., Wageh, S., Al-Ghamdi, A. A. and Jaroniec, M., 2018. Direct Z-scheme photocatalysts: principles, synthesis and applications. *Materials Today*, 21, pp. 1042-1063.

Xu, Z., Liang, J. and Zhou, L., 2013. Template-free hydrothermal synthesis of β-FeOOH nanorods and their catalytic activity in the degradation of methyl orange by a photo-fenton-like process. *Open Journal of Inorganic Non-metallic Materials*, 3, pp. 58-65.

Yang, X. L., Qian, F. F., Zou, G. J., Li, M. L., Lu, J. R., Li, Y. M. and Bao, M. T., 2016. Facile fabrication of acidified $g-C_3N_4/g-C_3N_4$ hybrids with enhanced photocatalysis performance under visible light irradiation. *Applied Catalysis B: Environmental*, 193, pp. 22-35.

Yang, X., López-Grimau, V., Vilaseca, M., and Crespi, M., 2020. Treatment of textile wastewater by CAS, MBR and MBBR: a comparative study from technical, economic and environmental perspectives. *Water*, 12, pp. 1-17.

Yaseen, D. A. and Scholz, M., 2016. Shallow pond systems planted with *Lemma minor* treating azo dyes. *Ecological Engineering*, 94, pp. 295-305.

Yaseen, D. A. and Scholz, M., 2018. Textile dye wastewater characteristics and constituents of synthetic effluents: a critical review. *International Journal of Environmental Science and Technology*, 16, pp. 1193-1226.

Yin, H., Qiu, P., Qian, Y., Kong, Z., Zheng, X., Tang, Z. and Guo, H., 2019. Textile wastewater treatment for water reuse: a case study. *Processes*, 7, pp. 1-21.

Ying, D. W., Cao, R. Q., Li, C. J., Tang, T. T., Li, K., Wang, H. W., Wang, Y. L. and Jia, J. P., 2016. Study of the photocurrent in a photocatalytic fuel cell for wastewater treatment and the effects of TiO_2 surface morphology to the apportionment of the photocurrent. *Electrochimica Acta*, 192, pp. 319-327.

Yong, Z. J., Lam, S. M., Sin, J. C. and Mohamed, A. R., 2021. Feasibility study of municipal wastewater removal synchronized with electricity generation via solar-driven photocatalytic fuel cell with Bi_2WO_6/ZnO nanorods array photoanode. *IOP Conference Series: Earth and Environmental Science*, 945, pp. 1-7.

Yu, K., Yang, S. G., He, H., Sun, C., Gu, C. G. and Ju, Y. M., 2009. Visible light-driven photocatalytic degradation of rhodamine B over $NaBiO_3$: pathways and mechanism. *The Journal of Physical Chemistry A*, 113, pp. 10024-10032.

Zhang, J. and Zhang, T., 2013. Preparation and characterisation of highly efficient and stable visible-light-responsive photocatalyst $AgBr$/Ag_3PO_4. *Journal of Nanomaterials*, pp. 1-11.

Zhang, Q., Chen, J. X., Xie, Y. Y., Wang, M. Z. and Ge, X. W., 2016. Inductive effect of poly (vinyl pyrrolidone) on morphology and photocatalytic performance of Bi_2WO_6. *Applied Surface Science*, 368, pp. 332-340.

Zhang, Y. Xie, M. Y., Adamaki, V., Khanbareh, H. and Bowen, C. R., 2017. Control of electro-chemical processes using energy harvesting materials and devices. *Chemical Society Reviews*, 46, pp. 1-30.

Zhang, Y., Ju, P., Hao, L., Zhai, X. F., Jiang, F. H. and Sun, C. J., 2021. Novel Z-scheme MoS_2/Bi_2WO_6 heterojunction with highly enhanced photocatalytic activity under visible light irradiation. *Journal of Alloys and Compounds*, 854, pp. 1-14.

Zhao, K., Bai, J., Zeng, Q., Zhang, Y., Li, J., Li, L., Xia, L. and Zhou, B., 2017. Efficient wastewater treatment and simultaneously electricity production using a photocatalytic fuel cell based on the radical chain reactions initiated by dual photoelectrodes. *Journal of Hazardous Materials*, 337, pp. 47-54.

Zhao, Y. Q., Li, Y. C., Yang, Z and Fang, Y. J., 2011. A novel monitoring system for COD using optical ultraviolet absorption method. *Procedia Environmental Sciences*, 10, pp. 2348-2353.

Zhu, H. Y., Jiang, R., Fu, Y. Q., Li, R. R., Yao, J. and Jiang, S. T., 2016. Novel multifunctional $NiFe_2O_4$/ZnO for dye removal by adsorption, photocatalysis and

magnetic separation. *Applied Surface Science*, 369, pp. 1-10.

Zhu, H., Jiang, R., Xiao, L., Chang, Y., Guan, Y., Li, X and Zeng, G., 2009. Photocatalytic decolourisation and degradation of Congo Red on innovative crosslinked chitosan/nano-CdS composite catalyst under visible light irradiation. *Journal of Hazardous Materials*, 169, pp. 933-940.

APPENDICES

$$y = 0.1469x + 0.045$$
$$R^2 = 0.996$$
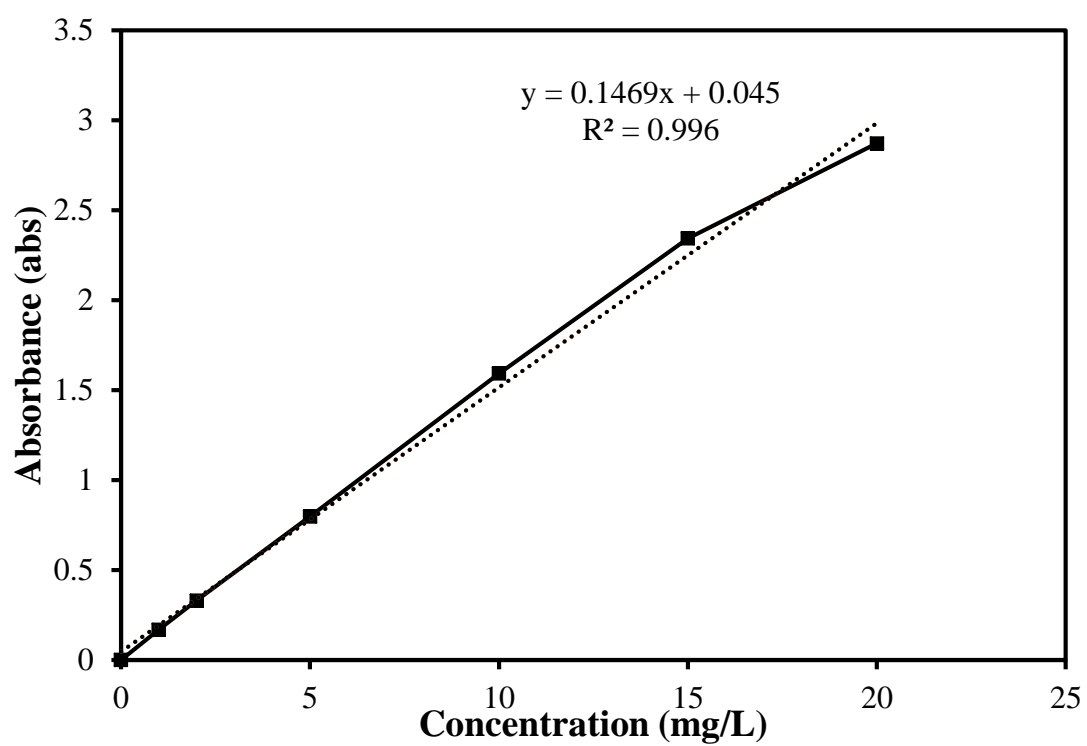
Appendix A1: RhB Dye Calibration Curve.

AWARD

2nd Place in Green Technology Category, awarded by 8th International Biotechnology Competition and Exhibition 2022 (IBCEx22) organized by Universiti Teknologi Malaysia (UTM), Johor via Cisco Webex online platform on 15 – 16th April 2022.

Title of Project: Photocatalytic Fuel Cell for Remediation of Environmental Pollutants and Sustainable Power Production.

Contributors: ChM. Ts. Dr. Lam Sze Mun, ChM. Ts. Dr. Sin Jin Chung, Warren Tong Meng Wei, Joyee Yap Chun Ting.